UNIVERSIDADE ESTADUAL DE MARINGÁ
PÓS-GRADUAÇÃO EM FÍSICA

DESLOCAMENTO TERMOELÁSTICO E EFEITOS DE BORDA DETECTADOS POR ESPELHO FOTOTÉRMICO E INTERFEROMETRIA

Gabriel Antonio Flizikowski Siqueira

Orientador: **Prof. Dr. Nelson Guilherme Castelli Astrath**

Co-orientador: **Prof. Dr. Luis Carlos Malacarne**

Co-orientador: **Prof. Dr. Tomaž Požar**

Maringá, 2023

STATE UNIVERISTY OF MARINGÁ
PHYSICS GRADUATE PROGRAM

THERMOELASTIC DISPLACEMENT AND EDGE EFFECTS DETECTED BY PHOTOTHERMAL MIRROR AND INTERFEROMETRY

Gabriel Antonio Flizikowski Siqueira

Supervisor: **Prof. Dr. Nelson Guilherme Castelli Astrath**

Co-supervisor: **Prof. Dr. Luis Carlos Malacarne**

Co-supervisor: **Prof. Dr. Tomaž Požar**

Maringá, 2023

UNIVERSIDADE ESTADUAL DE MARINGÁ
PÓS-GRADUAÇÃO EM FÍSICA

DESLOCAMENTO TERMOELÁSTICO E EFEITOS DE BORDA DETECTADOS POR ESPELHO FOTOTÉRMICO E INTERFEROMETRIA

Gabriel Antonio Flizikowski Siqueira

Tese apresentada ao Departamento de Física da Universidade Estadual de Maringá para a obtenção do título de Doutor em Física.

Banca Examinadora:

Prof. Dr. Nelson Guilherme Castelli Astrath	UEM (Orientador)
Profa. Dra. Andressa Novatski	UEPG
Prof. Dr. Leandro Herculano da Silva	UTFPR
Prof. Dr. Robson Ferrari Muniz	UEM
Prof. Dr. Vitor Santaella Zanuto	UEM
Prof. Dr. Antonio Medina Neto	UEM (Suplente)
Prof. Dr. Tomaž Požar	University of Ljubljana (Suplente)

Maringá, 2023

STATE UNIVERSITY OF MARINGÁ
PHYSICS GRADUATE PROGRAM

THERMOELASTIC DISPLACEMENT AND EDGE EFFECTS DETECTED BY PHOTOTHERMAL MIRROR AND INTERFEROMETRY

Gabriel Antonio Flizikowski Siqueira

A dissertation submitted to the Physics Department of the State University of Maringá to obtain the Doctoral Degree in Physics.

Supervisory Commitee:

Prof. Dr. Nelson Guilherme Castelli Astrath	UEM (Supervisor)
Prof. Dr. Andressa Novatski	UEPG
Prof. Dr. Leandro Herculano da Silva	UTFPR
Prof. Dr. Robson Ferrari Muniz	UEM
Prof. Dr. Vitor Santaella Zanuto	UEM
Prof. Dr. Antonio Medina Neto	UEM (Substitute)
Prof. Dr. Tomaž Požar	University of Ljubljana (Substitute)

Maringá, 2023

Dados Internacionais de Catalogação-na-Publicação (CIP)
(Biblioteca Central - UEM, Maringá - PR, Brasil)

Siqueira, Gabriel Antonio Flizikowski

S618d Deslocamento termoelástico e efeitos de borda detectados por espelho fototérmico e interferometria / Gabriel Antonio Flizikowski Siqueira. -- Maringá, PR, 2023.
119 f.: il. color., figs., tabs.

Orientador: Prof. Dr. Nelson Guilherme Castelli Astrath.
Coorientador: Prof. Dr. Luis Carlos Malacarne.
Tese (Doutorado) - Universidade Estadual de Maringá, Centro de Ciências Exatas, Departamento de Física, Programa de Pós-Graduação em Física, 2023.

1. Fenômenos fototérmicos - Física. 2. Espelho Térmico. 3. Interferometria. 4. Efeitos de Borda. 5. Deslocamento Termoelástico. I. Astrath, Nelson Guilherme Castelli, orient. II. Malacarne, Luis Carlos, coorient. III. Universidade Estadual de Maringá. Centro de Ciências Exatas. Departamento de Física. Programa de Pós-Graduação em Física. IV. Título.

CDD 23.ed. 535.3

Jane Lessa Monção - CRB 9/1173

GABRIEL ANTONIO FLIZIKOWSKI SIQUEIRA

DESLOCAMENTO TERMOELÁSTICO E EFEITOS DE BORDA DETECTADOS POR ESPELHO FOTOTÉRMICO E INTERFEROMETRIA

Tese apresentada à Universidade Estadual de Maringá, como requisito parcial para a obtenção do título de doutor.

Aprovado em: Maringá, 10 de fevereiro de 2023.

BANCA EXAMINADORA

_____

Prof. Dr. Nelson Guilherme Castelli Astrath
Universidade Estadual de Maringá – UEM

_____

Prof.ª Dr.ª Andressa Novatski
Universidade Estadual de Ponta Grossa – UEPG

_____

Prof. Dr. Leandro Herculano da Silva
Universidade Tecnológica Federal do Paraná – UTFPR

_____

Prof. Dr. Robson Ferrari Muniz
Universidade Estadual de Maringá – UEM

_____

Prof. Dr. Vitor Santaella Zanuto
Universidade Estadual de Maringá – UEM

Ao Seu Jango. Meu avô. Meu pai. Meu mentor. Meu melhor amigo.

ACKNOWLEDGMENTS

This dissertation could not have been completed without the invaluable contributions of many individuals. I would like to start expressing my sincerest gratitude to my supervisor, Prof. Nelson Astrath, for his guidance, support and encouragement throughout this roller-coaster. I would also like to thank my co-supervisors, Prof. Luis Malacarne and Prof. Tomaž Požar, for their invaluable insights and expertise.

I am also grateful for the support and guidance of the professors of DFI, specifically Prof. Mauro Baesso, Prof. Antônio Medina, and Prof. Jurandir Rohling.

I would like to extend my gratitude to all the staff of DFI/PFI, particularly Mônica Loiola, for their support and hard work. I am also grateful to Márcio Babata of the mechanical workshop for his numerous help.

This work would not have been possible without the financial support of Capes, CNPq, Fundação Araucária, and UEM.

Lastly, I would like to thank my beloved family, my namorida Kim, my cat Mikaela, my colleagues and friends Vitor and Otávio, for their unwavering support and encouragement throughout this journey.

This dissertation is dedicated to all of you.

“There is nothing like looking, if you want to find something. You certainly usually find something, if you look, but it is not always quite the something you were after.”

J.R.R. Tolkien, The Hobbit

CONTENTS

RESUMO

Um método óptico combinado do tipo *pump-probe* é proposto para investigar as propriedades físicas de metais, usando a detecção do deslocamento termoelástico da superfície induzida por laser por meio de medições simultâneas de Espelho Fototérmico e Interferometria. O deslocamento é monitorado pela análise das distorções da frente de onda dos feixes de prova refletidas da superfície da amostra. As propriedades físicas são obtidas fazendo a análise dos transientes juntamente com as descrições numéricas do deslocamento termoelástico e do aumento de temperatura na amostra e no ar ao redor. A influência dos efeitos de borda na mudança de fase fototermicamente induzido medido por um interferômetro também é demonstrada e comparada com descrições teóricas do deslocamento termoelástico da superfície de metais. A geometria finita das amostras é crucial para determinar a distribuição da temperatura no material e seu efeito nas medições do deslocamento de fase do interferômetro. A mudança no caminho óptico devido à deformação termoelástica e à lente térmica no ar são decodificadas a partir do sinal interferométrico usando ferramentas analíticas e numéricas. Os efeitos de borda se mostraram cruciais para descrever adequadamente os sinais interferométricos e as ferramentas de detecção desenvolvidas fornecem uma base para o estudo dos efeitos de tamanho finito no transporte de calor em materiais opacos e são aplicáveis a mecanismos de detecção similares em tecnologias de base fototérmica.

ABSTRACT

A combined pump-probe optical method is proposed to investigate physical properties of metals by demonstrating single-shot simultaneous laser-induced thermoelastic surface displacement detection by concurrent measurements using Photothermal Mirror and Interferometry. Surface displacement is probed by analyzing the wavefront distortions of the probe beams reflected from the sample's surface. Physical properties are retrieved through transient analysis in combination with numerical descriptions of thermoelastic displacement and temperature rise in the sample and surrounding air. The influence of edge effects on the photothermally-induced phase shift measured by a homodyne quadrature laser interferometer is also demonstrated and compared with theoretical descriptions of thermoelastic surface displacement of metals. Finite geometry of the samples is crucial in determining the temperature distribution across the material and its effect on the interferometer phase shift measurements. The optical path changes due to thermoelastic deformation and thermal lens are decoded from the interferometric signal using analytical and numerical tools. Edge effects are found to be crucial to properly describe the interferometric signals and the tools developed provide a framework for the study of finite size effects in heat transport in opaque materials and are applicable to similar detection mechanisms in photothermal-based technologies.

Part I

Background

CHAPTER 1

INTRODUCTION

Advancing and developing new technologies in the field of material science are crucial to gain a deeper understanding of material properties, such as thermal and optical. One set of methods that is commonly used to study these properties is based on the photothermal techniques, which detects thermal waves generated by the absorption of light by a material [1].

All-optical pump-probe methods are advanced strategies for non-destructive material characterization. They detect the effects caused by the interaction between light and matter, and the results obtained depend on the material's ability to convert light into both radiative and non-radiative processes. A benefit of these methods is that they do not require physical contact with the material, allowing for the characterization of thermal, optical, and mechanical properties of solids. Examples of these methods include photothermal mirror spectroscopy and interferometry. Photothermal mirror spectroscopy can detect deformation of the illuminated surface by analyzing the focusing or defocusing of the reflected probe beam in the far-field region [2–4]. Some interferometry methods can measure out-of-plane surface displacement [5–7], which can be detected using a homo-

dyne quadrature laser interferometer [8, 9].

The dynamic events that follow light absorption on the surface of the inspected material contain information on the structure of matter, its geometry, and its physical and thermoelastic properties. The temperature changes resulting from optical absorption are responsible for generating thermoelastic disturbances that can be detected on the surface of the sample. These disturbances can provide characteristic signatures of defects and shape of the system that can be exploited experimentally in several different ways [10].

The edge effects, such as lateral heat flow confinement or the elastic waves reflections from the sample's surfaces, can become significant when the heat diffusion flow is laterally halted or when the disturbances reflect from the edges and return to the detection site [11]. In many photothermal interferometric methodologies, simplified heat transfer treatments are feasible in applications where the diameter of the sample is much larger than its thickness. This approximation minimizes the edge effects and the system can be modeled properly using (semi)analytically solvable, one-dimensional formulations. However, in cases where the system is finite, a three-dimensional numerical description of the heat propagation and the corresponding thermoelastic deformation is required [12].

The core of this work can be divided into two parts. In the first, a new approach for photothermal detection is presented that utilizes a combined pump-probe method for detecting laser-induced thermoelastic surface displacement that was tested in metals. The method involves the simultaneous use of both photothermal mirror and interferometry techniques. A continuous wave excitation laser beam is employed to induce surface displacement in the sample by generating heat through surface optical absorption. As the heat propagates to the surrounding air, it causes a change in the refractive index of the air, resulting in a thermal lens effect. Both techniques probe the surface displacement of the sample and the thermal lens effect in the fluid by analyzing distortions in the wavefront of the probe beams reflected from the surface of the sample. The in-

terferometer method detects the out-of-plane surface displacement and thermal lens effect at a single location on the surface, while the photothermal mirror technique detects the total laser-induced phase shift on the surface of the sample and in the surrounding air.

The second part of this work for focuses on the edge effects that occur under laser-induced surface displacements of solids measured by optical interferometry. The interferometer is a tool used to detect laser-induced thermoelastic surface displacement in metals under continuous laser excitation. When the light is absorbed by the surface of the sample, it generates heat which builds up and dissipates within the material and out to the surrounding air. The specific geometry of the samples plays an important role in determining how the temperature is distributed throughout the material and how this affects the interferometer phase shift measurements. The changes in the optical path caused by the thermoelastic deformation of the surface and the thermal lens effect in the air are decoded from the interferometric signal using a combination of semi-analytical and numerical techniques. The boundary (or edge) effects of the samples were found to be significant when describing the interferometric signals. The techniques developed in this study can also be applied to other photothermal-based technologies that employ similar detection mechanisms.

This work begins by presenting two introductory chapters exploring the foundations of photothermal techniques and its applications (Chapter 2) and interferometry (Chapter 3). The core chapters include the investigation of the coupling between the photothermal mirror and interferometry as a new tool (Chapter 4) and the examination of edge effects in the photothermal displacement detected by photothermal interferometry (Chapter 5). The work concludes with a summary of the results obtained and the main conclusions (Chapter 6) along with potential research directions that could be pursued based on the knowledge gained so far.

CHAPTER 2

PHOTOTHERMAL EFFECT AND DETECTION TECHNIQUES

2.1 The photothermal effect

The photothermal effect is a phenomenon that occurs when a material or substance absorbs electromagnetic radiation, causing it to heat up. The radiation that excites the sample can be originated from different regions of the electromagnetic spectrum, for example, x-rays, the ultraviolet, infrared or microwave regions, or simply in the visible part of the spectrum. This effect, in short, is the conversion of light energy into thermal energy [1, 13].

The photothermal effect is a widely studied phenomenon with many practical applications. For example, it is used in thermal imaging, where infrared radiation is used to detect temperature differences in an object. In the field of medicine, it is used to destroy tumors by heating them with laser light. In material science, the photothermal effect is used to study the thermal properties of materials, such as thermal conductivity, thermal diffusivity, and thermal expansion. In general, the photothermal effect is a versatile and powerful tool for a wide range of appli-

Figure 2.1: Railway track expansion joint in continuous welded rail within Hayle railway station, UK [14].

cations, from scientific research to industrial processes.

The generation of heat through the absorption of light is a physical phenomenon that is present in everyday life. For example, in the Brazilian summer, an individual walking under the intense sun may experience the generation of heat on the skin as a result of the absorption of sunlight. Additionally, in colder regions of the country, it is common to find homes equipped with wood-burning stoves that are used for both cooking and as a source of heat, particularly during the freezing winter nights. In the first scenario, the skin absorbs a portion of the sun's radiation, converting it into heat. In the second scenario, the stove emits infrared radiation, which when absorbed by the surrounding environment results in heating. In both cases, the generation of heat by the object that absorbs the radiation (either the skin or the environment) occurs faster than its dissipation, resulting in an increase in temperature until thermal equilibrium is reached.

Certain photothermal effects have implications in various fields, such as construction. For example, the presence of expansion joints in railroad tracks or bridges (refer to Figure 2.1). These are small gaps that are deliberately left between specific rail segments to accommodate for expansion during hot weather

Figure 2.2: Buckling of railway track due to thermal expansion on an abnormally hot day causing [15].

days. On such days, the rail tracks, typically made of steel alloy, absorb light energy from the sun and convert it into heat, causing an increase in temperature and subsequently resulting in expansion of the rails. In the absence of these expansion joints, the thermal expansion caused by the increase in temperature can lead to excessive stress on the rails, resulting in deformation of the tracks (also called buckling) that could potentially cause derailment of railcars (refer to Figure 2.2).

2.2 The photothermal signal

Heating a sample through the absorption of radiation leads to changes in its temperature, as well as changes in other physical properties such as pressure and density. The various experimental techniques that measure these changes in properties resulting from the heating generated by light absorption are collectively referred to as photothermal methods [1] (refer to Fig. 2.3).

The dynamics of the signal that is monitored by a particular photothermal technique are contingent upon the behavior of heat flow as it propagates through the sample under investigation. In other words, the photothermal signal is in direct correlation with the thermo-optical and mechanical properties of the sample,

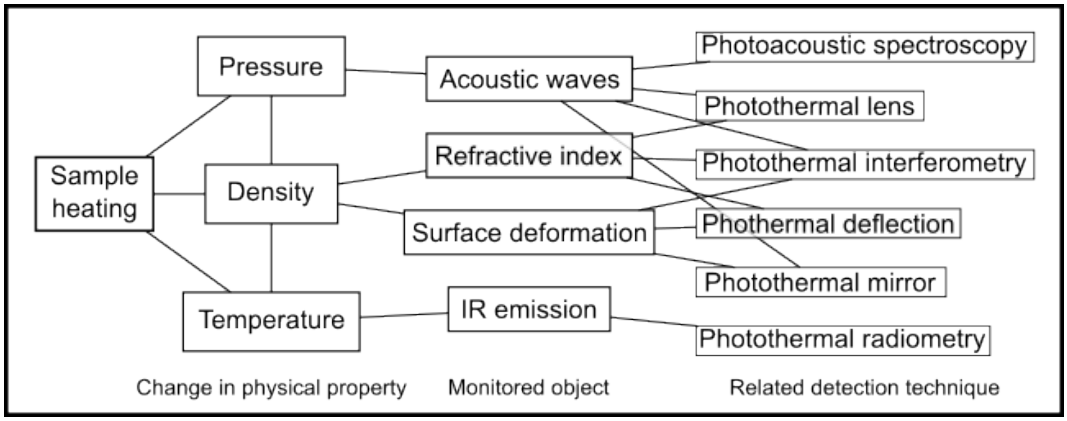

Figure 2.3: Illustration of the various phenomena that can be measured for each physical parameter affected by heat propagation, and the range of detection techniques available for such measurement.

including, but not limited to, specific heat, thermal conductivity, density and optical absorption. Due to this correlation, photothermal methods have been utilized to measure a plethora of physical parameters of solid, liquid, or gaseous samples, such as the thermal diffusivity coefficient and the speed of sound within the medium.

The fundamental principle underlying the generation of a photothermal signal is, in general terms, comprised of the following processes: optical absorption, thermal relaxation, and signal generation [1]. These processes will be discussed in detail in the subsequent sections.

2.2.1 Optical absorption

A source of electromagnetic radiation, which may be either visible or non-visible and typically originates from a laser source, illuminates a sample. A portion of this radiation is reflected, a portion may be transmitted, and a portion is absorbed. The absorbed portion induces a perturbation in the thermodynamic state of the sample, resulting in an increase in its internal energy. The sample, now in an excited state, seeks to return to equilibrium through relaxation mechanisms that ultimately result in heating of the sample due to heat generation (for an schematic illustration, see Fig. 2.4).

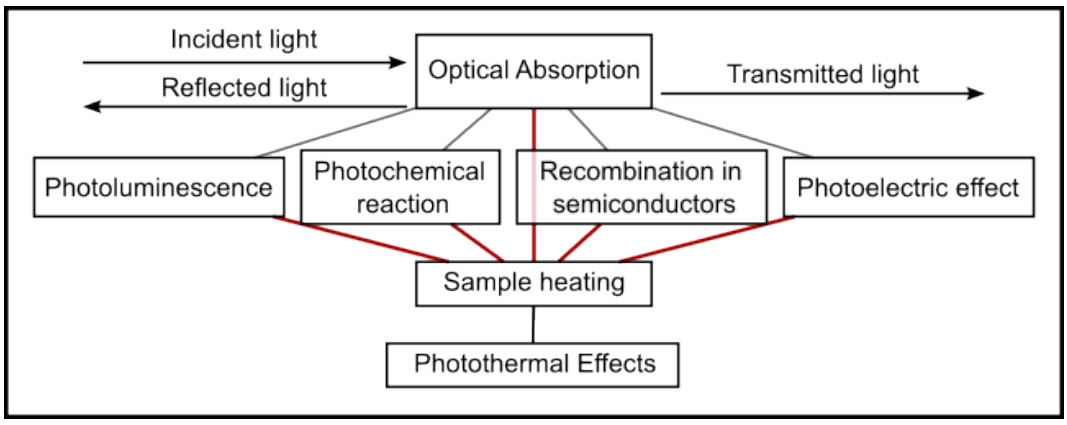

Figure 2.4: Schematic representation of the physical processes involved in the generation of a photothermal effect, including the initial process of light absorption and subsequent heating generation, which may also include intermediate processes before reaching equilibrium.

2.2.2 Thermal relaxation

Once in the excited state, and depending on the optical and electronic properties of the sample, the molecules and atoms of the sample may follow various pathways until returning to the ground state. For instance, it is possible that a portion of the energy is emitted as radiation at other wavelengths (photoluminescence phenomena). Additionally, in the presence of energy-retaining metastable states, heating may be delayed. Another possibility is the initiation of chemical reactions, which not only result in heat generation, but also may lead to modifications in the optical and thermal properties of the reaction products, thereby altering the absorption and relaxation dynamics of the sample. Furthermore, if the temperature rise is too rapid, there may be a sudden expansion (or contraction) of the region under excitation, inducing a density variation that can lead to the propagation of acoustic waves through the material.

In the context of semiconductor materials, the irradiation of light with energy equal to or greater than the characteristic band gap results in the formation of electron-hole pairs. Electrons from the valence band are excited to the conduction band, creating electronic holes. Photoexcited electrons may relax radiatively or non-radiatively, releasing energy in the form of phonons in the crystal lattice.

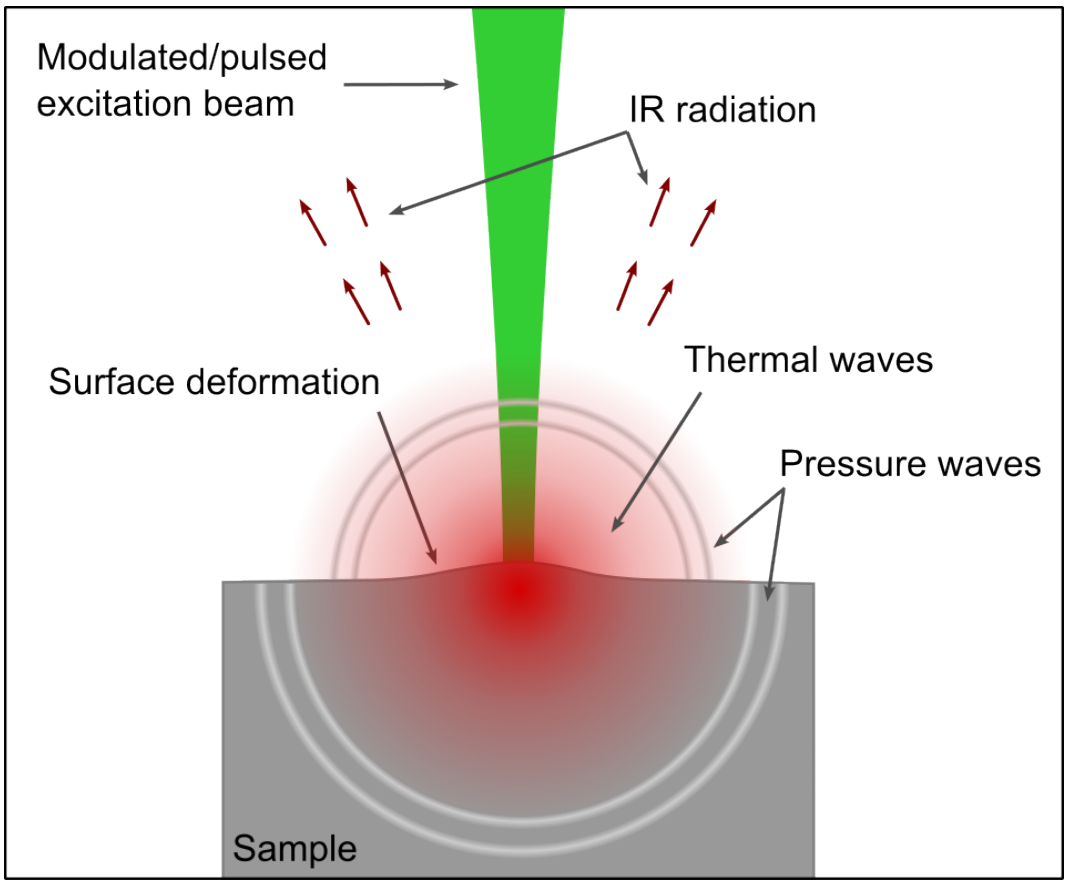

Figure 2.5: Graphical representation of the different effects that can be employed to detect photothermal signal.

This leads to a distribution of heat and, as a consequence, a rise in temperature.

2.2.3 Signal detection

Signal detection by photothermal methods entails monitoring specific physical parameters that have been altered due to the temperature increase resulting from the absorption of radiation. In general, the temperature change can be monitored directly or indirectly by observing the generated acoustic waves, the change in refractive index in the case of transparent materials, infrared emission, thermal coupling between the sample and the surrounding fluid, or even the deformation caused by thermal expansion of the material (Fig. 2.5).

The various photothermal methods are distinguished by the manner in which the signal is detected. For instance, some methods measure changes in re-

fractive index while others measure changes in pressure or thermal expansion (Fig. 2.3).

The basic experimental apparatus, commonly employed in the majority of photothermal methods, comprises the following components: an excitation light source (lamp or laser), a sample, a detector of the photothermal effect - for remote (non-contact) methods this is another laser source (probe laser), or in the case of contact methods these are devices such as pyroelectric sensors, thermocouples or thermistors -, some form of filter for the probe laser, a photodetector that converts the probe beam light into an electrical signal, and finally, the electronic equipment that receives and processes the signal.

2.3 Methods of photothermal detection

In the following section, a short examination of various experimental methods employed in photothermal signal detection will be presented. The discussion will cover particularities of each method, as well as the conditions under which they are most utilized. The intent of this section is to provide a general understanding of the different techniques available for photothermal signal detection and to aid in the selection of the most appropriate method for a given experimental scenario.

2.3.1 Photoacoustic spectroscopy

Photoacoustic Spectroscopy (PAS) is a spectroscopic technique that uses the photothermal effect to study the absorption of light in different materials. The photothermal effect was first observed in the photophone (Fig. 2.6), a telecommunication device invented by Alexander Graham Bell in 1880 [17]. When modulated light fell on a closed cell filled with different materials (solid or gaseous), it was possible to hear sounds using a tube connected to the cell. The more the material absorbs inside the chamber, the greater the intensity of the sound heard. This phenomenon, known as a photoacoustic signal was observed by

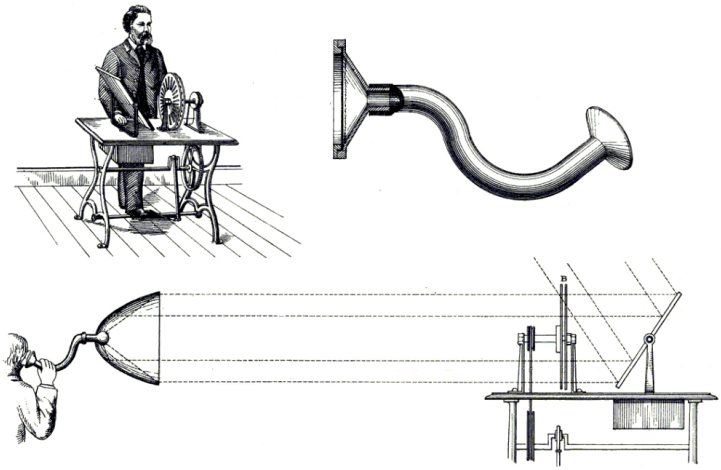

Figure 2.6: Diagrammatic representation of Bell's photophone and associated experiments for the transmission and reproduction of sound utilizing sunlight [16].

Bell but was not widely used due to the difficulty of obtaining quantitative results.

The real potential of the photoacoustic effect was not realized until the development of acoustic sensors such as microphones and piezoelectric crystals. With these tools, researchers were able to study the absorption of light in different substances. However, the major step in the use of the photoacoustic effect as a spectroscopic method came only with the presentation of a standard model of photoacoustic cell by Parker [18], Rosencwaig and Gersho [19, 20] (refer to Fig. 2.7). These researchers developed a theoretical model for the phenomenon and experimentally demonstrated that heat flow between the sample surface and the surrounding gas was the main signal generation mechanism.

Today, PAS is used in a variety of applications, including the study of gases, solids, and liquids. It is based on a range of different models that describe the interaction of electromagnetic radiation with matter, including thermal expansion,

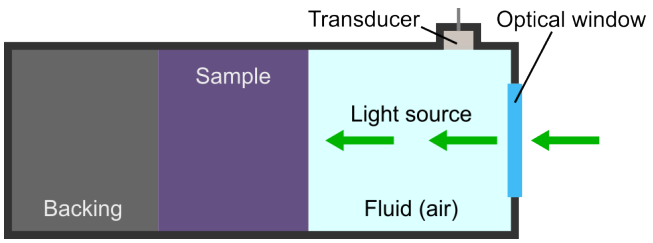

Figure 2.7: Depiction of the layout of a photoacoustic cell. Adapted from [21].

thermoelastic bending, thermal diffusion, and the thermobaric effect. PAS has proven to be a valuable tool for researchers in fields such as chemistry [22], biology and medicine [23], and continues to be an active area of research and development [24].

2.3.2 Thermal lens spectroscopy

Thermal Lens Spectroscopy (TLS) was the first photothermal method used for chemical analysis of substances [1, 25]. The principle of operation of TLS is as follows: A sample is illuminated by a laser beam, typically of radial Gaussian profile. Some of the light is absorbed by the sample, resulting in a temperature rise. This temperature rise is greater at the center of the illuminated region than along the radial direction, thereby creating a temperature gradient in the sample (refer to Fig. 2.8). This temperature gradient induces a refractive index gradient within the sample. As a result, the illuminated region behaves as a lens that can alter the intensity of a laser beam propagating through the sample. The center of the beam can either increase or decrease in intensity, depending on the optical and thermal properties of the sample, such as the refractive index temperature coefficient (dn/dT). It is this lensing effect that gives TLS its name. The thermal lensing phenomenon was first observed by Gordon et al. [26] while investigating the Raman spectrum of dyes inserted into a laser cavity. They detected a transient variation in the intensity of the center of the beam associated with an increase in its divergence when samples were inserted, and proposed that the temperature increase in the sample due to light absorption also causes a change in the refractive index of the liquid, thereby influencing the laser propagation inside.

Over the years, the experimental setup of TLS and the theoretical models describing the phenomenon have evolved. Initially, early experiments were performed inside a laser cavity, as reported by Gordon et al. [26]. Subsequently,

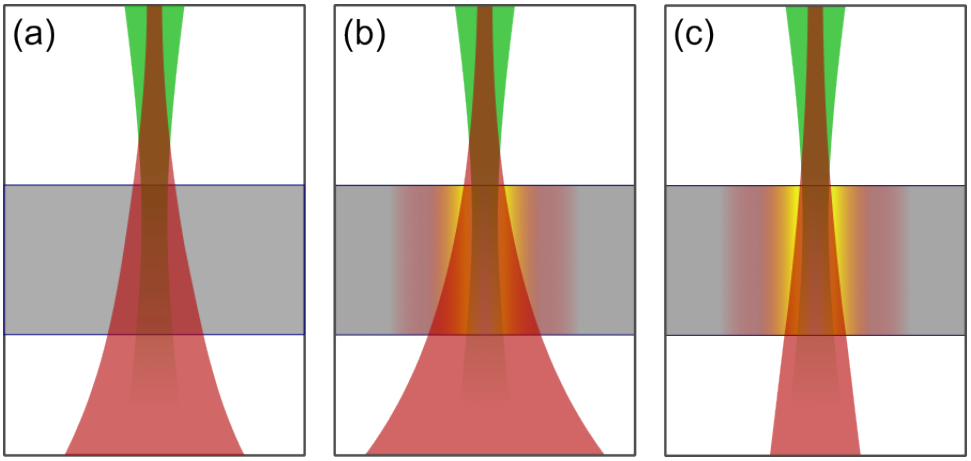

Figure 2.8: Illustration of (a) the instant immediately after excitation beam illuminates the sample. No change in the probe beam is detected yet. Illustration (b) and (c) shows the temperature gradient inducing a refractive index change within the sample. The illuminated region then behaves as a divergent and convergent lens, respectively, that alters the intensity of a laser beam propagating through the sample.

researchers began positioning the sample outside the cavity, along the focal region of a lens, which significantly increased the sensitivity of the experiments, as demonstrated by Hu and Whinnery [27]. Another important advancement was the use of an additional laser, with one laser beam being utilized exclusively to generate the thermal lens effect, and another used solely to monitor the effect. Both beams were arranged collinearly, with the aid of optical elements such as mirrors and beam splitters, as described in Fang and Swofford [28]. Presently, the most commonly employed configuration in experiments is the mismatched mode. In this configuration, the excitation and probe beams travel along individual paths and strike the sample with different beam sizes, further increasing the sensitivity of the experiment. The theoretical model for this configuration was popularized by Shen et al. [29], enabling steady-state or time-resolved measurements to be obtained. More recent work presents even more extensive models as reported in Refs. [30–32].

2.3.3 Photothermal z-scan

The z-scan technique, which was first developed by Sheik-Bahae et al. [33] for measuring optical nonlinearities in transparent samples, has been widely used as a method for measuring the nonlinear refractive index of materials. Additionally, it has been demonstrated that photothermal z-scan is a complementary technique to TLS, as it can also be used to investigate the thermal diffusivity of absorbing samples [34]. The z-scan technique is based on the measurement of the transmission of a focused laser beam through a sample as a function of the distance (z) of the sample relative to the beam focus position. By performing z-scan measurements on a sample, one can determine not only the nonlinear refractive index of the sample, but also other significant optical properties such as the nonlinear absorption coefficient and the two-photon absorption cross section, for example.

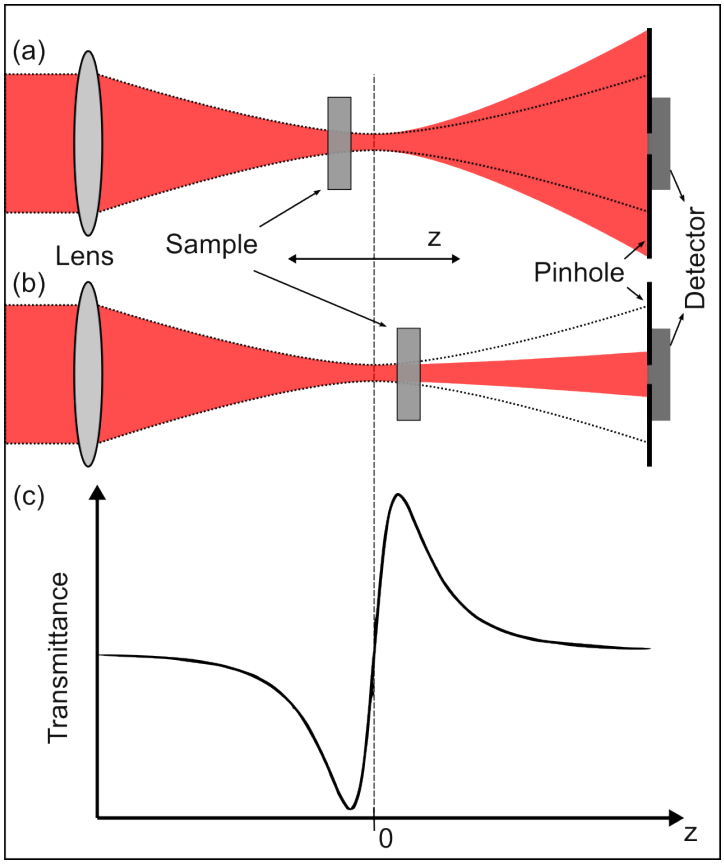

Figure 2.9: Illustration of the lens effect in the Z-scan technique. For the case of a positive nonlinear refractive index if (a) the sample is positioned before the focus, it will result in the beam expanded at the position of the aperture, whereas if (b) the sample is after the focus, it will result in the beam more collimated at the aperture. Dotted lines represent the beam when no sample is present. The result of the normalized transmittance when moving the sample in the z-direction is shown in (c). Adapted from [35].

In order to obtain information about nonlinear absorption, the entirety of the transmitted energy is collected, typically referred to as the open aperture mode. Conversely, information about nonlinear refraction is yielded by collecting the transmitted energy through an aperture centered on the beam in the far field, referred to as the closed aperture mode. By moving a sample through the focus of a Gaussian beam and measuring the transmittance on-axis and in the far-field, a characteristic curve can be obtained (refer to Fig. 2.9). This curve directly indicates the type and magnitude of the nonlinear optical response [36].

2.3.4 Photothermal radiometry

Photothermal Radiometry (PTR) is a technique used for monitoring changes in the emission of thermal radiation by a sample as it is heated in a modulated manner. The technique was first proposed by Nordal and Kanstad in 1979 [37]. In PTR, the emission in the infrared spectrum is monitored, allowing for the reliable detection of temperature changes. In the early days of PTR, measurements of absolute absorption coefficients were difficult to obtain. However, researchers such as Tam and Sullivan [38], were able to make such measurements using intense pulsed lasers.

One of the key advantages of PTR is its ability to provide remote sensing in a single-ended manner, making it an important tool for many industrial applications. A typical PTR experiment involves the use of a continuous modulated or pulsed monochromatic light beam, which is absorbed by the sample and converted into heat. This heat induces changes in the thermal radiation emitted by the sample, which depend on its thermal and optical properties.

The emitted radiation is collected by a set of optical elements appropriate for the infrared region and directed to a photodetector also suitable for the infrared, typically a liquid nitrogen cooled mercury cadmium telluride (MCT) detector (see an common configuration illustrated in Fig. 2.10). A system of optical filters is po-

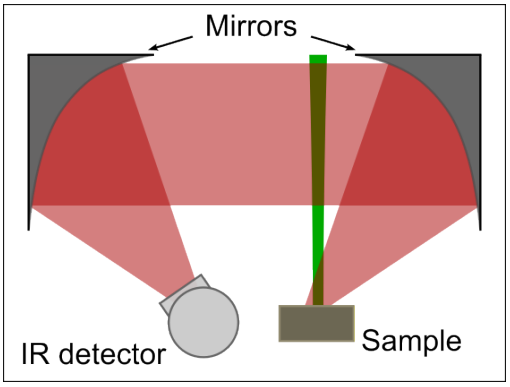

Figure 2.10: Illustration of a common configuration of a photothermal radiometry experiment. Adapted from [39].

sitioned next to the detector to prevent the passage of scattering. The modulated signal is extracted with help of a lock-in amplifier and recorded as a function of incident wavelength, allowing PTR to provide a spectrum corresponding to the optical absorption of the sample.

The temperature variation in PTR depends on the sample properties and the modulation frequency of the excitation light. Therefore, the model for PTR is very similar to the model proposed by Rosencwaig and Gersho for PAS. The thermal radiation emitted by the sample is related to the corresponding temperature change by the Stefan-Boltzmann law

$$W = \varepsilon \sigma T_0^4, \tag{2.1}$$

where, $\sigma = 5.67 \times 10^{-12}$ W.cm^{-2}K^{-4} is the Stefan-Boltzmann constant, ε is the samples' emissivity and T_0 the initial surface temperature. One can correlate any changes in the thermal emission of a sample by the following expression

$$\delta W = 4\varepsilon \sigma T_0^3 \delta T_0, \tag{2.2}$$

which means, to a first order, any changes in the samples' temperature due to the modulated excitation results in a change in the emission of IR radiation. The quantity in Eq. (2.2) when multiplied by the area A of the detector corresponds to

the change in the incident power arriving at the detector δP.

$$\delta P = 4Ag\varepsilon\sigma T_0^3 \delta T_0 \tag{2.3}$$

where g is a geometric parameter.

2.3.5 Photothermal deflection

Spatial variation of refractive index in a material can alter the path of light propagating through it, such as in the case of temperature gradient in thermal lens spectroscopy. When this deflection or deviation is monitored, it can be used to detect thermal waves generated within the material. Researchers Boccara, Fournier, and Badoz [40, 41] observed that the heat diffused through a material due to the photothermal effect causes a change in the refractive index of a fluid layer near the surface of a sample when it is optically excited. This is the principle behind the Mirage Effect, in which a laser beam directed parallel and very close to the surface is used to monitor beam deflection due to the change in refractive index and obtain the optical properties of solid samples (refer to Fig. 2.11).

The temperature rise at the surface depends on the material's thermal and optical properties, such as its optical absorption and thermal diffusivity, which can be studied as a function of the excitation wavelength. This allows for not only the thermal characterization of unknown materials but also the use of the beam

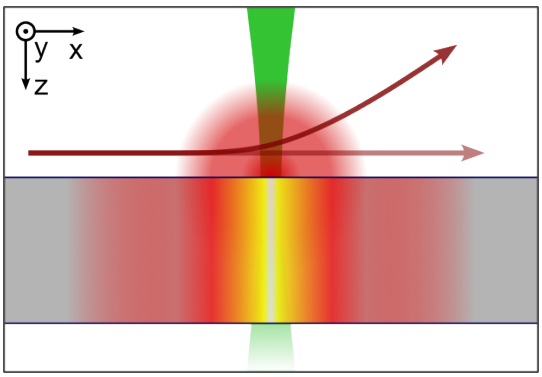

Figure 2.11: Illustration of the popular configuration of mirage effect used in beam deflection methods.

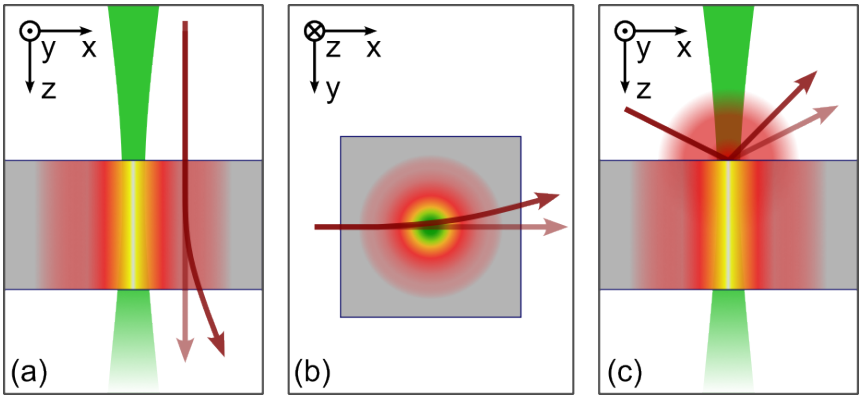

Figure 2.12: Illustration of additional configurations of the Photothermal Deflection: (a) Transmission Photothermal Deflection, (b) Internal Transverse Photothermal Deflection and (c) Reflection Photothermal Deflection.

deflection as spectroscopic photothermal method.

There are several experimental configurations of the Photothermal Deflection method. The Transverse Photothermal Deflection (Fig. 2.11), or just Mirage Effect, for simplicity, is the most used in the characterization of materials. Other configurations of photothermal deflection include Transmission Photothermal Deflection (Fig. 2.12(a)), Internal Transverse Photothermal Deflection (Fig. 2.12(b)) and Reflection Photothermal Deflection (Fig. 2.12(c)). The properties of the samples under investigation can typically be obtained by analyzing the behavior of the deflection signal intensity as a function of the optical excitation frequency or over time.

2.3.6 Photothermal mirror

The Photothermal Mirror (PTM) technique is a method that has been utilized to study both transparent and opaque solid samples. This approach involves focusing an excitation beam onto the surface of a solid, which leads to the absorption of radiation and the conversion of this energy into heat. This heat results in expansion of the illuminated region on the surface of the sample, creating a deformation that behaves like a mirror for a reflected test beam. The shape of this deformation, which can be either convex or concave, depends on the linear

thermal expansion coefficient of the sample. The magnitude of the deformation is directly proportional to the optical absorption coefficient and linear thermal expansion coefficient of the sample, and its time evolution is influenced by the heat conduction properties of the material. By measuring the strain, it is possible to gain insights into the thermal, optical, and mechanical properties of the sample. This method will be discussed in more detail further.

2.3.7 Photothermal interferometry

The Thermal Lens effect was discovered and a few years later, researchers realized that the photothermal-induced refractive index change could be measured through other methods. The absorption of light in a sample and the subsequent heating and refractive index changes would result in a phase shift in the light passing through the heated region, which means this phase shift could be detected with an interferometer [42,43]. The use of an interferometer to measure refractive index changes was not new, but the method of using an excitation laser to heat the sample while simultaneously monitoring the refractive index change was innovative [1].

The photothermal effect can be detected through changes in the optical path length, which can be measured using interferometry. This technique involves comparing the phase of monochromatic light passing through the heated sample to the phase passing through a reference arm, resulting in a change in power at a photoelectric detector. There are various interferometric setups that fall under the category of photothermal interferometry, all of which can be used to detect changes in the optical path length caused by the photothermal effect.

A brief review of optical interferometry will be presented in the next chapter.

CHAPTER 3

INTERFERENCE

3.1 The fundamentals

Interference is a phenomenon that occurs when two or more waves interact with each other. Therefore, light, as a wave, can interfere. The term “light” commonly refers to only a portion of the electromagnetic spectrum known as visible light. The electromagnetic spectrum is divided into various ranges based on different characteristics of transmission, emission, and absorption, as well as various technological applications. From shortest to longest wavelengths, the spectrum is divided into: gamma rays, x-rays, ultraviolet radiation, visible light, infrared radiation, radar waves, microwaves, television waves, and radio waves (see Fig. 3.1). It is worth noting that visible light is a small portion of the electromagnetic spectrum, ranging from violet to red in color and approximately 400 to 750 nm in terms of wavelength.

Interference is a result of the superposition of waves, which leads to the creation of a new wave that is the sum of the individual waves. This process can lead to constructive or destructive interference, depending on the relative phase

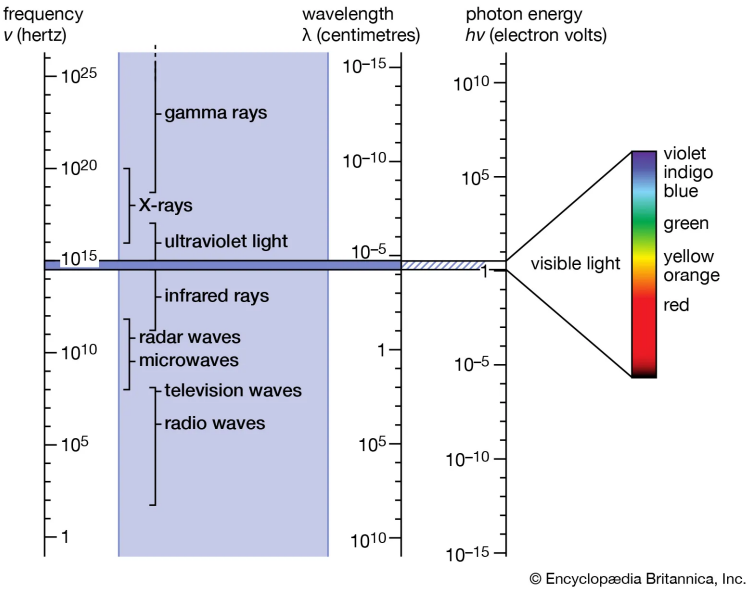

Figure 3.1: The electromagnetic spectrum. Visible light is only a small portion of the entire spectrum ranging from violet to red in color and approximately 400 to 750 nm in wavelength [44].

of the waves. Constructive interference occurs when the waves are in phase and their amplitudes add together, resulting in a stronger wave (i.e. with greater amplitude). Destructive interference, on the other hand, occurs when the waves are out of phase and their amplitudes cancel each other out, resulting in a weaker wave (i.e., with smaller amplitude). Figure 3.4, in next section, illustrates this property of waves. Light interference is an important concept in optics and is used in a variety of applications in holography [45, 46], astronomy [47–50], and the study of thin films [51–53]. This chapter will discuss the basic principles of light interference, the conditions under which it occurs, and present different optical interferometry apparatuses as measurement tools.

3.2 Interference intensity

Light is a transverse electromagnetic wave that propagates through space. It is characterized by the perpendicular variation of electric and magnetic fields. In order to mathematically analyze the propagation of light waves, it is useful to

consider only the real component of the electric field of the wave, as the magnetic field will always be perpendicular to the electric part. When an electromagnetic field oscillates within a plane perpendicular to its direction of propagation (in this case, the z direction), it is said to be linearly polarized in that plane. As such, the electric field of a monochromatic wave can be described by a time-varying scalar function, $E(z,t)$, as follows:

$$E(z,t) = E_0 \cos[2\pi(z/\lambda - \nu t)], \tag{3.1a}$$

$$= E_0 \cos[kz - \omega t]. \tag{3.1b}$$

The amplitude of the electric field of the wave is represented by E_0. The angular frequency of oscillation is given by $\omega = 2\pi\nu$, where ν is the time frequency (or simply frequency). The wavenumber k, sometimes referred to as the spatial frequency, is related to the wavelength λ by the equation $k = 2\pi/\lambda$. The cosine argument in the equations (3.1) is known as the phase of the wave and varies with time and position along the direction of propagation. In two or three dimensions, it is possible to define a surface called the wavefront, whose phase is constant and moves with velocity $c = \lambda\nu$ during the propagation of a wave.

For practicality, we will use the complex exponential notation to represent a wave mathematically, utilizing Euler's formula $\mathrm{e}^{i\theta} = \cos(\theta) + i\sin(\theta)$. Therefore, the electric field described by Eq. (3.1) is written as the real part of the complex exponential

$$E(z,t) = E_0 \mathrm{e}^{i(kz-\omega t)}, \tag{3.2}$$

that is,

$$E(z,t) = \mathrm{Re}\left\{E_0 \mathrm{e}^{i(kz-\omega t)}\right\}. \tag{3.3}$$

Rewriting the spatial and temporal parts separately we get

$$\begin{aligned} E(z,t) &= \mathrm{Re}\left\{E_0 \mathrm{e}^{i\phi}\mathrm{e}^{-i\omega t}\right\}, \\ &= \mathrm{Re}\left\{\widetilde{E}_0 \mathrm{e}^{-i\omega t}\right\}. \end{aligned} \tag{3.4}$$

Here, we introduce the variable $\phi = kz = 2\pi z/\lambda$ and the term $\widetilde{E}_0 = E_0 \mathrm{e}^{i\phi}$, which is referred to as the complex amplitude of E. This representation of the electric field can be visualized in the Argand-Gauss diagram using phasors. In Fig. 3.2, for instance, is the phasor diagram of an arbitrary electric field $E = E_0 \mathrm{e}^{i(\phi+\omega t)}$. The electric field is the projection onto the real axis of a vector with an amplitude of E_0 and an initial phase of ϕ, followed by a counterclockwise rotation given by ωt. This representation is advantageous because the sum of several waves of the same frequency propagating in the same direction is given by the vector sum in the phasor diagram.

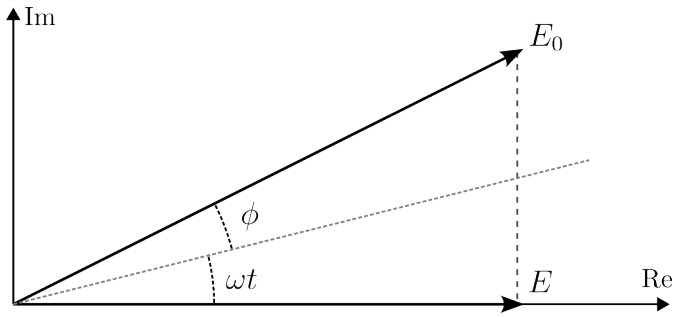

Figure 3.2: Representation of the electric field in the Argand-Gauss diagram. The real part E of the electric field is the projection of the phasor onto horizontal axis.

Interference is a characteristic of waves in general, not just electromagnetic waves. When waves are superimposed, the resulting wave can have an intensity that is higher or lower than the original waves, or there may even be total cancellation of the waves. If we consider two monochromatic waves, propagating in the same direction and with equal polarization, such that one wave differs from the

other only by an additional phase factor ϕ. Thus, we can write

$$E_1 = (E_1)_0 \cos(\omega t), \tag{3.5}$$

$$E_2 = (E_2)_0 \cos(\omega t + \phi). \tag{3.6}$$

In the case where the waves have same amplitude, we have

$$E_1 = E \cos(\omega t), \tag{3.7}$$

$$E_2 = E \cos(\omega t + \phi). \tag{3.8}$$

The superposition of these fields will result in a field that depends on the initial amplitudes and the phase factor ϕ. The vector sum of the fields E_1 and E_2 in the phasor diagram is depicted in Fig. 3.3. We can see that field E_1 is the projection onto the horizontal axis of the vector whose angle with the horizontal is ωt. Similarly, field E_2 is the projection of the vector whose angle with the horizontal is the same as that of E_1 plus ϕ. Cosine law of trigonometry gives the resultant of the vector sum $E_1 + E_2 = E_R$ in terms of ϕ

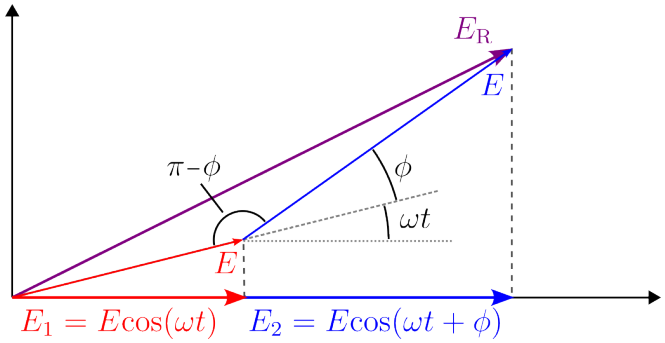

Figure 3.3: Representation of the vector sum of electric fields E_1 and E_2 in a phasor diagram. Bath have same amplitude but differ from a phase factor ϕ.

$$E_R^2 = 2E^2 - 2E^2\cos(\pi - \phi); \tag{3.9}$$

$$= 2E^2 + 2E^2\cos(\phi); \tag{3.10}$$

$$= 2E^2(1 + \cos(\phi)). \tag{3.11}$$

Where the relation $\cos(\pi - \phi) = -\cos(\phi)$ was used. Additionally, the identity given by $1 + \cos\phi = 2\cos^2(\phi/2)$ can be used to rewrite E_R as follows

$$E_R^2 = 4E^2\cos^2\left(\frac{\phi}{2}\right) \tag{3.12}$$

$$E_R = 2E\cos\left(\frac{\phi}{2}\right) \tag{3.13}$$

As shown in Fig. 3.4, it is possible to see that: (i) when the two waves are in phase, i.e. $\phi = 0$, the resulting amplitude is twice the initial amplitude (Fig. 3.4a); (ii) when they are perfectly out of phase, i.e. $\phi = \pi$, the resulting amplitude is zero (Fig. 3.4b); and (iii) when there is an intermediate phase difference, the resultant will be a wave with an amplitude between the limits described above (Fig. 3.4a).

In terms of electric field strength, an interesting fact occurs. If we consider that the field intensity is equal to the average amplitude of the Poynting vector S_{mean}, for a wave of the form $E\cos(\omega t)$, the intensity is given by

$$I = S_{\text{mean}}\ , \tag{3.14}$$

$$= \frac{E_R^2}{2\mu_0 c} = \frac{1}{2}\varepsilon_0 c E_R^2. \tag{3.15}$$

For the case where the electric field is the resultant of the superposition of two

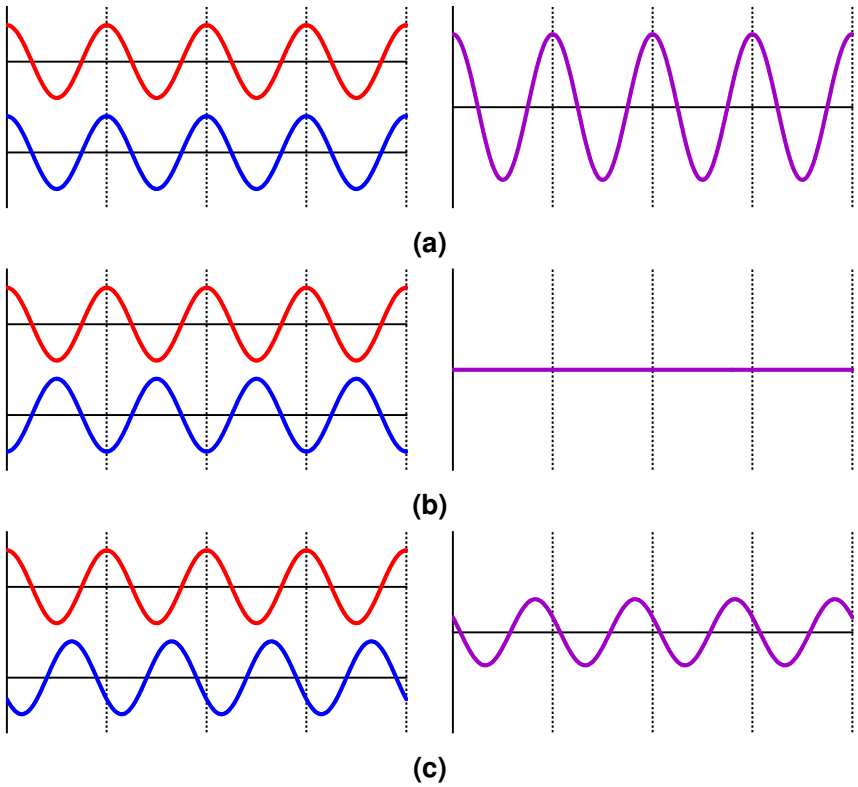

Figure 3.4: Illustration of the different situations of wave interference. (a) Constructive interference occurs when the waves are in phase ($\phi = 0$) and their amplitudes add together. (b) Destructive interference occurs when the waves are out of phase ($\phi = \pi$) and their amplitudes cancel each other out. (c) When the phase difference between the waves are somewhere between $\phi = 0$ and $\phi = \pi$ the resultant amplitude of the wave will be somewhere between the maximum amplitude of the individual waves and zero.

fields as shown in Eq. (3.13), the intensity is

$$I = 2\varepsilon_0 cE^2 \cos^2\left(\frac{\phi}{2}\right), \tag{3.16}$$

$$I = I_0 \cos^2\left(\frac{\phi}{2}\right). \tag{3.17}$$

Where $I_0 = 2\varepsilon_0 cE^2$. Notice that, if the phase difference varies linearly, therefore, the resulting intensity oscillates with the square of the cosine.

The additional phase factor ϕ can appear even in the case where two waves have the same origin, such that at the origin both had the same initial phase [54]. The phase difference between them, $\Delta\phi = \phi_2 - \phi_1 = \phi$, is, therefore, either a result of the optical path difference Δp between the waves, given by

$$\Delta p = \frac{\lambda}{2\pi}\Delta\phi \tag{3.18}$$

or the time delay

$$\tau = \frac{\Delta p}{c} = \frac{\lambda}{2\pi c}\phi. \tag{3.19}$$

The strength of the interference can be defined by a quantity called fringe visibility V [54], which is given by the following equation

$$V = \frac{I_{\text{max}} - I_{\text{min}}}{I_{\text{max}} + I_{\text{min}}}. \tag{3.20}$$

where I_{max} and I_{min} are the maximum and minimum intensity of the constructive and destructive interference, respectively. The visibility of the interference fringes, in other words, refers to how easy it is to distinguish between the light and dark regions of the interference pattern.

3.3 Interferometry

Optical interferometry has been utilized as a laboratory technique for over a century. However, it was with the invention of the laser in the mid-1960s that the use of interferometric techniques in fields such as astronomy [47], quantum mechanics [55], spectroscopy [56], biology and medicine [57] became more prevalent. For this it is necessary that an experimental apparatus has an optical arrangement in which two light waves traveling separately are set to interfere. One of these waves will serve as a reference, while the other will be used for the test being conducted. The optical path difference between the waves is determined by [54]

$$\Delta p = p_{\mathrm{r}} - p_{\mathrm{m}}. \tag{3.21}$$

The optical path traveled by the reference is given by $p_{\mathrm{r}} = n_{\mathrm{r}} d_{\mathrm{r}}$, where n_{r} is the refractive index and d_{r} is the distance traveled. Similarly, the optical path of the test wave is $p_{\mathrm{m}} = n_{\mathrm{m}} d_{\mathrm{m}}$. In order for the interference pattern to be stationary, it is necessary that the phase between the waves does not vary with time, i.e., the waves must have the same frequency. This requirement can be satisfied if the waves originate from the same source, for instance. There are two methods that can be employed to split an initial beam into two waves: wavefront splitting and amplitude splitting.

3.3.1 Wavefront splitting

The wavefront can be split by utilizing small openings, such as pinholes, to separate the light source into two beams. This method was used in Young's famous experiment (see Fig 3.5) to demonstrate the wave nature of light and is also utilized in Rayleigh interferometers, which will be briefly discussed next.

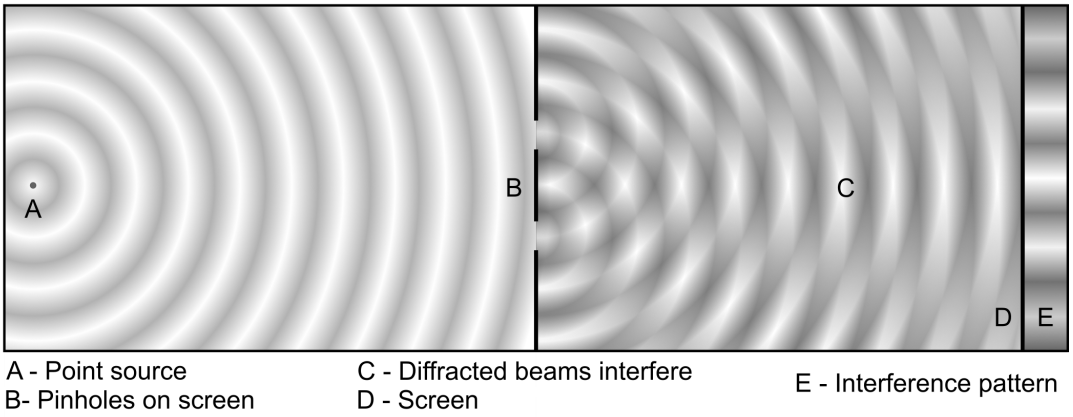

Figure 3.5: Interference of two beams originated from the wavefront splitting of a point source. Adapted from Ref. [54].

3.3.1.1 Rayleigh Interferometer

Proposed in 1896 by British physicist John William Strut, Lord Rayleigh, this interferometer employs two apertures to split the wavefront of the light source after it passes through a collimating lens, as illustrated in Fig. 3.6. The beams subsequently travel along two different optical paths and are recombined by a converging lens.

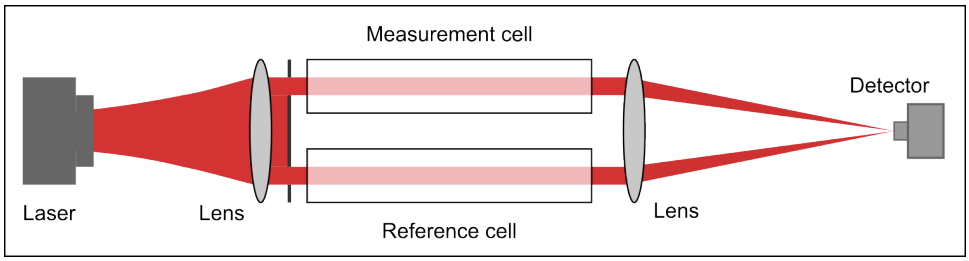

Figure 3.6: Illustration of the basic configuration of the Rayleigh interferometer. Adapted from Ref. [54].

This interferometer is relatively stable and simple to construct, although the interference fringes are very close together spatially, requiring detection instruments with high magnification power. It is primarily used to determine the refractive index of liquids and gases. The reference beam passes through a cell containing a gas of known refractive index, while the other beam passes through a cell containing the gas whose refractive index is to be determined. The number

of fringes passing through the detection point is given by [54]

$$N = \frac{(n-1)d}{\lambda}, \tag{3.22}$$

where d is the size of the gas cell. It is also possible to determine the composition of gas mixtures using this type of interferometer.

3.3.2 Amplitude splitting

In amplitude splitting, optical elements such as a diffraction grating, a beam splitter, or a polarized beam splitter are employed to separate the initial light beam into two portions of smaller amplitudes. Another optical element must then be employed to recombine the two beams in order to produce the interference pattern. This method is utilized in interferometers such as the Mach-Zehnder interferometer, the Sagnac interferometer, and the Michelson interferometer. These will be discussed shortly below.

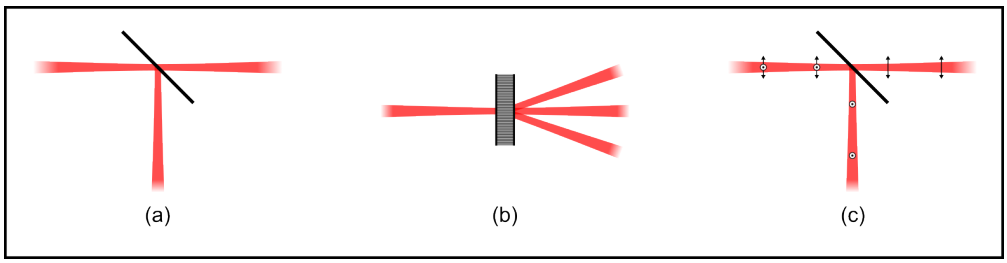

Figure 3.7: Different methods of performing amplitude splitting of light: (a) a beam splitter, (b) a diffraction grating and (c) a polarized beam splitter. Adapted from Ref. [54].

3.3.2.1 Mach-Zehnder interferometer

In 1891, Ludwig Zehnder [58] proposed an adaptation to Jamin's interferometer [59], using two beam splitters and two mirrors (see Fig. 3.8) in place of the two thick glass mirrors of the original configuration. A year later, the apparatus was improved by Ludwig Mach [60]. The main beam is split into the reference and measurement beams by the first beam splitter, both of which are reflected

by mirrors and recombined in a second beam splitter to form the interference pattern.

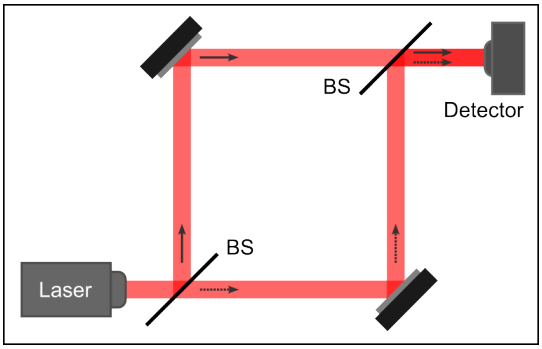

Figure 3.8: Illustration of the principle of operation of the Mach-Zehnder interferometer. The light source is separated in two portions by a beam-splitter. Reference and measurement beam are combined again by a second beam-splitter with help of a couple of mirrors. Differently than the Michelson interferometer, each beam travels each path only once.

This configuration has several advantages, including the ease of manipulating the paths traveled by simply changing the position of the mirrors and the fact that the beams travel each path only once. The Mach-Zehnder interferometer is used for studies of fluids, heat transfer, and temperature distribution in plasmas [61, 62]. It is also a popular tool for studying quantum phenomena such as quantum entanglement [63–65].

3.3.2.2 Sagnac interferometer

The Sagnac interferometer was an experimental attempt by French physicist Georges Sagnac to observe the relative effect of ether motion in 1913 [66, 67]. In this setup, shown in Fig. 3.9, both beams travel the same path but in opposite directions after being separated by the beam splitter.

A drawback of most interferometers is their susceptibility to the effects of ambient vibrations and air currents, which can cause unwanted phase variations. It is therefore often necessary to mechanically isolate the whole system. The Sagnac interferometer is particularly stable due to the fact that the path taken by the beams is the same, meaning that any disturbance caused by these effects

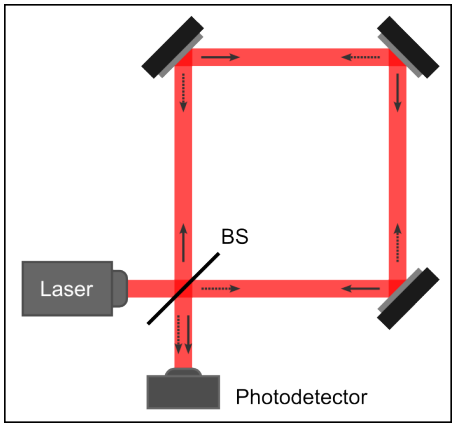

Figure 3.9: Illustration of the basic configuration of the Sagnac interferometer. Adapted from Ref. [54].

affects both beams equally. Applications include its use as a rotation detector [68, 69]. When the system as a whole is put into rotary motion, the angular velocity Ω induces a phase difference that is proportional to the angle θ that the angular velocity makes with the normal direction

$$\Delta\phi = \frac{4\Omega A}{\lambda c}\cos\theta, \tag{3.23}$$

where A is the surface area formed by the path taken by the beams, λ and c are the wavelength and the speed of light, respectively. This effect is a consequence of the difference in optical path taken by the beams propagating in opposite directions when the system is put into rotation, as the time it takes for the beams to complete the entire cycle differs, thus inducing the phase difference.

3.4 Michelson interferometer

In this work, we used an adaptation of the Michelson interferometer as the tool to perform the studies. In this section, the concept of the Michelson interferometer, its limitations, and how to overcome them using the quadrature detection method will be presented.

The Michelson interferometer is perhaps the most common setup in optical

interferometry. Conceived by American physicist Albert Michelson in the late 19th century, a beam of light has its intensity divided by a beam-splitter, as shown in Fig. 3.10. The beams travel along perpendicular paths; one travels to a reference mirror, which is static, and the other to a measuring mirror, which can be moved. Both are reflected and recombine after passing through the beam-splitter again to form the interference pattern that can be detected by photodetectors or cameras. The phase variation detected is directly related to the distance the beams travel, so this type of interferometer is often used for accurate displacement measurement. If the relative phase between the beams due to the movement of the mirrors is an integer multiple of the wavelength, constructive interference occurs, i.e., the light detected at the sensor reaches a maximum value. If the phase is a half integer multiple, the interference is destructive, and the detected light intensity is minimal.

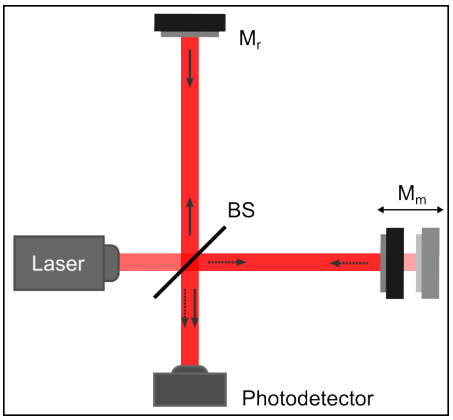

Figure 3.10: Illustration of the basic configuration of the Michelson interferometer. Adapted from Ref. [54].

Michelson's interferometer became known in the scientific community when, in 1887, Michelson and Edward Morley used it in their experiment to test the relative motion of the Earth through the supposed ether believed to be the medium through which light propagated [70]. The experiment concluded that if there were any phase variations due to the Earth moving through the ether, the displacement of the interference pattern would be less than one hundredth of a fringe, i.e., practically zero for the accuracy limit of the experiment. This result was only

understood after the publication in 1905 of Albert Einstein's Theory of Restricted Relativity. More than a hundred years later, an adaptation of Michelson's interferometer was used by the Laser Interferometer Gravitational-Wave Observatory (LIGO) to detect gravitational waves for the first time [48], validating another important implication of Einstein's theory, this time in the Theory of General Relativity.

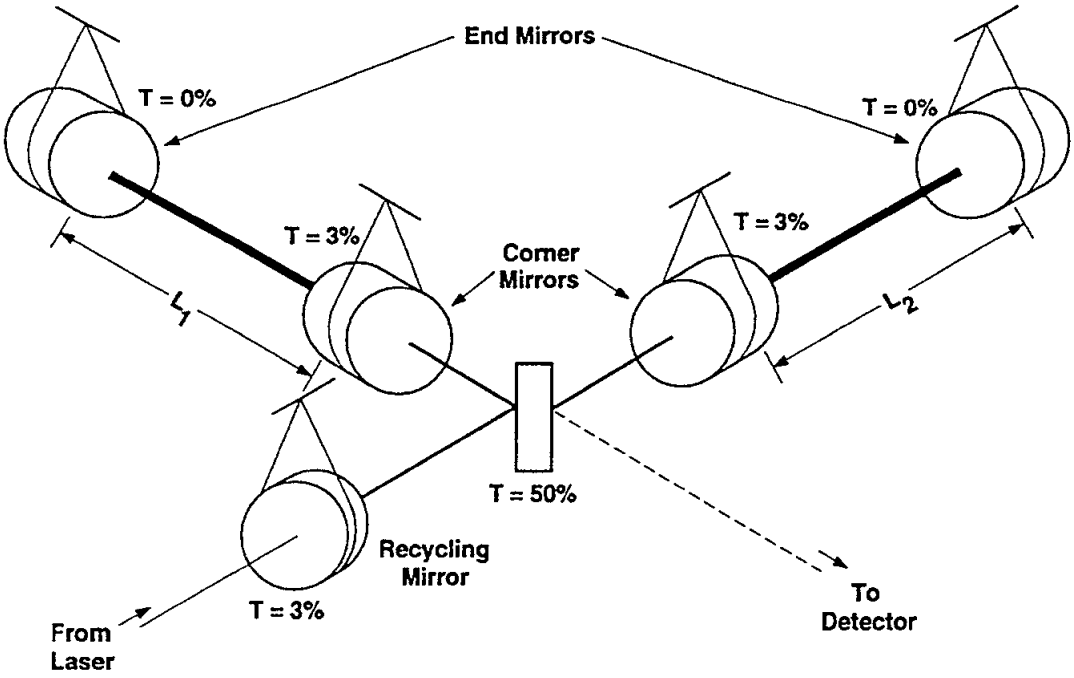

Figure 3.11: Schematic illustration of the Light Interferometer Gravitational-Wave Observatory (LIGO). Adapted from Ref. [71].

The LIGO observatory is equipped with two interferometers that operate simultaneously in different locations, approximately 3,000 km apart. The first is located in Livingston, Louisiana and the second in Richland, Washington, both in the United States. Each interferometer has a set of beam-splitters and mirrors that are attached to a system of suspended masses, as depicted in Fig. 3.11. The length of each arm is approximately 4 km and they are contained within a large vacuum chamber in order to reduce ambient noise. When a gravitational wave passes by the Earth, it causes a phase difference corresponding to a relative displacement of approximately 10^{-9} nm between the arms of the detector. To achieve such a high level of sensitivity, the interferometer arms are

also equipped with half-mirrors, which cause each arm to function as an optical Fabry-Perot cavity. This reflects the incoming light from the mirrors multiple times before it reaches the beam-splitter and the detector, effectively increasing the size of the interferometer arms by a factor of nearly 300. Sensitivity is further enhanced by the use of an additional mirror, which allows much of the light that would otherwise be returned to the source to be reused.

In a Michelson interferometer, such as the one shown in Fig.3.10, light reaching the detector, in this case a photodiode, generates a photocurrent whose corresponding voltage can be monitored by an oscilloscope. A linear displacement of the measuring mirror causes a sinusoidal variation in the intensity of the interference between the beams. Since the optical path difference accounts for the beams traveling back and forth between the interferometer arms, one complete oscillation cycle of the interference fringe corresponds to a half-wavelength shift. Therefore, the voltage observed by the oscilloscope is related to the displacement of the mirror as follows:

$$x = A_{x0} + A_x \sin \frac{4\pi u(t)}{\lambda} \tag{3.24}$$

Part II

Combinating photothermal methods

CHAPTER 4

COUPLING PHOTOTHERMAL MIRROR AND INTERFEROMETRY

4.1 Introduction

All-optical pump-probe methods are advanced techniques for general non-destructive material characterization, characterized by detecting the effects generated by the interaction between light and matter. These effects depend on the ability of the material to convert light into radiative and non-radiative processes [1].

The non-contacting nature of pump-probe methods allows accessing thermal, optical and mechanical properties of solids. These methods require reflective surfaces in order to directly detect the perturbation caused by light absorption and have to be capable of detecting probe beam wavefront deformation. Two such methods are the photothermal mirror and the interferometry [2–7]. Both are naturally similar in this sense, because they detect wavefront distortion, although employing different optical detection mechanisms.

The photothermal mirror (TM) spectrometry detects the deformation of the il-

luminated surface by analyzing the focusing or defocusing of the reflected probe beam in the far field region [72–76]. TM measures a convoluted signal arising from the wavefront distortion caused in the probed surface of the sample in addition to the phase shift created by heat-coupling in the fluid surrounding the sample. This method has been recently introduced under pulsed Gaussian laser excitation for the measurement of thermal diffusivity and thermo-optical properties of semi-transparent and opaque solids [72, 75] and for the detection of thermoelastic waves launched by a localized heat deposition [10, 77, 78]. This method has also been used to detect surface displacement induced by radiation pressure at air-liquids interfaces [74, 76].

Out-of-plane surface displacement can be detected with a homodyne quadrature laser interferometer (HQLI) [8,79,80], a special extension of an arm-compensated Michelson interferometer [8, 81]. HQLI employs the quadrature detection using a stable, linearly polarized laser. Using an additional octadic-wave plate and a polarizing beam splitter, two orthogonally polarized interference signals in phase quadrature are generated and detected by two photodiodes. These two signals provide the means to measure the displacements with a sub-nanometer resolution, high dynamic range and constant sensitivity. This method has been used to detect laser-induced, out-of-plane point displacements of high-amplitude and high-frequency [8, 82]. The HQLI also senses the phase shift induced by the thermal lens, the underlying effect used in refractometers [83].

Here, we present a combined pump-probe method to detect laser induced thermoelastic surface displacement in metals by simultaneous measurement using photothermal mirror and interferometry. A single-shot continuous wave excitation laser beam is used to induce surface displacement of the sample by heat generation following surface optical absorption. Heat propagates to the surrounding air changing its refractive index with temperature creating a thermal lens effect in the air. Both methods probe the surface displacement of the sample and the thermal lens effect in the fluid by analyzing wavefront distortions

of the probe beams reflected from the surface of the sample. The interferometer senses the out-of-plane surface displacement and the thermal lens effect at a single location on the surface, while the photothermal mirror senses the total laser induced phase shift caused on the surface of the sample and in the surrounding air. The theoretical predictions are quantitative and describe the experiments performed in metals. We demonstrate the utility of this combined technique to detect thermoelastic displacement at the nanometer-scale. The single-shot combined method has revealed important features that a single technique could not discern with the same precision, including features such as heat diffusion properties as well as mechanical perturbations.

4.2 Theory

The detection methods use two probe beams and a single excitation beam. The cw Gaussian (TEM_{00}) laser beam propagates along the z-axis and excites the sample almost perpendicular to its surface. The sample surface is located at $z = 0$. Part of the laser power is absorbed at the sample surface and converted into heat, and the rest is reflected. By conduction, heat is transferred to the surrounding air generating a thermal lens due to the temperature dependence of the refractive index of air. Due to the circular symmetric geometry of the problem, the scalar temperature and the vector displacement fields depend only on the normal z- and radial r-coordinates.

The spatiotemporal distribution of the temperature change, $T_i(r,z,t)$, is solved for the sample ($i = s$) and for the surrounding fluid ($i = f$), which obeys the heat diffusion equation [75]

$$\frac{\partial T_i(r,z,t)}{\partial t} - D_i \nabla^2 T_i(r,z,t) = \zeta Q_0 Q(r) Q(z), \tag{4.1}$$

where $\zeta = 1$ for $i = s$ and $\zeta = 0$ for $i = f$. For the Gaussian beam excitation,

$Q(r) = \exp\left(-2r^2/w_e^2\right)$ and $Q_0 = 2P_e(1-R)\phi/\pi c_s \rho_s w_e^2$. P_e is the excitation power, $D_i = k_i/\rho_i c_{pi}$ is the thermal diffusivity, k_i is the thermal conductivity, ρ_i is the mass density, c_{pi} is the specific heat, t is the time, R is the reflectivity at the excitation wavelength, and w_e is the radius of the excitation beam on the surface of the sample. ϕ accounts for the fraction of the absorbed energy converted to heat; $\phi = 1$ if the absorbed energy is totally converted to heat. The deposition of thermal energy by light absorption is assumed to occur only at the surface of the sample, which can be represented in the high absorption limit by a Dirac delta function $Q(z) = 2\delta(z)$, bringing mathematical simplicity to the model.

The temperature gradients in the fluid and in the sample can be written in terms of the inverse of Laplace and Hankel transforms as

$$T_i(r,z,t) = \int_0^\infty T_i(\alpha,z,t) J_0(\alpha r)\alpha \mathrm{d}\alpha, \tag{4.2}$$

using the convolution theorem

$$T_i(\alpha,z,t) = \frac{k_s Q_0 Q(\alpha)}{\sqrt{D_s/D_f}} \int_{t_0}^{t} G(\alpha, t-\tau) H(\alpha,\tau,D_i)\mathrm{d}\tau, \tag{4.3}$$

in which $H(\alpha,t)$ and $G(\alpha,t,D_i)$ are given by the inverse Laplace transform of $H(\alpha,s)$ and $G(\alpha,s,D_i)$, respectively, as $H(\alpha,t,D_i) = \delta(t)$, for $z = 0$, $H(\alpha,t,D_i) = |z|(4\pi t^3 D_i)^{-1/2}\exp\left[-D_i\alpha^2 t - z^2/(4D_i t)\right]$, for $z \neq 0$, and

$$\begin{aligned} G(\alpha,t) = \frac{k_s\sqrt{D_f}}{\alpha\kappa(k_s^2 D_f - k_f^2 D_s)}[\sqrt{D_s}\mathrm{Erf}(\alpha\sqrt{D_s}\sqrt{t}) \\ - e^{-\alpha^2\kappa t}\sqrt{D_s-\kappa}\mathrm{Erf}(\alpha\sqrt{D_s-\kappa}\sqrt{t})] - \\ \frac{k_f\sqrt{D_s}}{\alpha\kappa(k_s^2 D_f - k_f^2 D_s)}[\sqrt{D_f}\mathrm{Erf}(\alpha\sqrt{D_f}\sqrt{t}) \\ - e^{-\alpha^2\kappa t}\sqrt{D_f-\kappa}\mathrm{Erf}(\alpha\sqrt{D_f-\kappa}\sqrt{t})] \end{aligned} \tag{4.4}$$

Here, $\kappa = (k_s^2 - k_f^2)D_s D_f/(k_s^2 D_f - k_f^2 D_s)$, $\mathrm{Erf}(x)$ is the error function, $J_0(x)$ is the Bessel function of the first kind and the Hankel transform of $Q(r)$ is $Q(\alpha) = (w_e^2/4)\exp\left(-w_e^2\alpha^2/8\right)$. $t_0 = 0$ accounts for the laser-on ($t < \xi$) and $t_0 = t - \xi$ for the laser-off ($t > \xi$) excitation regimes. ξ is the duration of illumination. Both excitation and relaxation regimes are recorded experimentally.

The temperature field is used then, as the source to compute the thermoelastic displacement of the sample, by solving the thermoelastic equation of motion with the appropriate initial and boundary conditions. The displacement field $\mathbf{u} \equiv \vec{u}(r,z,t)$ of a homogeneous and isotropic solid is given by the solution of [75]

$$(\lambda + 2\mu)\nabla^2\mathbf{u} + (\lambda+\mu)\nabla(\nabla\cdot\mathbf{u}) = \gamma\nabla T_s(r,z,t) + \rho_s\frac{\partial^2\mathbf{u}}{\partial t^2}, \tag{4.5}$$

where $\gamma = (3\lambda + 2\mu)\alpha_T$. $\lambda = E\nu_s/[(1+\nu_s)(1-2\nu_s)]$ and $\mu = E/2(1+\nu_s)$ are the Lame's constants, E is the Young's modulus, α_T is the linear thermal expansion coefficient, and ν_s is the Poisson's ratio of the sample. The last term on the right-hand side of the thermoelastic equation represents the inertia term yielding elastic wave motion. This term can be neglected [84] as the signal oscillations due to the inertia term are not observed experimentally considering the relatively long detector response time [85]. The z-component (normal) of the displacement vector at the sample surface for a semi-infinite sample is

$$\begin{aligned} u_z(r,0,t) &= \theta_{\mathrm{TM}}\frac{\lambda_p k_s D_s\sqrt{D_f}}{\pi}\int_0^\infty\int_{t_0}^t\left[\frac{e^{-D_s\alpha^2\tau}}{\alpha\sqrt{\tau\pi}} - \sqrt{D_s}\mathrm{Erfc}(\alpha\sqrt{\tau D_s})\right] \\ &\quad G(\alpha, t-\tau)\alpha^2 e^{-w_e^2\alpha^2/8}J_0(\alpha r)\mathrm{d}\tau\mathrm{d}\alpha. \end{aligned} \tag{4.6}$$

$\theta_{\mathrm{TM}} = -P_e(1-R)(1+\nu_s)\alpha_T\phi/(k_s\lambda_p)$ [72] and λ_p is the probe beam wavelength.

The normal surface deformation given by Eq. (4.6) can be concurrently measured by the TM and the interferometer. The TM detection is performed by analyzing the on-axis intensity change of the central portion of the probe beam reflected from the sample surface at the far field photodetector [74, 84]. The

centers of both the pump and the probe beams overlap at the sample surface. The thermoelastic displacement created at the surface acts as a dynamic optical element to the wavefront of the probe beam increasing or diminishing its power passing the pinhole at the detector plane. $u_z(r,0,t)$ produces a phase shift to the reflected portion of the TM probe beam

$$\Phi^s_{\mathrm{TM}}(r,t) = \frac{4\pi}{\lambda_p} u_z(r,0,t). \tag{4.7}$$

Additional phase shift to the probe beam as a consequence of the thermal lens (TL) effect created in the surrounding air by heat coupling to the sample is given by [84]

$$\Phi^f_{\mathrm{TL}}(r,t) = \frac{4\pi}{\lambda_p}\left(\frac{dn}{dT}\right)_f \int_{-\infty}^{0} \left[T_f(r,z,t) - T_f(0,z,t)\right] \mathrm{d}z. \tag{4.8}$$

$(dn/dT)_f$ is the temperature coefficient of the fluid refractive index at λ_p. The probe beam wavefront distortion caused by the thermoelastic displacement of the sample and temperature change in the air is

$$\Phi_{\mathrm{TM}}(r,t) = \Phi^s_{\mathrm{TM}}(r,t) + \Phi^f_{\mathrm{TL}}(r,t). \tag{4.9}$$

The intensity of the reflected TM probe beam varies as [2]

$$S(t) = \left| \int_0^{\infty} \frac{2r}{w_p^2} \exp\left[-\left(1 + i\frac{z_1}{z_c}\right)\frac{r^2}{w_p^2} - i\Phi_{\mathrm{TM}}(r,t) \right] \mathrm{d}r \right|^2, \tag{4.10}$$

where z_c is the confocal distance of the probe beam, z_1 is the distance from the probe beam waist to the sample, and w_p is the radius of the probe beam at the sample surface. Eq. (4.10) can be evaluated numerically using the calculated $u_z(r,0,t)$ and $T(r,z,t)$.

The total phase shift $\Phi_{\mathrm{TM}}(r,t)$ is sensed by both the photothermal mirror and the interferometer. The interferometer gives direct access to the phase shift at a chosen off-axis distance r while the photothermal mirror shows a convoluted

signal resulting from the total phase shift at the sample surface and in the air given by Eq. (4.10). The physical parameters of the sample and fluid in $\Phi_{\mathrm{TM}}(r,t)$ can be rearranged in terms of θ_{TM}.

4.3 Experimental

The combined photothermal mirror and interferometer experiments use the pump-probe configuration schematically shown in Fig. 4.1. The cw excitation, a TEM_{00} optically pumped semiconductor laser (Coherent, Verdi G7, 532 nm), was used to pump the samples. The excitation laser is arranged almost collinear to both probe laser beams. The angles between each beam and the normal to the surface of the sample is always $< 1^{\circ}$. The exposure time of the sample to the excitation laser beam (laser-on and laser-off) is controlled by a mechanical shutter (SRS, Model SR470) with an oppening/closing time of about $6\ \mu s$. TM detection uses a He-Ne laser at $632.8\ \mathrm{nm}$ (Thorlabs, Model HNL225R-JP, 22.5 mW). The intensity variation of the probe beam center after reflection was detected by a pinhole-laser line filter-photodetector assembly PD(TM)(Thorlabs, Model PDA36A2) in the far field. A digital oscilloscope (Tektronix, Model DPO 4102B) triggered by the photodiode PD(Trigger) (Thorlabs, Model PDA36A2) recorded the data. The measured decreasing/increasing intensity signal corresponds to the laser induced convex/concave optical element.

The interferometer uses a stabilized He-Ne laser at $632.8\ \mathrm{nm}$ (Thorlabs, Model HRS015B, 1.2 mW). The linearly polarized beam exiting the laser lies in the plane of the optical table (x–z plane). After the optical Faraday isolator (OFI), the beam polarization forms a 45° angle with respect to the x-axis. This polarization can be decomposed into two orthogonal polarizations with equal intensities, one in the plane of the paper (x-axis) and the other perpendicular to it (y-axis). The 50%–50% nonpolarizing cube beam splitter (NBS) evenly divides the beam into the reference and the measurement arm. The first transition through the $\lambda/8$,

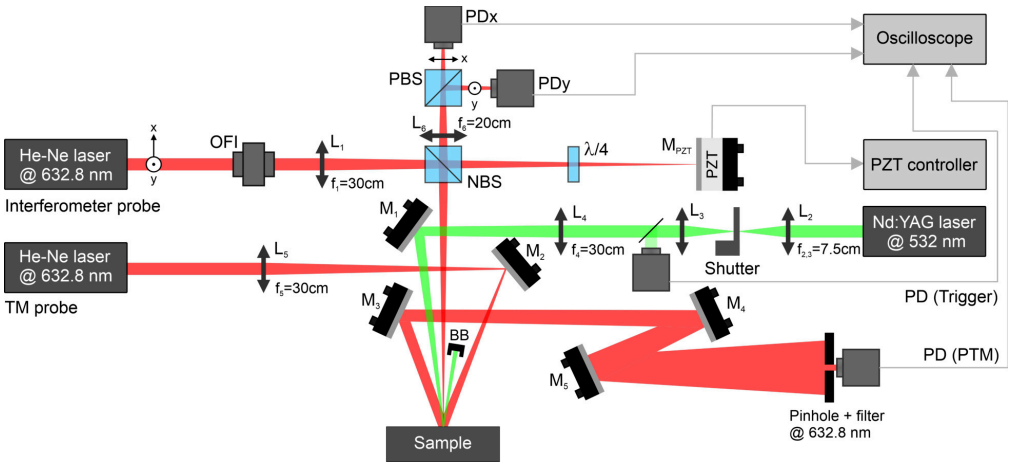

Figure 4.1: Experimental diagram for the TM and the interferometer measurements. The pump and the probe beams are focused by the biconvex lenses L_j of focal lengths f_j. M_j, BB, BS and PD_j stand for the lenses, the beam blocker, the beam sampler and the photodiodes. NBS/PBS are the nonpolarizing/polarizing beam splitters, OFI is the optical Faraday isolator, $\lambda/8$ is the octadic wave plate and PDx,y detects the beam having x,y-polarization. The laser beams have radii: $w_e = 646$ µm, $w_p = 1584$ µm, $w_{\text{interf.}} = 154$ µm, at the surface of the sample. The experimental parameters are $z_c = 0.50$ cm, and $z_1 = 26.1$ cm. The temperature of the samples was 298 K.

which is placed in the reference arm, gives rise to the 45° phase difference between the orthogonal polarizations. The beam is then reflected from the reference mirror (M_{PZT}), which is driven by a piezoelectric transducer (PZT), and an additional 45° is added on the returning passage through the $\lambda/8$. The orthogonal polarizations in the measurement arm undergo an equal phase shift due to the displacement of the sample surface and the thermal lens generated in the surrounding air. The polarizing beam splitter (PBS) transmits the x-polarization and reflects the y-polarization. The two beams with polarizations in the x-z/y-z plane, one from the reference arm and the other from the measurement arm, reach the Si photodiode PDx/PDy. The two photodiodes are equal and have equal amplification gains. Furthermore, the arms are of equal length so that the interfering beams have the same wavefront curvature. Ideally, the interference signals on the photodiodes are shifted by 90°, which can be achieved with a properly rotated $\lambda/8$. The measured time dependent phase shift due to the surface displacement and thermal lens in the air are encoded in the phase $\Phi_{\text{TM}}(r,t)$.

The interferometer probes the phase at a position r by placing a lens just before the NBS to focus the probe beam, reducing the probing area, with radius $w_{\text{interf.}} = 154\ \mu\text{m}$, at the surface of the sample. The phase shift is derived from the intensities I_{x} and I_{y} from the photodetectors PDx and PDy, respectively, and is given in terms of the DC offset I_0 as

$$\Phi_{\text{TM}}^{\text{int.}}(r,t) = \arctan\left[\frac{I_y(t) - I_0/4}{I_x(t) - I_0/4}\right] + m\pi,\ m = 0, \pm 1, \ldots \tag{4.11}$$

The integer m must be chosen correctly, so that the function $\Phi_{\text{TM}}^{\text{int.}}(r,t)$ satisfies the condition of being continuous. As described in details in Refs. [86, 87], the PZT was used to make a synthetic displacement of more than $\lambda_p/2$ in order to obtain the parameters of a full ellipse, which are used in the unwrapping process.

4.4 Results and Discussion

Experiments were performed in copper, bronze and inox cylinders having diameter of $50\ \text{mm}$ and height of $15\ \text{mm}$. The samples were polished to obtain a mirrored surface and irradiated by a focused laser beam. The results are presented in Fig. 4.2. The phase shift obtained from the interferometric measurements at $r = 0$, $\Phi_{\text{TM}}(0,t)$, are recovered from the unwrapping of the time-dependent signals from the photodiodes PDx and PDy – Fig. 4.2(a). Fig. 4.2(b) show the normalized intensity signal of the central portion of the TM probe beam, $S(t)/S(0)$. The signals are averaged over 100 transients and the time interval between consecutive events is long enough for the sample to return to its unperturbed state.

The surface deformation produced by the excitation laser acts as a convex mirror to the TM probe beam [88], decreasing the TM intensity signal at the photodetector at first, and then recovering it as the heat diffuses out of the irradiated region of the sample, reaching a steady state. The laser-off transients show the

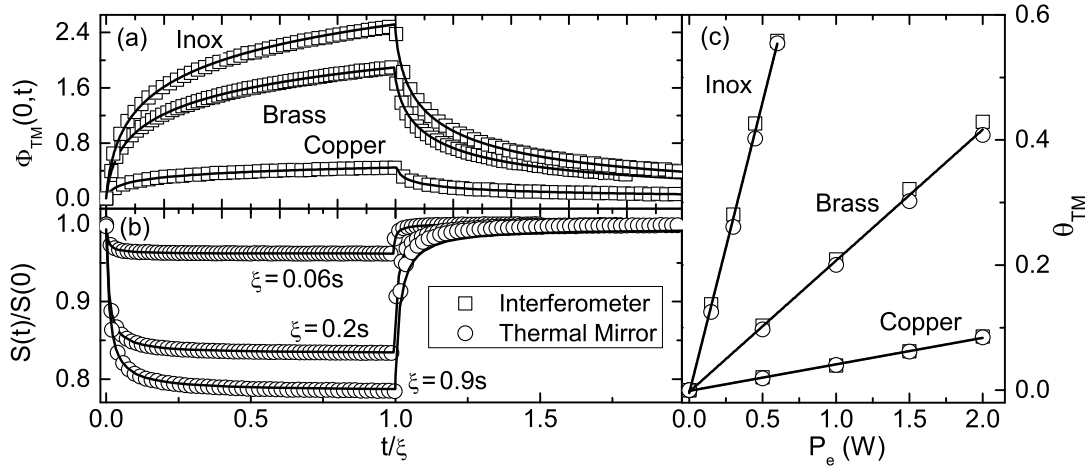

Figure 4.2: Measured (open circles and squares) (a) interferometric and (b) TM signals for copper, bronze and inox as a function of the reduced time, t/ξ. Continuous lines represent the numerical fit of the experimental curves to $\Phi_{\rm TM}(0,t)$ (interferometer) and Eq. (4.10) (TM). (c) shows the retrieved $\theta_{\rm TM}$ as a function of the excitation power.

relaxation processes with the signal reaching the original values at $t = 0$. The interferometric transients, on the other hand, do not approach steady state for the excitation time used in this work as the phase shift continues to increase with time. The thermal diffusivity of the samples dictates how fast heat diffuses within the sample and out to the fluid, and the amplitude of the transients are related to the excitation power, thermal conductivities and thermal expansion coefficient of the sample.

The continuous lines in Fig. 4.2(a) and (b) are the numerical fit of the experimental curves to $\Phi_{\rm TM}(0,t)$ (interferometer) and $S(t)/S(0)$ (TM). Regression was performed by numerically evaluating these equations in a C++ compiled software. The numerical fits are in good agreement with the measurements. The parameter $\theta_{\rm TM}$ recovered from both the interferometer and the TM measurements shows a linear dependence on the excitation power as displayed in Fig. 4.2(c). The linear regression gives $\theta_{\rm TM}/P_e$, which depends on the thermal conductivity of the sample. By using literature values for α_T and ν_s, and the measured reflectivity R, the results for k_s and $\rho_s c_{ps}$ are presented in Table I. These results are in complete agreement with the literature values for the thermal and mechanical properties

Table 4.1: Physical properties of the metals. The literature values are for metals with characteristics similar to the samples investigated here. Reflectivity R is 0.58 for copper, 0.69 for bronze, and 0.60 for inox, and $(dn/dT)_{air} = -1 \times 10^{-6}\mathrm{K}^{-1}$ [72].

Material	D_i (10^{-6}) $\mathrm{m^2s^{-1}}$		θ_{TM}/P_e $\mathrm{W^{-1}}$	k_i $\mathrm{Wm^{-1}K^{-1}}$		$\rho_s c_{ps}$ (10^6) $\mathrm{Jm^{-3}K^{-1}}$	ν_s	α_T (10^{-6}) $\mathrm{K^{-1}}$
	This work	Ref. [89]	This work	This work	Ref. [89]	This work	Ref. [89]	Ref. [89]
Copper	105 ± 6	113	0.042 ± 0.001	355 ± 15	391	3.4 ± 0.2	0.31	17.3
Bronze	19 ± 2	17.6	0.210 ± 0.005	55 ± 3	59	2.9 ± 0.1	0.32	18.0
Inox	3.6 ± 0.1	4.0	0.93 ± 0.02	15.2 ± 0.7	16.2	4.2 ± 0.2	0.29	17.3
Air	21.9		0.026					

of the samples [89].

Even though TM and interferometer both measure the temporal dependence of the power of the probing light reaching the sensor, TM is more sensitive to the shape of the probed surface, while the two HQLI signals depend primarily on the phase shift induced by the displacement of the investigated surface. When both methods are compared, TM is appropriated for on-field measurements due to its practically insensitivity to mechanical vibrations and absolute surface displacement in the z-direction. On the other hand, the signal of the interferometer is easier to be fitted and is, assuming negligible contribution of the lens effect of the heated air, directly proportional to the z-component of the displacement and thus easily interpretable. The unprecedented collective experimental power of using both methods at the same time not only cross validates each other, but also gives access to additional insights of the underlying physics, especially when the interferometer is used in the surface-scanning mode.

The combined interferometer/TM method presented here has applications for the characterization of opaque and semitransparent materials. These methods are highly sensitive, non-contacting techniques. This makes them a useful tool to investigate materials in a variety of environmental conditions by controlling temperature, pressure and even applying external electric and magnetic fields. Both methods are complementary in a sense that the interferometer is sensitive to the out-of-plane surface displacement of the sample at a single location, while the photothermal mirror reads a complex convolution of all the effects taking place in

the sample surface and in the coupling fluid. TM has been proven to characterize laser induced thermoelastic waves generated locally and propagating within metals, thermo-optical and mechanical properties of semiconductors and semi-transparent materials, and even in detecting the effects of radiation pressure in dielectric liquids. The combination of the two techniques brings substantial improvements for single shot analysis and offer compelling support to describe the origins of light and mater interaction effects.

4.5 Conclusions

In summary, we proposed a combined photothermal mirror and interferometric detection method using simultaneous laser induced surface displacement to investigate thermal, optical and mechanical properties of metals. Both the wavefront distortion caused by the surface displacement of the sample and the thermal lens in coupling fluid are sensed by the probe beams from the two techniques. The combined technique gives direct access to the phase shift at a single location on the surface of the sample (interferometer) in addition to the convoluted signal arising from the total wavefront distortion in the media (photothermal mirror). Both methods are complementary in a sense that the interferometer is sensitive to the out-of-plane surface displacement of the sample at a single location, while the photothermal mirror reads a complex convolution of all the effects taking place on the sample surface and in the coupling fluid. The photothermal mirror has been proven to characterize laser induced thermoelastic waves generated locally and propagating within metals, thermo-optical and mechanical properties of semiconductors and semi-transparent materials, and even in detecting the effects of radiation pressure in dielectric liquids. The combination of the two techniques brings substantial improvements for single-shot analysis and offer compelling support to describe the origins of light and mater interaction effects.

Part III

Edge effects induced inaccuracy

CHAPTER 5

INFLUENCE OF EDGE EFFECTS ON SURFACE DISPLACEMENT

5.1 Introduction

The dynamic events following light absorption at the surface of the inspected material contain information on the structure of matter, its geometry and its physical and thermoelastic properties. The temperature changes resulting from optical absorption are responsible for generating thermoelastic disturbances detectable at the surfaces of the sample, bringing characteristic signatures of defects and shape of the system that can be exploited experimentally in several different ways. External and internal boundaries are accessible in such a system, for example, by monitoring the perturbations caused by heat diffusion at the interfaces [1] or by elastic waves reverberating within the material [10].

In practice, the inspected materials have to be prepared as samples of well-defined finite dimensions, often as small as possible, especially when the material is expensive or difficult to be produced. This in turn imposes some limitations on how to model the response of such samples and compare the model

to the measurements to retrieve the unknown sample properties. The lateral heat flow confinement or the elastic waves reflections from the samples surfaces are known as edge effects. They become important when the heat diffusion flow is laterally halted or when the disturbances reflect from the edges and return to the detection site. The edge effects are responsible for the scattering of elastic waves propagating inside materials and form the basis of photothermal ultrasound detection systems with applications ranging from biological imaging [90, 91] to defect inspection [92, 93]. Edge effects also have an important role in material processing procedures [94–96]. Several methods including laser interferometry have been used for investigating surface properties [97, 98], local magnetic property deterioration in metals [99], micro-damage evolution [100], fatigue failure [101], mechanical properties [4, 102], and as optical image hiding method [103, 104]. This technique reveals how nanostructured surfaces and structures can be characterized, such as textured stainless steel [105], Mylar polymer films [106] and biomaterials, for instance, polymerized hexamethyldisiloxane [107] and hydroxyapatite materials [108, 109]. Interferometric methods are also used in all-optical ultrasound detection [110], which can overcome some limitations when compared with piezoelectric transducers detection in biological imaging [111, 112].

In many photothermal interferometric methodologies, simplified heat transfer treatments are feasible in applications where the diameter of the sample is much larger than its thickness. This approximation minimizes the edge effects and the system can be modeled properly using (semi)analytically-solvable, one-dimensional formulations. On the other hand, finite systems are complex and require three-dimensional numerical description of the heat propagation and the corresponding thermoelastic deformation. Here we report on the edge effects occurring under laser-induced surface displacements of metals measured by optical interferometry. The interferometer used in this study, the homodyne quadrature laser interferometer (HQLI), has a wide dynamic range and a constant sen-

sitivity [8]. It is traceable to the primary standard of length [113] and is thus very accurate in measuring physical displacement of reflective objects as well as changes in the refractive index of transparent gases. This detector is thus both, a displacement measuring device [114] and a refractometer [83], exactly what is needed to simultaneously probe the surface bending of a heated reflective solid and the temperature rise in the gas above the heated sample, since both information can be encoded into the optical phase difference (OPD). The HQLI has already been used to detect very fast transients (temporal resolution of about 10 ns) [86], where elastic waves play an important role, and also slow phenomena, such as the creeping of polymers (total measuring time of minutes) [9] and determination of the absolute gravity [115]. This makes the HQLI a complementary technique to the thermal mirror (TM) and thermal lens (TL) inspection of materials with a notable difference [116]. The HQLI is sensitive to the absolute displacements and absolute changes of the refractive index encoded in the OPD, while the TM/TL techniques sense the relative changes, encoded as the wave front distortion of the optical probe beam. The notable advantage of using the HQLI is the capability of probing point-displacements [85], while the TM/TL proved to be independent of the environmental vibrations making this detection method more robust [116].

In this study, the HQLI is used to detect the laser-induced thermoelastic surface displacement in metals under on/off continuous laser excitation. Heat generated by light absorption on the surface of the sample builds up and dissipates within the material and out to the coupling air. The finite geometry of the samples is crucial in determining how the temperature is distributed across the material and how this affects the interferometer phase shift measurements. The optical path change due to the surface thermoelastic deformation and the TL in the surrounding air is decoded from the interferometric signal using semi-analytical and numerical tools. The boundary/edge effects are found to be relevant to properly describe the interferometric signals. The tools developed in this study are appli-

cable to describe not only the phase shift sensed by the interferometer but also to contribute to the photothermal-based technologies employing similar detection mechanisms.

5.2 Theory

Two theoretical approaches were used to model the response of the specimen and the surrounding air to laser heating of the sample surface. The first approach gives a neat analytical solution, often accurate enough to give useful results, especially when the laser beam diameter is small compared to the dimensions of the sample and when the heat diffusion has not yet been affected by the sample boundaries. The second one is a more realistic numerical procedure based on the finite elements analysis (FEA).

In both models, cylindrical symmetry is considered, defined by the coordinates (r,z,φ,t), where r is the axial distance from the z-axis, φ is the azimuth, a problem independent variable, and t is the time. Three fields of interest are calculated: the scalar temperature rise field in the fluid $T_f(r,z,t)$ and in the solid sample $T_s(r,z,t)$ and the vector displacement field of the sample $\mathbf{u} \equiv \vec{u}(r,z,t)$. These fields are then used to calculate the optical phase difference (OPD) $\Phi(r,t)$, measurable by an appropriate interferometer.

The main difference between the two models is the geometry of the problem. The analytical approach assumes two homogeneous and isotropic half-spaces, a light absorbing solid sample ($z > 0$) in contact at $z = 0$ with a non-absorbing fluid ($z < 0$). The FEA model is more realistic, because it additionally takes into account the exact geometry of the sample (a homogeneous and isotropic cylinder with a finite radius and a finite height) as shown in Fig. 5.1, including the sample mount. Physically, the key novelty introduced by taking the finite lateral dimension of the sample into account is the lateral boundary that prohibits an effective lateral diffusion of heat within the sample.

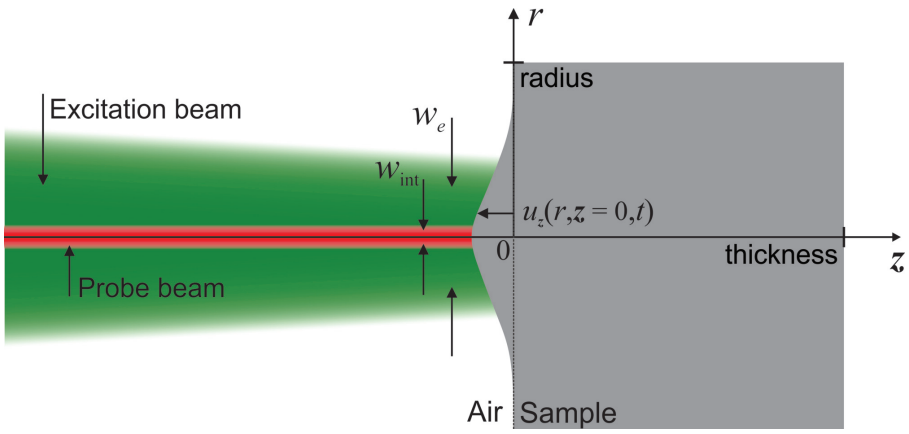

Figure 5.1: Geometric scheme of the beams in the measurement arm of the interferometer.

The surface of the sample is illuminated through the fluid using a temporally modulated (on-off boxcar-modulated continuous wave (cw) with the exposure time ξ) Gaussian (TEM_{00}) laser beam coinciding with the z-axis and having a radius of w_e at the surface of the sample, as shown in Fig. 5.1. Assuming a temperature independent reflectivity at the excitation laser wavelength R, the surface reflects a fraction PR of the laser power P and absorbs $P(1-R)$. The absorbed light is converted into heat, which is then diffused into the sample and the neighboring fluid (air). As a consequence of thermal expansion, the surface is deformed according to the temperature profile in the sample. Additionally, a thermal lens is induced above the solid sample – the refractive index of the air is temperature dependent. A simultaneous detection of both, the out-of-plane surface displacement and the TL of the air was performed by a HQLI.

5.2.1 Analytical approach

5.2.1.1 Temperature fields

The spatiotemporal distribution of the temperature (rise) is sought for the sample and fluid. It is given by the solution of the coupled heat diffusion equations [117]

$$\frac{\partial T_i(r,z,t)}{\partial t} - D_i \nabla^2 T_i(r,z,t) = Q_i Q(r) Q(z), \tag{5.1}$$

with proper boundary and initial conditions as given in Ref. 84. $D_i = k_i/\rho_i c_{pi}$ is the thermal diffusivity, k_i is the thermal conductivity, ρ_i is the mass density and c_{pi} is the specific heat for the sample ($i = s$) and fluid ($i = f$). The heat source in the sample is $Q_s = 2P(1-R)\phi/\pi c_s \rho_s w_e^2$ and $Q(r) = \exp\left(-2r^2/w_e^2\right)$. Since the fluid is assumed not to absorb any laser light, $Q_f = 0$. The portion of the absorbed power converted into heat is represented by ϕ, which in this case is 1 as the absorbed power is completely converted into heat. For opaque, highly-absorbing materials, the excitation light is assumed to be absorbed only by the surface, thus one can adopt the Dirac delta function $Q(z) = 2\delta(z)$.

The temperature gradients in the fluid and in the sample can be written in terms of the inverse of Laplace and Hankel transforms as

$$T_i(r,z,t) = \int_0^\infty T_i(\alpha,z,t)\mathrm{J}_0(\alpha r)\alpha \mathrm{d}\alpha, \tag{5.2}$$

where $\mathrm{J}_0(x)$ is the Bessel function of the first kind, and

$$T_i(\alpha,z,t) = \frac{k_s Q_0 Q(\alpha)}{\sqrt{D_s/D_f}} \int_{t_0}^{t} G(\alpha,t-\tau)H(\alpha,\tau,D_i)\mathrm{d}\tau, \tag{5.3}$$

in which $G(\alpha,t)$ and $H(\alpha,t,D_i)$ are given by the inverse Laplace transform of $G(\alpha,s)$ and $H(\alpha,s,D_i)$, respectively, as

$$H(\alpha,t,D_i) = \begin{cases} \delta(t) & , z = 0 \\ \dfrac{|z|\exp\left[-D_i\alpha^2 t - z^2/(4D_i t)\right]}{\sqrt{4\pi t^3 D_i}} & , z \neq 0 \end{cases}, \tag{5.4}$$

and

$$G(\alpha,t) = \frac{k_s\sqrt{D_f}}{\alpha\kappa(k_s^2D_f - k_f^2D_s)}[\sqrt{D_s}\mathrm{Erf}(\alpha\sqrt{D_s}\sqrt{t}) - e^{-\alpha^2\kappa t}\sqrt{D_s-\kappa}\mathrm{Erf}(\alpha\sqrt{D_s-\kappa}\sqrt{t})] - \frac{k_f\sqrt{D_s}}{\alpha\kappa(k_s^2D_f - k_f^2D_s)}[\sqrt{D_f}\mathrm{Erf}(\alpha\sqrt{D_f}\sqrt{t}) - e^{-\alpha^2\kappa t}\sqrt{D_f-\kappa}\mathrm{Erf}(\alpha\sqrt{D_f-\kappa}\sqrt{t})] \quad (5.5)$$

Here, $\kappa = (k_s^2 - k_f^2)D_sD_f/(k_s^2D_f - k_f^2D_s)$, $\mathrm{Erf}(x)$ is the error function, and $Q(\alpha) = (w_e^2/4)\exp\left(-w_e^2\alpha^2/8\right)$ is the Hankel transform of $Q(r)$. $t_0 = 0$ accounts for the laser-on ($0 < t < \xi$) and $t_0 = t - \xi$ for the laser-off ($t > \xi$) excitation regimes. Both the excitation and the relaxation regimes are recorded experimentally. Using the null heat-flux approximation, $k_f \ll k_s$, the temperature change, on the surface at $z = 0$, is reduced to

$$T_s(\alpha,0,t) = \frac{Q_0Q(\alpha)}{D_s\alpha}\mathrm{Erf}\left[\alpha\sqrt{D_st)}\right]. \quad (5.6)$$

5.2.1.2 Displacement field

The temperature distribution within the solid is used as the source to compute the thermoelastic displacement of the sample by solving the thermoelastic equation of motion. The displacement field **u** is given by the solution of [118]

$$(\lambda+2\mu)\nabla^2\mathbf{u} + (\lambda+\mu)\nabla(\nabla\cdot\mathbf{u}) = \gamma\nabla T_s(r,z,t) + \rho_s\frac{\partial^2\mathbf{u}}{\partial t^2}, \quad (5.7)$$

with free surface boundary conditions of the normal stress components in the semi-infinite plane, $\sigma_{rz}|_{z=0}$ and $\sigma_{zz}|_{z=0}$. Here, $\lambda = E\nu/[(1+\nu)(1-2\nu)]$ and $\mu = E/2(1+\nu)$ are the Lame's constants, $\gamma = (3\lambda+2\mu)\alpha_T$, E is the Young's modulus, α_T is the linear thermal expansion coefficient, and ν is the Poisson's ratio of the sample. The last term on the right-hand side of Eq. (5.7) represents the inertia

term yielding elastic wave motion. This term can be neglected [84] as the elastic waves described by the inertia term are not observed experimentally since the detector averages them out due to its relatively long response time [85]. The normal component of the displacement vector at the sample surface, $u_z(r, z = 0, t)$, in null flux approximation, can be written for the semi-infinite sample as

$$u_z(r,0,t) = -2(1+\nu)\alpha_T \int_0^\infty \alpha^2 f(\alpha,t) J_0(\alpha r) \mathrm{d}\alpha, \tag{5.8}$$

where

$$f(\alpha,t) = Q_0 Q(\alpha) \int_{t_0}^{t} \frac{1}{\alpha} \mathrm{Erfc}\left(\alpha\sqrt{D_s\tau}\right) \mathrm{d}\tau. \tag{5.9}$$

For $r = 0$, Eq. (5.8) reduces to

$$u_z(0,0,t) \quad = \quad \theta \frac{\lambda_p}{2\pi} \frac{2}{t_c} \int_{t_0}^{t} \left(1 - \frac{1}{\sqrt{1+t_c/2\tau}}\right) \mathrm{d}\tau, \tag{5.10}$$

where $t_c = w^2/4D_s$, $\theta = -P(1-R)(1+\nu)\alpha_T\phi/(k_s\lambda_p)$ and λ_p is the wavelength of the probe beam. The effect of neglecting the heat-coupling in the determination of the surface displacement is discussed in Ref. 84.

5.3 Finite element analysis (FEA)

The heat transfer and thermoelastic equations, Eqs. (5.1) and (5.7), were also solved using FEA with Comsol Multiphysics 4.2a software, which provides numerical solutions to the differential equations with the realistic boundary conditions imposed by the experiments. The temperature and the displacement obtained with FEA are compared with the analytical solutions, Eqs. (5.2) and (5.8). We assumed that the mechanical and thermal properties of the sample do not change much as the temperature rise induced by the excitation laser is not large.

5.4 Optical phase difference (OPD)

The surface deformation of the sample and the change of the refractive index of the air $n_f(r,z,t)$ surrounding the sample due to heat coupling can be simultaneously measured by the interferometer. This information is encoded in the OPD generated between the two arms of the interferometer. The combined OPD is

$$\Phi(r,t) = \Phi_s(r,t) + \Phi_f(r,t). \tag{5.11}$$

The first contribution

$$\Phi_s(r,t) = \frac{4\pi}{\lambda_p} u_z(r,0,t) \tag{5.12}$$

is the OPD induced by the normal thermoelastic deformation of the sample surface given by Eq. (5.8). The second contribution

$$\Phi_f(r,t) = \frac{4\pi}{\lambda_p}\frac{dn_f}{dT}\int_{-\infty}^{0} T_f(r,z,t)\mathrm{d}z \tag{5.13}$$

is an additional OPD the interferometer senses as a consequence of the heating of the surrounding air [116], where $T_f(r,z,t)$ is given by Eqs. (5.2) and (5.3). Here, the temperature coefficient of the fluid refractive index at λ_p, dn_f/dT, is assumed temperature independent. Since dn_f/dT for the air at normal conditions is negative, heating the air lowers its refractive index. The probing beam therefore propagates faster through the heated air which effectively shortens the time needed for the probing beam to return back and interfere with the reference beam. The same happens when the sample surface moves towards the incoming probing beam. Thus, the OPD induced due to air heating in front of the sample adds to the OPD created by the bulge due to thermal expansion.

The interferometer gives direct access to the time-varying OPD, also called phase shift, at a selected off-axis distance r. The physical parameters of the sample and the fluid in $\Phi(r,t)$ can be rearranged in terms of θ.

5.5 Experimental

5.5.1 Samples

Metals of different geometries were used to compare the numerical predictions with the interferometric experiments. Commercial grade (purity of 99%) copper (C10100) and inox (310S) metals were prepared in cylindrical shapes with one flat surface polished with polycrystalline diamond compound in order to create a high reflective surface. Copper samples were 50.8 mm and 12.7 mm in diameter and 30 mm thick. Inox samples were 50.8 mm and 12.7 mm in diameter and 15 mm thick. The optical reflection coefficients R of the samples were determined by measuring the incident and reflected power at the excitation wavelength and used to correct the absorbed power by the samples.

5.5.2 Excitation

The experimental setup is illustrated in Fig. 5.2. The samples were excited by a cw Gaussian TEM_{00} laser beam (Coherent, Verdi G7, OPSL at 532 nm) arranged practically colinear to the measurement arm of the interferometer, so that the angle between the excitation and the probe beams was $< 1^{\circ}$. The mechanical shutter (SRS, Model SR470) was placed at the focus of the lens L_2 and used to control the excitation exposure time (ξ), i.e., the laser on/off transients. The rise/fall time was approximately $7\ \mu\mathrm{s}$. The lens L_3 was placed to recollimate the beam. A small amount of the excitation light was then extracted by the beam sampler (BS) and sent to the photodiode PD (Trigger) (Thorlabs, Model DET10A/M) to trigger the digital oscilloscope (Tektronix, Model DPO 4102B) which recorded the data. The lens L_4 was used to focus the excitation beam at the sample surface with a radius $w_{\mathrm{e}} = 646\ \mu\mathrm{m}$. The laser beams radii at the sample surface position were measured with a beam profiler (Thorlabs, Model BP104-UV).

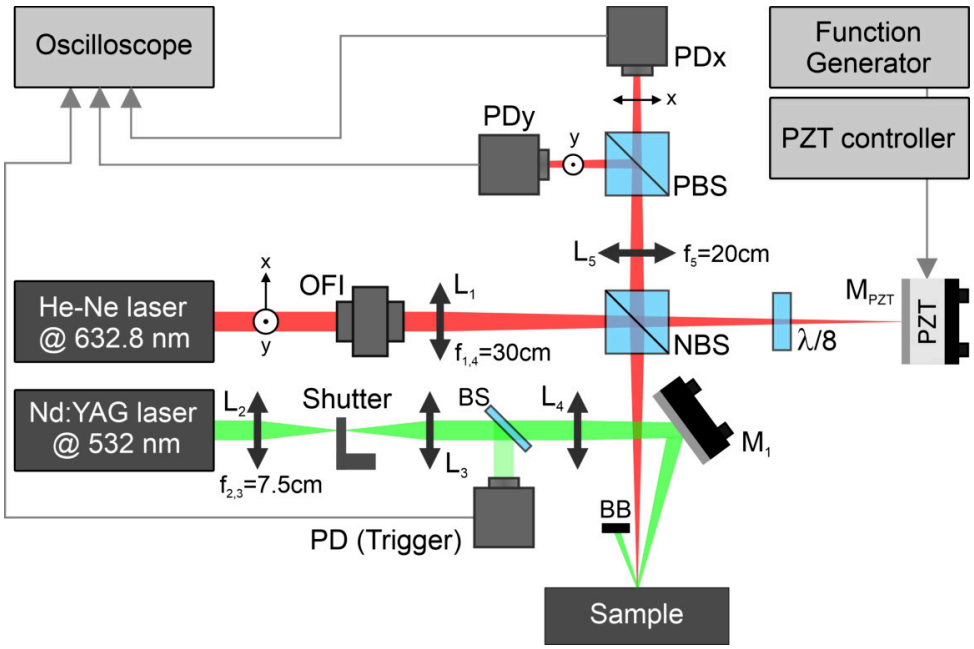

Figure 5.2: Schematic illustration of the HQLI interferometer. The system is probed by a stabilized and linear polarized He-Ne laser at 632.8 nm with polarization perpendicular to the table, with polarization rotated by 45° by the optical Faraday isolator (OFI). L_j are the biconvex lenses of focal lengths f_j, M_j are the mirrors, BB is the beam blocker, BS is the beam sampler, NBS/PBS are the nonpolarizing/polarizing beam splitters, $\lambda/8$ is the octadic wave plate and PDx,y are the photodiodes that detect the x,y-polarization of the laser, whose signals are acquired by the digital oscilloscope. The reference mirror (M_{PZT}) is attached to the piezoelectric transducer (PZT) controlled by the function generator. The thermoelastic displacement is induced in the sample by the continuous wave Gaussian beam in the fundamental mode TEM_{00} by an optically pumped semiconductor laser. The radii of the excitation and probe beams at the surface of the sample are: $w_e = 646\ \mu m$ and $w_{int} = 154\ \mu m$, respectively.

5.5.3 Detection

The HQLI was employed to monitor the magnitude of the thermal expansion and the effect of TL above the sample due to laser excitation. It uses a stabilized and linear polarized He-Ne laser at 632.8 nm (Thorlabs, Model HRS015B, 1.2 mW), with beam polarization perpendicular to the optical table. The optical Faraday isolator (OFI) rotates the polarization by 45° and blocks any back reflections, preventing the laser to destabilize. The lens L_1 focuses the beam at the sample surface with a radius $w_{int} = 154\ \mu m$. The non-polarizing beam splitter (NBS) splits the beam into the interferometer's measurement (reflected) and

reference (transmitted) arms, evenly.

The beam in the reference arm is shifted by 90° as it passes twice through the octadic-wave plate ($\lambda/8$), due to reflection from the reference mirror (M_{PZT}), which can be displaced by the attached piezoelectric transducer (PZT) controlled by the function generator (Tektronix, Model AFG1022). The beam in the measurement arm is reflected and experiences a phase shift due to (i) the displacement of the sample surface due to laser induced thermal expansion and (ii) the TL generated in the surrounding air. The two beams recombine and travel toward the polarizing beam splitter (PBS). In order to maintain the same wavefront curvature at the superposition of the two beams, the arms have to be of equal length, 20 cm in the present study. The orthogonal projection in the x direction (y direction) is transmitted (reflected) and reaches the Si photodiode PDx (PDy). The two photodiodes are identical (Thorlabs, Model PDA36A-EC) and their raw output signals are acquired by the digital oscilloscope. As the beams recombine while diverging, the lens L_5 was placed to ensure the photodiodes collect all the light.

5.5.4 HQLI signal conditioning

Consider ideal optical components, identical photodiodes with a linear response and the two ideal voltage signals x_i and y_i of the HQLI in perfect quadrature, i.e., with a relative phase shift of 90° between the photodiode signals. In this case, the two ideal signals are given by [86]

$$x_i(t) = \frac{A_0}{4}(1+\sin\Phi(t)), \tag{5.14a}$$

$$\begin{aligned} y_i(t) &= \frac{A_0}{4}[1+\sin(\Phi(t)+\pi/2)] \\ &= \frac{A_0}{4}(1+\cos\Phi(t)), \end{aligned} \tag{5.14b}$$

where A_0 stands for the voltage output if all laser light is collected by one photodiode. The optical phase difference (OPD) $\Phi(t)$, also simply dubbed the phase shift, given theoretically in Eq. (5.11), is the sum of the OPD caused by the out-of-plane thermal expansion (Eq. (5.12)) and the OPD induced by the TL (Eq. (5.13)). Solving Eqs. (5.14), the phase shift is

$$\Phi(t) = \arctan\left(\frac{x_i(t) - A_0/4}{y_i(t) - A_0/4}\right) + m\pi, \tag{5.15}$$

where $m = 0, \pm 1, \pm 2, ...$ must be chosen with a proper unwrapping algorithm to ensure the correction of the discontinuities of the arc-tangent function. By removing the DC offsets and equalizing the AC amplitudes to A, Eqs. (5.14) can be rewritten as

$$x_{in}(t) = A\sin\Phi(t), \tag{5.16a}$$

$$y_{in}(t) = A\cos\Phi(t). \tag{5.16b}$$

Note the Lissajous curves of Eqs. (5.14) and (5.16) represent a perfect circle. The OPD is accessed by

$$\Phi(t) = \arctan\left(\frac{x_{in}}{y_{in}}\right) + m\pi. \tag{5.17}$$

In the real experimental circumstances, the signals present nonlinearities despite of meticulous alignment. In this case, the raw signals assume the following form

$$x(t) = x_0 + A_x\sin\left(\Phi(t) + \Phi_0\right), \tag{5.18a}$$

$$y(t) = y_0 + A_y\cos\Phi(t). \tag{5.18b}$$

The DC offsets x_0 and y_0, AC amplitudes A_x and A_y, and the quadrature error Φ_0 are known as common nonlinearities [8]. The respective Lissajous curve is

elliptically shaped as a result of different AC amplitudes, $A_x \neq A_y$, and the lack of quadrature, $\Phi_0 \neq 0$.

The phase shift – Eq. (5.17) – when calculated directly from Eqs. (5.18), presents second order periodic errors [8]. The corrected phase, free of nonlinearities, is obtained by rearranging Eqs. (5.18) in the form of Eqs. (5.16), yielding

$$\begin{aligned} x_c(t) &= x_r(t)\,(\cos\Phi_0)^{-1} - y_r(t)\tan\Phi_0 \qquad (5.19a) \\ &= \sin\Phi(t), \\ y_c(t) &= y_r(t) = \cos\Phi(t), \qquad (5.19b) \end{aligned}$$

where $x_r(t)$ and $y_r(t)$ are the reduced components given by the signals subtracted by the DC offsets and normalized by the AC amplitudes

$$\begin{aligned} x_r(t) &= \frac{x(t) - x_0}{A_x}, \qquad (5.20a) \\ y_r(t) &= \frac{y(t) - y_0}{A_y}, \qquad (5.20b) \end{aligned}$$

respectively. Provided the nonlinearities are known, Eqs. (5.19) leads, therefore, to the corrected phase

$$\Phi(t) = \arctan\left(\frac{x_r(t)}{y_r(t)\cos\Phi_0} - \tan\Phi_0\right) + m\pi. \qquad (5.21)$$

There are a few signal processing methods which allow for the determination of the 5 unknowns (x_0, y_0, A_x, A_y, Φ_0). Fitting an ellipse to the Lissajous curve is especially efficient, more so when the total displacement does not give a full ellipse [87]. For convenience, in this paper, we made a synthetic displacement by vibrating the PZT in the reference arm of the HQLI to reach the maximum and minimum values of the interferometric signals before the measurements were performed. The latter approach was employed given it is less computationally

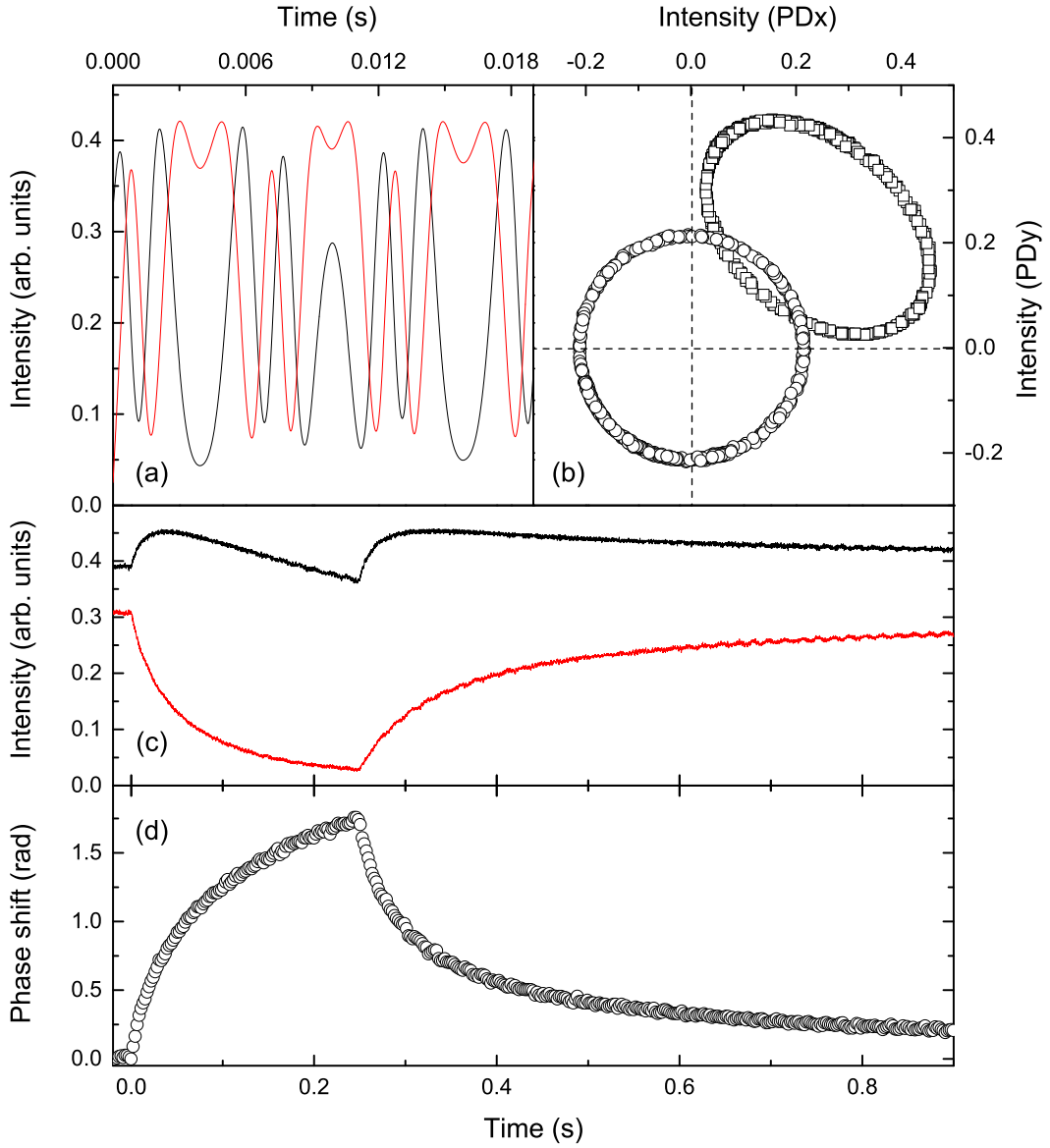

Figure 5.3: Signal processing steps. (a) Synthetic interference signals produced by the piezoelectric transducer for determination of the common nonlinearities. (b) Lissajous curves from (a) corresponding to the raw (ellipse) and corrected (circle) signals. (c) Raw interference signals obtained from the laser-induced thermoelastic displacement and TL. Black/red line is the x/y polarization signal detected by PDx/PDy. (d) Unwrapped phase transient of the signals from (c).

consuming when dealing with large amounts of transients. Interference signals of a synthetic displacement are shown in Fig. 5.3 (a) and the Lissajous curve of the raw and corrected signals is shown in Fig. 5.3 (b). Note how the ellipse has converted into a circle. Once the signal extremes are reached, the DC offsets

and AC amplitudes can be extracted from the raw signals simply as

$$(x_0, y_0) = \frac{\max(x, y) + \min(x, y)}{2}, \tag{5.22a}$$

$$(A_x, A_y) = \frac{\max(x, y) - \min(x, y)}{2}. \tag{5.22b}$$

The lack of quadrature Φ_0 can be obtained from the extremes of the sum of the reduced signals $z = x_r + y_r$. The amplitude $A_z = (\max(z) - \min(z))/2$ is used to obtain the last nonlinearity

$$\Phi_0 = \arcsin\left(\frac{A_z^2 - 2}{2}\right). \tag{5.23}$$

Raw interference signals of an example transient are shown in Fig. 5.3 (c). Fig 5.3 (d) exhibits the unwrapped phase transient.

5.6 Results and Discussion

Following the laser on/off experiment, each unwrapped interferometric transient is recorded and over 100 transients are averaged to produce the phase shift signal illustrated in Fig. 5.4 for copper with diameter of 50.8 mm and excitation power $P = 2$ W. The exposure time $\xi = 250$ ms was used in this example. Continuous lines show the numerical curve fit using Eq. (5.11) (black). The agreement between the theory and the experiments is very good. The contributions to the phase shift from the surface displacement, $\Phi_s(0,t)$, and the thermal lens in the air, $\Phi_f(0,t)$, are also presented. The thermal lens in the air contributes around 4% to the total phase shift. The surface displacement $u_z(0,0,t) = (\lambda_p/4\pi)\Phi_s(0,t)$ is also shown on the right-hand side scale. Note that the peak displacement at the center of the excitation beam is less than 30 nm.

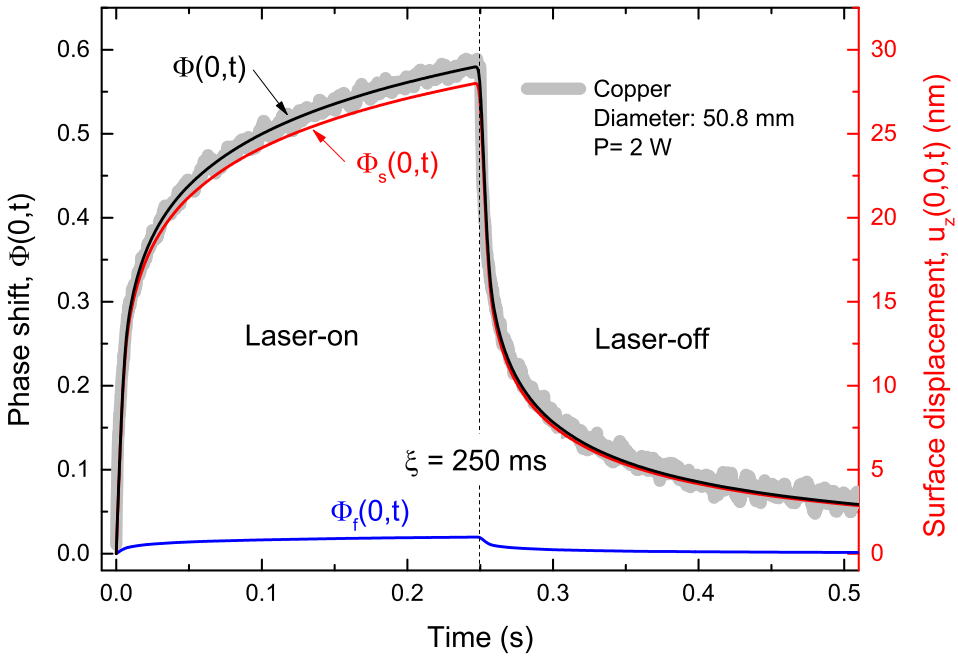

Figure 5.4: Measured time-resolved interferometric phase shift for copper with the diameter of 50.8 mm and the excitation power $P = 2$ W. Continuous lines show the numerical curve fit using Eq. (5.11) (black) and the contributions to the phase shift from the surface displacement (red) and the thermal lens in the air (blue). The surface displacement $u_z(0,0,t) = (\lambda_p/4\pi)\Phi_s(0,t)$ is also shown on the right-hand side scale.

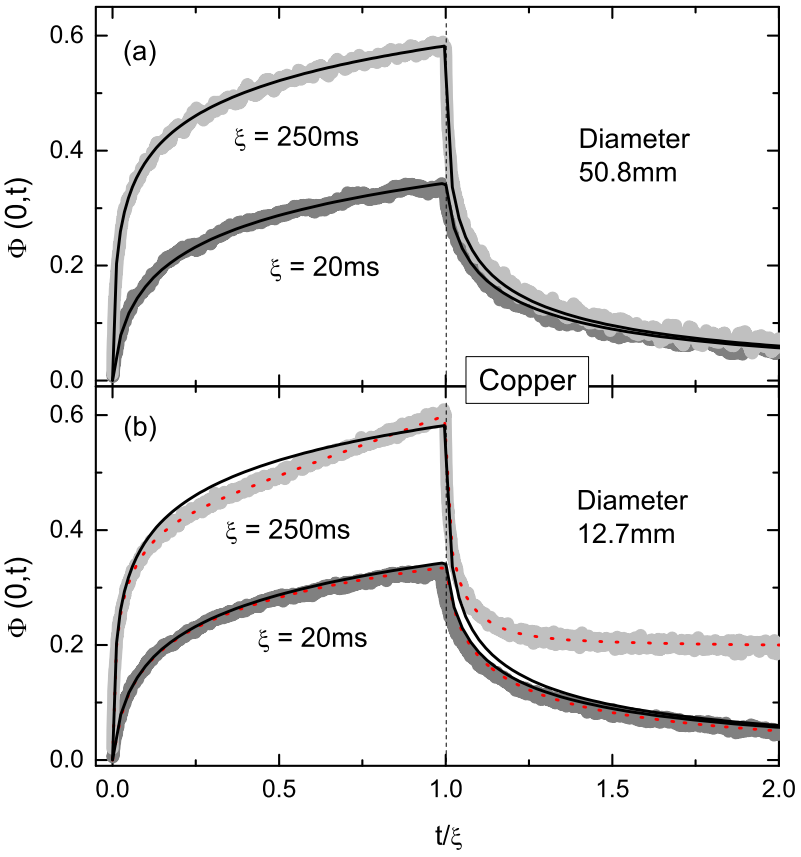

Figure 5.5: Measured interferometric phase shift for copper with the diameter of (a) 50.8 mm and (b) 12.7 mm as a function of the reduced time, t/ξ. Continuous lines show the numerical fits of the curves in (a) using Eq. (5.11). Dotted lines (red) show the numerical predictions using the FEA with the parameters obtained from the fits in (a).

Additional experiments were performed using different excitation times ξ and the results for $\xi = 20$ ms and $\xi = 250$ ms are displayed as a function of the reduced time t/ξ in Fig. 5.5 for copper with different diameters. The laser-off time between each excitation is long enough for the sample to return to its unperturbed thermal state. The samples were excited and probed with laser beam radii $w_e = 646$ μm and $w_{int} = 154$ μm, respectively, at the surface of the sample.

The continuous lines in Fig. 5.5 show the theoretical curve fits of the experimental phase shift transients for the sample with the diameter of 50.8 mm – curves in (a) – to the analytical model, Eq. (5.11). The same curves are shown in (b) for the sample with diameter of 12.7 mm. The theoretical curves are in a good agreement with the experimental transients for the larger sample.

Using the same experimental configuration, a similar behavior was observed for the inox samples. Fig. 5.6 shows the measured phase shifts for the samples with different diameters and exposure times from $\xi = 100$ ms to $\xi = 5000$ ms. The

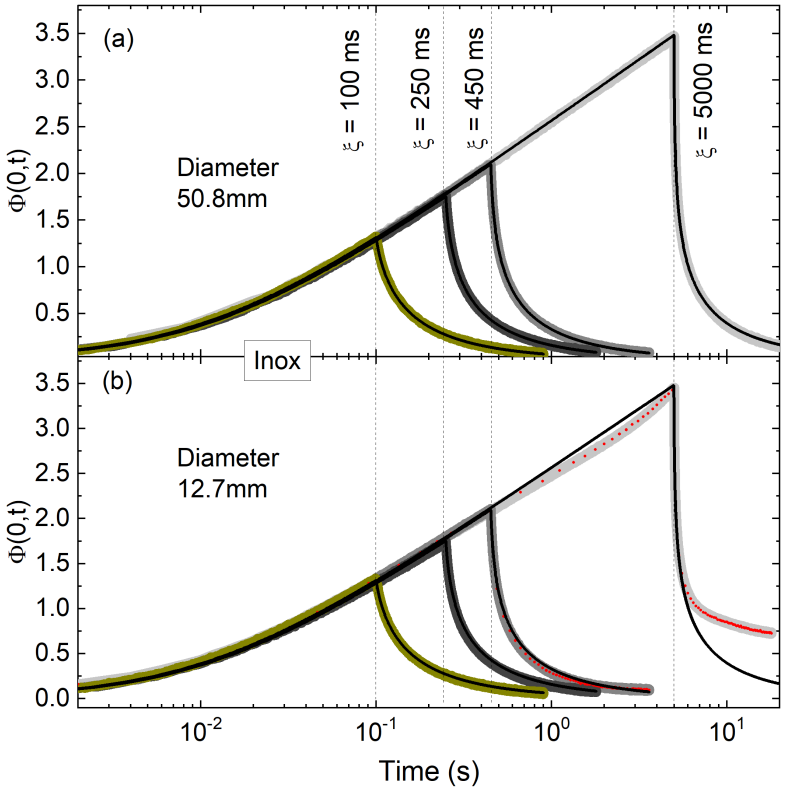

Figure 5.6: Measured interferometric phase shift for inox with diameter of (a) 50.8 mm and (b) 12.7 mm under different excitation time exposure (ξ). Continuous lines show the numerical fits of the curves in (a) using Eq. (5.11). Time is shown on a log scale. Dotted lines (red) show the numerical predictions using FEA with the parameters obtained from the fits in (a).

time axis is presented in a log scale. The excitation power for the measurements was $P = 600$ mW. The continuous lines displayed in Fig. 5.6 (a) and (b) show the theoretical curve fits of the experimental phase shift transients for the sample with the diameter of 50.8 mm to Eq. (5.11). When the theoretical phase shifts for the samples with the diameter of 50.8 mm are projected over the experimental phase shifts for the samples with the diameter of 12.7 mm, Fig. 5.5 (b) for copper and Fig. 5.6 (b) for inox, the curves are in disagreement with the experimental data, especially as the exposure time increases, both for copper ($\xi = 250$ ms) and inox ($\xi > 450$ ms). This is a clear evidence of the edge effects, or the lateral heat accumulation, contributing to the thermoelastic deformation of the samples and the consequent additional phase shift.

The thermal diffusivity and the parameter θ/P are retrieved from the regression analysis. Considering only the numerical fits over the transients for the samples with larger diameters, the results for the thermal diffusivity are within the range of expected values for both copper and inox [89, 119], as shown in

Table 5.1: Physical properties of the metals. Reflectivity R is 0.58 for copper and 0.60 for inox.

Material	D_i (10^{-6}) m^2s^{-1}	θ/P W^{-1}	k_i $Wm^{-1}K^{-1}$	ρc_{ps} (10^6) $Jm^{-3}K^{-1}$	ν	α_T (10^{-6}) K^{-1}
Copper	105 ± 6	0.042 ± 0.001	355 ± 15	3.4 ± 0.2	0.31[a]	17.3[a]
Inox	3.6 ± 0.1	0.93 ± 0.02	15.2 ± 0.7	4.2 ± 0.2	0.29[b]	17.3[b]
Air	21.9[c]		0.026[c]			
$dn_{\text{air}}/dT = -1 \times 10^{-6}$ K^{-1} [c]						

[a] Ref. 89. [b] Ref. 119. [c] Ref. 120.

Table 5.1. For copper, for instance, D ranges from 116×10^{-6} m^2s^{-1} for pure copper to 101×10^{-6} m^2s^{-1} for copper alloy C15500 [89]. Assuming the values of α_T and ν from the literature and the parameter θ measured in this study, the thermal conductivity was calculated and the results for both samples are also in good agreement with the previously reported data [116].

The edge effects were considered in the experimental results by describing the dynamics of the systems using the FEA numerical calculations. The real geometry of the samples and the sample holders were assumed in the calculations. Fig. 5.7 shows the temperature rise and the thermoelastic deformation calculated for inox with the diameter of 12.7 mm and the thickness of 15 mm. The sample holder, made of aluminum, is also illustrated on the same scale. The simulations were performed using the same excitation power as in the experiments and the physical parameters as given in Table 5.1. The excitation exposure time was 5 s.

The edge effects are not clearly seen during the time the sample is excited (laser-on). However, when the laser is turned off, heat diffused rapidly throughout the material and reaches the boundaries of the samples. The heat is also accumulated in the center of the sample where the interferometer senses the phase shift. The heat-coupling between the sample and the surrounding air also contributes to the total phase shift observed experimentally. Analogously, the corresponding thermoelastic deformation of about 700 nm is observed at the center of the excitation beam in the sample during the laser-on excitation. The all-numerical results presented for inox in Fig. 5.7 was also calculated for copper

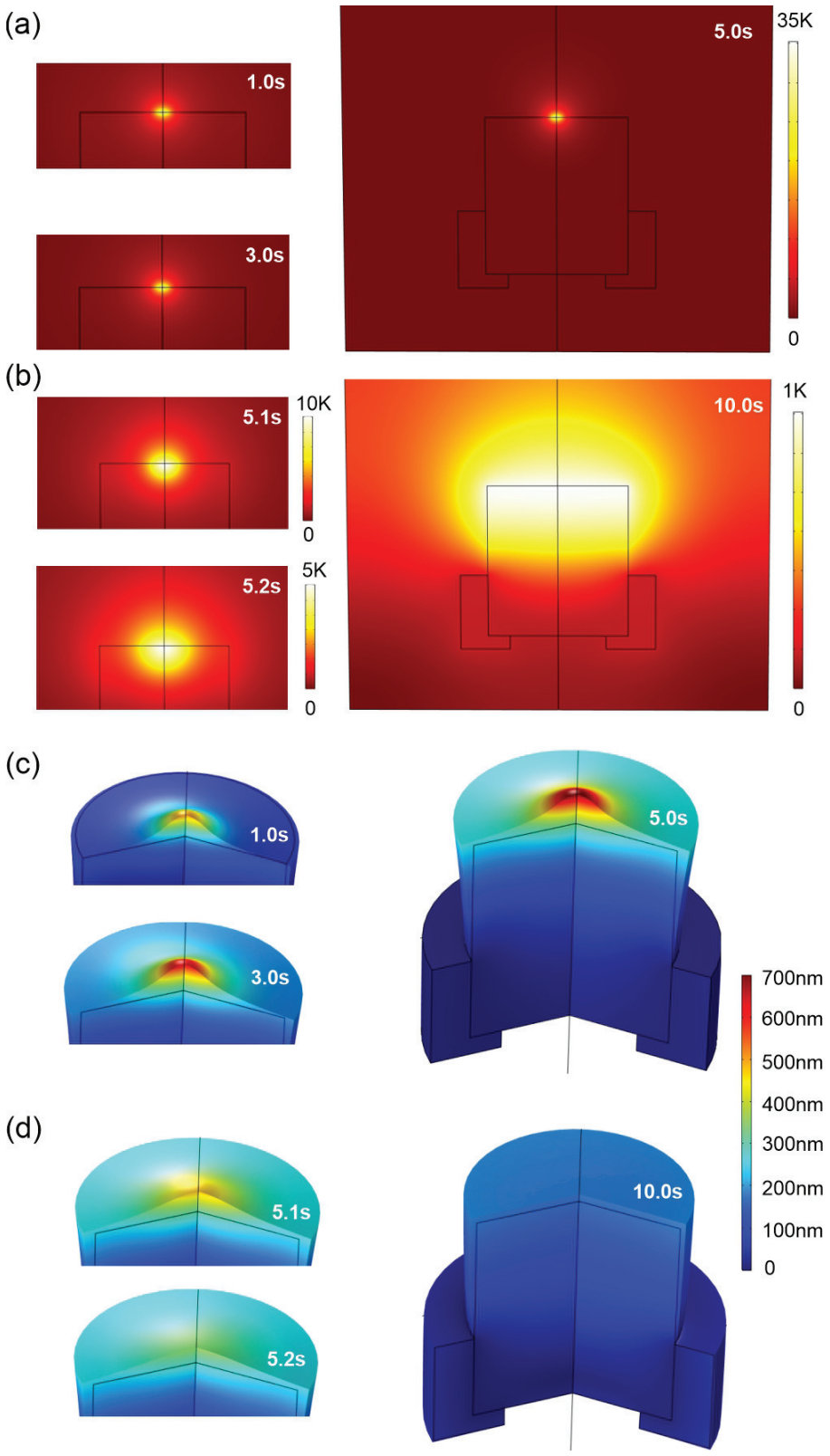

Figure 5.7: Time evolution of the temperature rise and the thermoelastic displacement for laser-on (a,c) and laser-off (b,d) excitation of inox with diameter of $12.7\ \mathrm{mm}$ with an excitation exposure time of 5 s.

(not shown here). These simulations were used to calculate the phase shift considering not only the real geometry of the samples, but also the finite size of the interferometer probe beam. The dotted lines (red) in Fig. 5.5 (b) and Fig. 5.6 (b) show the numerical FEA phase shifts for copper and inox, respectively, with the diameter of 12.7 mm. There is an excellent agreement between the experiments and the numerical solutions for both samples.

With numerical calculations, the phase shift can be further explored as a function of the excitation beam radius used in the experiments. Fig. 5.8 shows how the time-resolved phase shift is dispersed radially on the surface of inox (diameter of 12.7 mm and exposure time of 900 ms). In Fig. 5.8 (a), the shorter

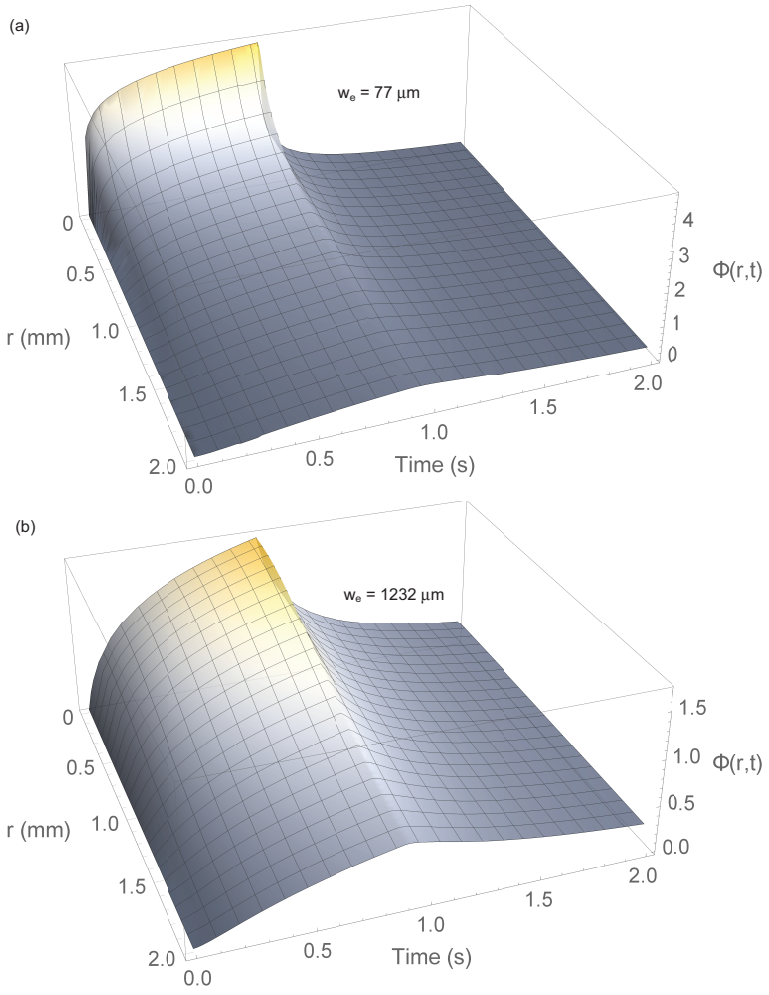

Figure 5.8: FEA numerical calculations of the phase shift $\Phi(r,t)$ for inox with $\xi = 900$ ms as a function of r for different excitation laser radius (a) $w_e = 77$ μm and (b) $w_e = 1232$ μm.

excitation beam radius generates a sharp response in time and a larger phase shift, attenuating further from the excitation origin. However, in Fig. 5.8 (b), the phase shift is prolonged in time and along the surface of the sample as a result of the larger excitation spot.

Although the theoretical phase shift calculated so far assumes an infinitely small probe beam radius capable of probing at $r = 0$, the real experiments are performed with a finite size probe beam radius ($w_{\text{int}} = 154$ μm in this study). The finite dimensions of the probe beam can be described by a theoretical averaged phase shift $\Phi_{\text{avg}}(t)$ considering the Gaussian radial distribution of the interferometer probe beam as

$$\Phi_{\text{avg}}(t) = \frac{\int_0^\infty \Phi(r,t)\exp\left(-2r^2/w_{\text{int}}^2\right)\mathrm{d}r}{\int_0^\infty \exp\left(-2r^2/w_{\text{int}}^2\right)\mathrm{d}r}. \tag{5.24}$$

Figure 5.9 shows the effects of the excitation beam radius on the phase shift as probed by the interferometer considering an infinitely small beam radius and the real finite size of the probe beam. The lines show $\Phi(0,t)$ considering different excitation beam radii, varying from 77 to 1232 μm, compared with the respective averaged phase shift (symbols), $\Phi_{\text{avg}}(t)$, as probed by an interferometer with $w_{\text{int}} = 154$ μm. The inset presents the relative error between the phase shifts $\Phi(0,\xi)/\Phi_{\text{avg}}(\xi)$ as a function of the ratio between the excitation and the probe beam radii. Note that the error decreases significantly as the ratio $w_{\text{e}}/w_{\text{int}}$ increases.

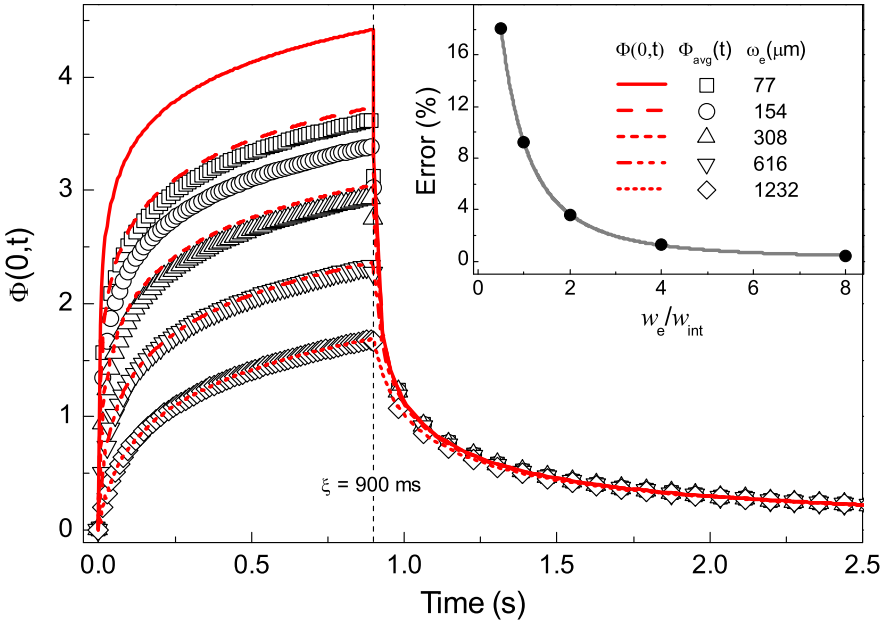

Figure 5.9: FEA numerical calculations of the phase shift $\Phi(0,t)$ for inox with $\xi = 900$ ms as a function of the excitation laser beam radius, varying from 77 μm to 1232 μm, compared with the averaged phase shift $\Phi_{\text{avg}}(t)$, Eq. (5.24), as probed experimentally by the interferometer with a radius of $w_{\text{int}} = 154$ μm. The inset shows the relative error between the phase shifts $\Phi(0,\xi)/\Phi_{\text{avg}}(\xi)$ as a function of the ratio between the excitation and probe beam radii.

5.7 Conclusions

To summarize, we have presented a detailed theoretical and experimental description of the edge effects on the photothermally induced thermoelastic displacement of opaque metals detected by a homodyne quadrature laser interferometer. Both the excitation and the relaxation heat diffusion were investigated and compared to the analytical and the all-numerical solutions for the heat diffusion and the thermoelastic equations describing the phase shift on the sample. The finite geometry of the samples was crucial in determining how the temperature was distributed across the material and how this affected the interferometer phase shift measurements. The optical path change due to the surface thermoelastic deformation and the thermal lens in the surrounding air was decoded from the interferometric signal using analytical and numerical tools. The boundary/edge effects were found to be relevant to properly describe the interferomet-

ric signals and the tools developed in this study were found to be applicable to describe not only the phase shift sensed by the interferometer but also to contribute to the photothermal-based technologies employing similar detection mechanisms.

Part IV

Final Remarks

CHAPTER 6

SUMMARY AND OUTLOOK

In this study, we proposed a novel methodology for investigating the thermal, optical and mechanical properties of metals, through the combination of a photothermal mirror and an interferometric detection. The photothermal mirror technique, which has previously been shown to effectively characterize laser induced thermoelastic waves within metals, thermo-optical and mechanical properties of semiconductors and semi-transparent materials, and radiation pressure effects in dielectric liquids, was combined with the interferometric detection method to provide a more comprehensive analysis of the sample.

The proposed methodology utilizes the wavefront distortion caused by the surface displacement of the sample and the thermal lens in the coupling fluid, which are sensed by the probe beams from both techniques. This allows for direct access to the phase shift at a single location on the sample's surface (interferometer) in addition to the convoluted signal arising from the total wavefront distortion in the media (photothermal mirror).

In addition, we also presented a detailed experimental description of the edge effects on the photothermal induced thermoelastic displacement of opaque met-

als detected by a homodyne quadrature laser interferometer. Both the excitation and the relaxation heat diffusion were investigated and compared to the analytical and the all-numerical solutions for the heat diffusion and the thermoelastic equations describing the phase shift on the sample. The finite geometry of the samples was crucial in determining the distribution of temperature across the material and how this affected the interferometer phase shift measurements. The boundary/edge effects were found to be significant in properly describing the interferometric signals, and the tools developed in this study were found to be applicable to not only describe the phase shift sensed by the interferometer, but also to contribute to the advancement of photothermal-based technologies utilizing similar detection mechanisms.

Overall, this proposed methodology offers substantial improvements for single-shot analysis and provides compelling support for describing the origins of light and matter interaction effects. The combination of the two techniques, the photothermal mirror and the interferometric detection method, provides a more complete understanding of the sample under investigation and is a valuable addition to the field of materials science.

REFERENCES

[1] Bialkowski, S., Astrath, N. G. C. & Proskurnin, M. *Photothermal spectroscopy methods*. Chemical analysis (Wiley, Hoboken, NJ, 2019), second edition edn.

[2] Malacarne, L. C. *et al.* Nanoscale surface displacement detection in high absorbing solids by time-resolved thermal mirror. *Appl. Phys. Lett.* **92**, 131903 (2008). URL doi.org/10.1063/1.2905261.

[3] Beyersdorf, P. & Cordier, M. Measurement of thermo-elastic deformation of an optic using a polarization-based shearing interferometer. *Appl. Opt., AO* **51**, 7426–7433 (2012). URL doi.org/10.1364/AO.51.007426.

[4] Goetz, G. *et al.* Interferometric mapping of material properties using thermal perturbation. *Proceedings of the National Academy of Sciences* **115**, E2499–E2508 (2018). URL doi.org/10.1073/pnas.1712763115.

[5] Kurzmann, V., Stöhr, J., Tochtrop, M. & Kassing, R. Interferometric measurement of thermal expansion. *Materials Science and Engineering: A* **122**, 117–120 (1989). URL doi.org/10.1016/0921-5093(89)90782-X.

[6] Shen, Y.-c. & Hess, P. Real-time detection of laser-induced transient gratings and surface acoustic wave pulses with a Michelson interferometer. *Journal of Applied Physics* **82**, 4758–4762 (1997). URL doi.org/10.1063/1.366332.

[7] Carp, S. A. & Venugopalan, V. Optoacoustic imaging based on the interferometric measurement of surface displacement. *JBO* **12**, 064001 (2007). URL doi.org/1083-3668,1560-2281.

[8] Požar, T., Gregorčič, P. & Možina, J. A precise and wide-dynamic-range displacement-measuring homodyne quadrature laser interferometer. *Appl. Phys. B* **105**, 575–582 (2011). URL doi.org/10.1007/s00340-011-4512-5.

[9] Pogačnik, A., Požar, T., Kalin, M. & Možina, J. A Homodyne Quadrature Laser Interferometer for Micro-Asperity Deformation Analysis. *Sensors* **13**, 703–720 (2013). URL doi.org/10.3390/s130100703.

[10] Scruby, C. B. & Drain, L. E. *Laser ultrasonics: techniques and applications* (A. Hilger, Bristol, England ; Philadelphia, 1990).

[11] Dhanesh, N. & Kapuria, S. Edge effects in elastic and piezoelectric laminated panels under thermal loading. *Journal of Thermal Stresses* **41**, 1577–1596 (2018). URL https://www.tandfonline.com/doi/full/10.1080/01495739.2018.1524732.

[12] Wolf, J. *et al.* Lens-term- and edge-effect in X-ray grating interferometry. *Biomed. Opt. Express* **6**, 4812 (2015). URL https://opg.optica.org/abstract.cfm?URI=boe-6-12-4812.

[13] Sell, J. A. (ed.) *Photothermal investigations of solids and fluids* (Academic Press, Boston, 1989).

[14] Rwendland. Expansion joint, hayle (2011). URL http://commons.wikimedia.org/wiki/User:Rwendland. Retrieved from Wikimedia Commons. Licensed under Creative Commons Attribution-ShareAlike 3.0 Unported.

[15] US Department of Transportation. Rail buckle from high heat (2012). URL https://toolkit.climate.gov/image/1001. Image in the public domain.

[16] Bell, A. G. THE PRODUCTION OF SOUND BY RADIANT ENERGY. *Science* **os-2**, 242–253 (1881). URL https://www.sciencemag.org/lookup/doi/10.1126/science.os-2.49.242.

[17] Bell, A. G. On the production and reproduction of sound by light. *American Journal of Science* **s3-20**, 305–324 (1880). URL http://www.ajsonline.org/cgi/doi/10.2475/ajs.s3-20.118.305.

[18] Parker, J. G. Optical Absorption in Glass: Investigation Using an Acoustic Technique. *Appl. Opt.* **12**, 2974 (1973). URL https://opg.optica.org/abstract.cfm?URI=ao-12-12-2974.

[19] Rosencwaig, A. & Gersho, A. Photoacoustic Effect with Solids: A Theoretical Treatment. *Science* **190**, 556–557 (1975). URL https://www.science.org/doi/10.1126/science.190.4214.556.

[20] Rosencwaig, A. & Gersho, A. Theory of the photoacoustic effect with solids. *Journal of Applied Physics* **47**, 64–69 (1976). URL http://aip.scitation.org/doi/10.1063/1.322296.

[21] Mura, J. *Utilização Da Técnica Piezo-Piroelétrica Para Caracterização Fototérmica De Polímeros Em Função Da Temperatura*. PhD Thesis, Universidade Estadual de Maringá, Maringá (2000). URL http://www.pfi.uem.br/wp-content/uploads/2015/09/joao_mura_2005_final.pdf.

[22] Liu, Y. *et al.* Chemical Design of Activatable Photoacoustic Probes for Precise Biomedical Applications. *Chem. Rev.* **122**, 6850–6918 (2022). URL https://pubs.acs.org/doi/10.1021/acs.chemrev.1c00875.

[23] Su, J. L. *et al.* Advances in clinical and biomedical applications of photoacoustic imaging. *Expert Opinion on Medical Diagnostics* **4**, 497–510 (2010). URL http://www.tandfonline.com/doi/full/10.1517/17530059.2010.529127.

[24] Vu, T., Razansky, D. & Yao, J. Listening to tissues with new light: recent technological advances in photoacoustic imaging. *J. Opt.* **21**, 103001 (2019). URL https://iopscience.iop.org/article/10.1088/2040-8986/ab3b1a.

[25] Leite, R. C. C., Moore, R. S. & Whinnery, J. R. Low Absorption Measurements By Means Of The Thermal Lens Effect Using An He–Ne Laser. *Appl. Phys. Lett.* **5**, 141–143 (1964). URL http://aip.scitation.org/doi/10.1063/1.1754089.

[26] Gordon, J. P., Leite, R. C. C., Moore, R. S., Porto, S. P. S. & Whinnery, J. R. Long-Transient Effects in Lasers with Inserted Liquid Samples. *Journal of Applied Physics* **36**, 3–8 (1965). URL http://aip.scitation.org/doi/10.1063/1.1713919.

[27] Hu, C. & Whinnery, J. R. New Thermooptical Measurement Method and a Comparison with Other Methods. *Appl. Opt.* **12**, 72 (1973). URL https://opg.optica.org/abstract.cfm?URI=ao-12-1-72.

[28] Fang, H. L. & Swofford, R. L. Highly excited vibrational states of molecules by thermal lensing spectroscopy and the local mode model. I. $CHCl_3$, $CHBr_3$, CH_2Cl_2, CH_2Br_2. *The Journal of Chemical Physics* **72**, 6382–6389 (1980). URL http://aip.scitation.org/doi/10.1063/1.439163.

[29] Shen, J., Lowe, R. D. & Snook, R. D. A model for cw laser induced mode-mismatched dual-beam thermal lens spectrometry. *Chemical Physics* **165**, 385–396 (1992). URL https://linkinghub.elsevier.com/retrieve/pii/030101049287053C.

[30] Malacarne, L. C. *et al.* Analytical solution for mode-mismatched thermal lens spectroscopy with sample-fluid heat coupling. *Journal of Applied Physics* **107**, 053104 (2010). URL http://aip.scitation.org/doi/10.1063/1.3309762.

[31] Malacarne, L. C., Astrath, N. G. C. & Baesso, M. L. Unified theoretical model for calculating laser-induced wavefront distortion in optical materials. *J. Opt. Soc. Am. B* **29**, 1772 (2012). URL https://opg.optica.org/abstract.cfm?URI=josab-29-7-1772.

[32] Malacarne, L. C., Savi, E. L., Baesso, M. L., Lenzi, E. K. & Astrath, N. G. C. Role of Photophysics Processes in Thermal Lens Spectroscopy of Fluids: A Theoretical Study. *J. Phys. Chem. A* **118**, 5983–5988 (2014). URL https://pubs.acs.org/doi/10.1021/jp505255a.

[33] Sheik-bahae, M., Said, A. A. & Van Stryland, E. W. High-sensitivity, single-beam n_2 measurements. *Opt. Lett.* **14**, 955 (1989). URL https://opg.optica.org/abstract.cfm?URI=ol-14-17-955.

[34] Sehnem, A. L., Espinosa, D., Gonçalves, E. S. & Figueiredo Neto, A. M. Thermal Lens Phenomenon Studied by the Z-Scan Technique: Measurement of the Thermal Conductivity of Highly Absorbing Colloidal Solutions. *Braz J Phys* **46**, 547–555 (2016). URL http://link.springer.com/10.1007/s13538-016-0434-3.

[35] Messias, D. N. *Estudo das contribuições térmica e eletrônica na variação do índice de refração de materiais dopados com íons*

emissores. PhD Thesis, Universidade de São Paulo„ São Carlos (2006). URL https://www.teses.usp.br/teses/disponiveis/76/76131/tde-21112006-092927/publico/tese_Djalmir.pdf.

[36] dos Santos, B. H. B. *Estudo das contribuições térmica e eletrônica do índice de refração não linear utilizando a técnica de Z-scan resolvida no tempo*. PhD Thesis, Universidade Estadual de Maringá, Maringá (2009). URL http://www.pfi.uem.br/wp-content/uploads/2015/09/bruno_henrique_bononi_Santos_2009.pdf.

[37] Nordal, P.-E. & Kanstad, S. O. Photothermal Radiometry. *Phys. Scr.* **20**, 659–662 (1979). URL https://iopscience.iop.org/article/10.1088/0031-8949/20/5-6/020/pdf.

[38] Tam, A. C. & Sullivan, B. Remote sensing applications of pulsed photothermal radiometry. *Appl. Phys. Lett.* **43**, 333–335 (1983). URL http://aip.scitation.org/doi/10.1063/1.94346.

[39] Horne, K., Ban, H., Mandelis, A. & Matvienko, A. Photothermal radiometry measurement of thermophysical property change of an ion-irradiated sample. *Materials Science and Engineering: B* **177**, 164–167 (2012). URL https://linkinghub.elsevier.com/retrieve/pii/S0921510711004971.

[40] Boccara, A. C., Fournier, D. & Badoz, J. Thermo-optical spectroscopy: Detection by the "mirage effect". *Appl. Phys. Lett.* **36**, 130–132 (1980). URL http://aip.scitation.org/doi/10.1063/1.91395.

[41] Boccara, A. C., Jackson, W., Amer, N. M. & Fournier, D. Sensitive photothermal deflection technique for measuring absorption in optically thin media. *Opt. Lett.* **5**, 377 (1980). URL https://opg.optica.org/abstract.cfm?URI=ol-5-9-377.

[42] McLean, E. A., Sica, L. & Glass, A. J. INTERFEROMETRIC OBSERVATION OF ABSORPTION INDUCED INDEX CHANGE ASSOCIATED WITH THERMAL BLOOMING. *Appl. Phys. Lett.* **13**, 369–371 (1968). URL http://aip.scitation.org/doi/10.1063/1.1652475.

[43] Longaker, P. R. & Litvak, M. M. Perturbation of the Refractive Index of Absorbing Media by a Pulsed Laser Beam. *Journal of Applied Physics* **40**, 4033–4041 (1969). URL http://aip.scitation.org/doi/10.1063/1.1657139.

[44] Britannica, The Editors of Encyclopaedia. Electromagnetic spectrum. https://www.britannica.com/science/electromagnetic-spectrum (2019).

[45] Yu, F. *et al.* Photonic slide rule with metasurfaces. *Light Sci Appl* **11**, 77 (2022). URL https://www.nature.com/articles/s41377-022-00765-0.

[46] Kim, M. K. Digital holographic microscopy for surface profilometry. In Mendoza-Santoyo, F., De la Torre-Ibarra, M., del Socorro Hernández-Montes, M. & Flores Moreno, J. M. (eds.) *Full Field Optical Metrology and Applications*, 9–1–9–15 (IOP Publishing, 2022). URL https://iopscience.iop.org/book/edit/978-0-7503-3027-5/chapter/bk978-0-7503-3027-5ch9.

[47] Monnier, J. D. Optical interferometry in astronomy. *Rep. Prog. Phys.* **66**, 789–857 (2003). URL https://iopscience.iop.org/article/10.1088/0034-4885/66/5/203.

[48] Abbott, B. *et al.* GW151226: Observation of Gravitational Waves from a 22-Solar-Mass Binary Black Hole Coalescence. *Phys. Rev. Lett.* **116**, 241103 (2016). URL https://link.aps.org/doi/10.1103/PhysRevLett.116.241103.

[49] Bourdarot, G. Heterodyne interferometry: review and prospects. In Mérand, A., Sallum, S. & Sanchez-Bermudez, J. (eds.) *Optical and Infrared Interferometry and Imaging VIII*, 39 (SPIE, Montréal, Canada, 2022). URL https://www.spiedigitallibrary.org/conference-proceedings-of-spie/12183/2635601/Heterodyne-interferometry-review-and-prospects/10.1117/12.2635601.full.

[50] Angerhausen, D., Alei, E., Quanz, S. & LIFE Initiative, T. Status and progress of the Large Interferometer For Exoplanets (LIFE) mission . other, display (2022). URL https://meetingorganizer.copernicus.org/EPSC2022/EPSC2022-1148.html.

[51] Zhang, C. Research on thin film lubrication: state of the art. *Tribology International* **38**, 443–448 (2005). URL https://linkinghub.elsevier.com/retrieve/pii/S0301679X04002336.

[52] Wang, Y., Xie, F., Ma, S. & Dong, L. Review of surface profile measurement techniques based on optical interferometry. *Optics and Lasers in Engineering* **93**, 164–170 (2017). URL https://linkinghub.elsevier.com/retrieve/pii/S0143816617300659.

[53] Hu, D. J. J. & Humbert, G. Special Issue "Novel Specialty Optical Fibers and Applications": An Overview. *Photonics* **9**, 497 (2022). URL https://www.mdpi.com/2304-6732/9/7/497.

[54] Hariharan, P. *Basics of interferometry* (Elsevier Academic Press, London, 2007), 2nd ed edn. URL doi.org/10.1016/B978-0-12-373589-8.X5000-7. OCLC: ocm70158467.

[55] Paris, M. G. A. Entanglement and visibility at the output of a Mach-Zehnder interferometer. *Phys. Rev. A* **59**, 1615–1621 (1999). URL https://link.aps.org/doi/10.1103/PhysRevA.59.1615.

[56] Stroke, G. & Funkhouser, A. Fourier-transform spectroscopy using holographic imaging without computing and with stationary interferometers. *Physics Letters* **16**, 272–274 (1965). URL https://linkinghub.elsevier.com/retrieve/pii/0031916365908462.

[57] Nolte, D. D. *Optical interferometry for biology and medicine*. No. v. 1 in Bioanalysis (Springer, New York, 2011). OCLC: ocn733249835.

[58] Zehnder, L. Ein neuer Interferenzrefraktor. *Zeitschrift für Instrumentenkunde* **11**, 275–285 (1891).

[59] Jamin. Neuer Interferential-Refractor. *Ann. Phys. Chem.* **174**, 345–349 (1856). URL https://onlinelibrary.wiley.com/doi/10.1002/andp.18561740619.

[60] Mach, L. Ueber einen Interferenzrefraktor. *Zeitschrift für Instrumentenkunde* **12**, 89–93 (1892).

[61] Lopez, J., Echeverry, D., Zambrano, G., Castro, L. & Prieto, P. Gas Temperature Determination of an AC Arc Discharge at Atmospheric Pressure in Air Using a Mach–Zehnder Interferometer. *IEEE Trans. Plasma Sci.* **34**, 115–120 (2006). URL http://ieeexplore.ieee.org/document/1593854/.

[62] Zhou, X., Zeng, R., Zhuang, C. & Chen, S. Experimental study on thermal characteristics of positive leader discharges using Mach-Zehnder interferometry. *Physics of Plasmas* **22**, 063508 (2015). URL http://aip.scitation.org/doi/10.1063/1.4922660.

[63] Paris, M. G. A. Entanglement and visibility at the output of a Mach-Zehnder interferometer. *Phys. Rev. A* **59**, 1615–1621 (1999). URL https://link.aps.org/doi/10.1103/PhysRevA.59.1615.

[64] Yupapin, P. P. Entangled photon generation using a fiber optic Mach-Zehnder interferometer incorporating the nonlinear effect in a fiber ring resonator. *J. Nanophoton* **1**, 013504 (2007). URL http://nanophotonics.spiedigitallibrary.org/article.aspx?doi=10.1117/1.2516897.

[65] Haack, G., Förster, H. & Büttiker, M. Parity detection and entanglement with a Mach-Zehnder interferometer. *Phys. Rev. B* **82**, 155303 (2010). URL https://link.aps.org/doi/10.1103/PhysRevB.82.155303.

[66] Sagnac, G. L'ether lumineux demontre par l'effet du vent relatif d'ether dans un interferometre en rotation uniforme. *Comptes Rendus* **157**, 708–710 (1913).

[67] Sagnac, G. Sur la preuve de la réalité de l'éther lumineux par l'expérience de l'interférographe tournant. *Comptes Rendus* **157**, 1410–1413 (1913).

[68] Gustavson, T. L., Landragin, A. & Kasevich, M. A. Rotation sensing with a dual atom-interferometer Sagnac gyroscope. *Class. Quantum Grav.* **17**, 2385–2398 (2000). URL https://iopscience.iop.org/article/10.1088/0264-9381/17/12/311.

[69] Culshaw, B. The optical fibre Sagnac interferometer: an overview of its principles and applications. *Meas. Sci. Technol.* **17**, R1–R16 (2006). URL https://iopscience.iop.org/article/10.1088/0957-0233/17/1/R01.

[70] Michelson, A. A. & Morley, E. W. On the relative motion of the Earth and the luminiferous ether. *American Journal of Science* **s3-34**, 333–345 (1887). URL http://www.ajsonline.org/cgi/doi/10.2475/ajs.s3-34.203.333.

[71] Abbott, B. *et al.* Detector description and performance for the first coincidence observations between LIGO and GEO. *Nuclear Instruments and*

Methods in Physics Research Section A: Accelerators, Spectrometers, Detectors and Associated Equipment **517**, 154–179 (2004). URL https://linkinghub.elsevier.com/retrieve/pii/S0168900203028675.

[72] Lukasievicz, G. V. B. *et al.* Pulsed-Laser Time-Resolved Thermal Mirror Technique in Low-Absorbance Homogeneous Linear Elastic Materials. *Appl Spectrosc* **67**, 1111–1116 (2013). URL doi.org/10.1366/13-07068.

[73] Astrath, N. G. C., Lukasievicz, G. V. B., Malacarne, L. C. & Bialkowski, S. E. Surface deformation effects induced by radiation pressure and electrostriction forces in dielectric solids. *Appl. Phys. Lett.* **102**, 231903 (2013). URL doi.org/10.1063/1.4809924.

[74] Astrath, N. G. C., Malacarne, L. C., Baesso, M. L., Lukasievicz, G. V. B. & Bialkowski, S. E. Unravelling the effects of radiation forces in water. *Nat Commun* **5**, 4363 (2014). URL http://www.nature.com/articles/ncomms5363.

[75] Capeloto, O. A. *et al.* Pulsed photothermal mirror technique: characterization of opaque materials. *Appl. Opt., AO* **53**, 7985–7991 (2014). URL doi.org/10.1364/AO.53.007985.

[76] Capeloto, O. A. *et al.* Quantitative assessment of radiation force effect at the dielectric air-liquid interface. *Sci Rep* **6**, 20515 (2016). URL doi,org/10.1038/srep20515.

[77] Gusev, V. E. & Karabutov, A. A. *Laser optoacoustics* (American Institute of Physics, New York, 1993). OCLC: 624189504.

[78] Capeloto, O. A. *et al.* Generation and detection of thermoelastic waves in metals by a photothermal mirror method. *Appl. Phys. Lett.* **109**, 191908 (2016). URL doi.org/10.1063/1.4967530.

[79] Reibold, R. & Molkenstruck, W. Laser Interferometric Measurement and Computerized Evaluation of Ultrasonic Displacements. *Acta Acustica united with Acustica* **49**, 205–211 (1981).

[80] Greco, V., Molesini, G. & Quercioli, F. Accurate polarization interferometer. *Review of Scientific Instruments* **66**, 3729–3734 (1995). URL doi.org/10.1063/1.1145429.

[81] Požar, T. & Možina, J. Detection of subnanometer ultrasonic displacements. In Sattler, K. D. (ed.) *Fundamentals of picoscience* (CRC Press, Taylor & Francis Group, Boca Raton, FL, 2014). URL doi.org/10.1201/b15523.

[82] Požar, T. & Možina, J. Mechanical wave motion due to the radiation pressure on gain or absorptive rods. *Opt. Lett., OL* **38**, 1754–1756 (2013). URL doi.org/10.1364/OL.38.001754.

[83] Lazar, J., Holá, M., Číp, O., Hrabina, J. & Oulehla, J. Interferometric system with tracking refractometry capability in the measuring axis. *Meas. Sci. Technol.* **24**, 067001 (2013). URL doi.org/10.1088/0957-0233/24/6/067001.

[84] Lukasievicz, G. V. B. *et al.* A Theoretical and Experimental Study of Time-Resolved Thermal Mirror with Non-Absorbing Heat-Coupling Fluids. *Appl Spectrosc* **66**, 1461–1467 (2012). URL doi.org/10.1366/12-06743.

[85] Spicer, J. B. & Hurley, D. H. Epicentral and near epicenter surface displacements on pulsed laser irradiated metallic surfaces. *Appl. Phys. Lett.* **68**, 3561–3563 (1996). URL doi.org/10.1063/1.116637. Publisher: American Institute of Physics.

[86] Gregorčič, P., Požar, T. & Možina, J. Quadrature phase-shift error analysis using a homodyne laser interferometer. *Opt. Express, OE* **17**, 16322–16331 (2009). URL doi.org/10.1364/OE.17.016322.

[87] Požar, T. & Možina, J. Enhanced ellipse fitting in a two-detector homodyne quadrature laser interferometer. *Meas. Sci. Technol.* **22**, 085301 (2011). URL doi.org/10.1088/0957-0233/22/8/085301.

[88] Taylor, L. & Talghader, J. Monitoring and analysis of thermal deformation waves with a high-speed phase measurement system. *Appl. Opt., AO* **54**, 9010–9016 (2015). URL doi.org/10.1364/AO.54.009010.

[89] ASM Handbook Committee (ed.) *Properties and Selection: Nonferrous Alloys and Special-Purpose Materials*, vol. 2 (ASM International, 1990). URL doi.org/10.31399/asm.hb.v02.9781627081627.

[90] Nugroho, H. A., Khusna, D. A. & Frannita, E. L. Detection and Classification of Breast Nodule on Ultrasound Images using Edge Feature. *International Journal of Advances in Soft Computing and its Applications*

11, 64–80 (2019). URL http://ijasca.zuj.edu.jo/PapersUploaded/2019.1.5.pdf.

[91] Mishra, A., Yadav, R. & Kumar, L. Edge Detection Through Dynamic Programming in Ultrasound Gray Scale Digital Images. In Solanki, V. K., Hoang, M. K., Lu, Z. J. & Pattnaik, P. K. (eds.) *Intelligent Computing in Engineering*, vol. 1125, 177–185 (Springer Singapore, Singapore, 2020). URL doi.org/10.1007/978-981-15-2780-7_22.

[92] Almond, D. P. & Lau, S. K. Edge effects and a method of defect sizing for transient thermography. *Appl. Phys. Lett.* **62**, 3369–3371 (1993). URL doi.org/10.1063/1.109074.

[93] Su, L., Yu, X., Li, K., Yao, X. & Pecht, M. Simulation and Experimental Verification of Edge Blurring Phenomenon in Microdefect Inspection Based on High-Frequency Ultrasound. *IEEE Access* **7**, 11515–11525 (2019). URL doi.org/10.1109/ACCESS.2019.2892231.

[94] Shen, H., Hu, J. & Yao, Z. Analysis and control of edge effects in laser bending. *Optics and Lasers in Engineering* **48**, 305–315 (2010). URL doi.org/10.1016/j.optlaseng.2009.11.005.

[95] Hu, J., Xu, H. & Dang, D. Modeling and reducing edge effects in laser bending. *Journal of Materials Processing Technology* **213**, 1989–1996 (2013). URL doi.org/10.1016/j.jmatprotec.2013.05.007.

[96] Shi, Y., Zhang, C., Sun, G. & Li, C. Study on reducing edge effects by using assistant force in laser forming. *Journal of Materials Processing Technology* **227**, 169–177 (2016). URL doi.org/10.1016/j.jmatprotec.2015.08.018.

[97] Taudt, C. *et al.* Characterization of edge effects in precision low-coherence interferometry using broadband light sources. 1032932 (Munich, Germany, 2017). URL doi.org/10.1117/12.2270318.

[98] Lv, C., Wang, K., Gu, G. & Pan, Y. Accurate full-edge detection and depth measurement of internal defects using digital speckle pattern interferometry. *NDT & E International* **102**, 1–8 (2019). URL doi.org/10.1016/j.ndteint.2018.10.009.

[99] Weiss, H. A. *et al.* Neutron grating interferometry investigation of punching-related local magnetic property deteriorations in electrical steels. *Journal*

of Magnetism and Magnetic Materials **474**, 643–653 (2019). URL doi.org/10.1016/j.jmmm.2018.10.098.

[100] Ritter, K. & Thiele, K. Monitoring Micro-damage Evolution in Structural Steel S355 Using Speckle Interferometry. In Abdel Wahab, M. (ed.) *Proceedings of the 7th International Conference on Fracture Fatigue and Wear*, 427–437 (Springer Singapore, Singapore, 2019). URL doi.org/10.1007/978-981-13-0411-8_38.

[101] Rodríguez-Martín, R., Castro, I., Ocaña, I. & Martínez-Esnaola, J. M. Use of electronic speckle pattern interferometry in the detection of fatigue failure in high strength steels. *Engineering Failure Analysis* **17**, 226–235 (2010). URL doi.org/10.1016/j.engfailanal.2009.06.005.

[102] Peng, X., Asundi, A., Chen, Y. & Xiong, Z. Study of the mechanical properties of Nd:YVO_4 crystal by use of laser interferometry and finite-element analysis. *Appl. Opt., AO* **40**, 1396–1403 (2001). URL doi.org/10.1364/AO.40.001396.

[103] Li, J., Sheng Li, J., Yang Pan, Y. & Li, R. Compressive Optical Image Encryption. *Sci Rep* **5**, 10374 (2015). URL doi.org/10.1038/srep10374.

[104] Li, J. *et al.* Optical image hiding based on dual-channel simultaneous phase-shifting interferometry and compressive sensing. *Appl. Phys. B* **123**, 4 (2016). URL doi.org/10.1007/s00340-016-6592-8.

[105] Hairaye, C., Mermet, F., Engel, T., Montgomery, P. C. & Fontaine, J. Functionalization of surfaces by ultrafast laser micro/nano structuring. *J. Phys.: Conf. Ser.* **558**, 012063 (2014). URL doi.org/10.1088/1742-6596/558/1/012063.

[106] Leong-Hoï, A. *et al.* Detection of defects in a transparent polymer with high resolution tomography using white light scanning interferometry and noise reduction. 952807 (Munich, Germany, 2015). URL doi.org/10.1117/12.2184559.

[107] Pramatarova, L. *et al.* The Advantages of Polymer Composites with Detonation Nanodiamond Particles for Medical Applications. In Pramatarova, L. (ed.) *On Biomimetics* (InTech, 2011). URL doi.org/10.5772/22903.

[108] Pecheva, E., Montgomery, P., Montaner, D. & Pramatarova, L. White Light Scanning Interferometry Adapted for Large-Area Optical Analysis of Thick

and Rough Hydroxyapatite Layers. *Langmuir* **23**, 3912–3918 (2007). URL doi.org/10.1021/la061593f.

[109] Leong-Hoi, A., Montgomery, P. C., Serio, B., Uhring, W. & Pecheva, E. Improvement in measurements of hydroxyapatite layers by hybrid high dynamic range image processing in white-light interferometry. *Materials Today: Proceedings* **4**, S36–S43 (2017). URL doi.org/10.1016/j.matpr.2017.05.008.

[110] Monchalin, J.-P. Laser-ultrasonics: principles and industrial applications. In *Ultrasonic and Advanced Methods for Nondestructive Testing and Material Characterization*, 79–115 (World Scientific, 2007). URL doi.org/10.1142/9789812770943_0004.

[111] Dong, B., Sun, C. & Zhang, H. F. Optical Detection of Ultrasound in Photoacoustic Imaging. *IEEE Transactions on Biomedical Engineering* **64**, 4–15 (2017). URL doi.org/10.1109/TBME.2016.2605451.

[112] Wissmeyer, G., Pleitez, M. A., Rosenthal, A. & Ntziachristos, V. Looking at sound: optoacoustics with all-optical ultrasound detection. *Light Sci Appl* **7**, 53 (2018). URL doi.org/10.1038/s41377-018-0036-7.

[113] BIPM. Appendix 4. Historical notes on the development of the International System of Units and its base units. In *Le Système international d'unités (SI) / The International System of Units (SI)* (Bureau international des poids et mesures, Sèvres, France, 2019). URL https://www.bipm.org/en/publications/si-brochure.

[114] Lenkova, G. A. *et al.* Laser interferometer for length measurements. *Meas Tech* **14**, 1822–1825 (1971). URL doi.org/10.1007/BF00994940.

[115] Svitlov, S. & Araya, A. Homodyne interferometry with quadrature fringe detection for absolute gravimeter. *Appl. Opt., AO* **53**, 3548–3555 (2014). URL doi.org/10.1364/AO.53.003548.

[116] Flizikowski, G. A. S. *et al.* Laser induced thermoelastic surface displacement in solids detected simultaneously by photothermal mirror and interferometry. *Opt. Express* **28**, 7116 (2020). URL doi.org/10.1364/OE.386344.

[117] Carslaw, H. S. & Jaeger, J. C. *Conduction of heat in solids* (Clarendon, Oxford, 1980).

[118] Nowacki, W. *Thermoelasticity* (Pergamon Press, Oxford, UK, 1986). URL doi.org/10.1016/C2013-0-03247-1.

[119] ASM Handbook Committee (ed.) *Properties and Selection: Irons, Steels, and High-Performance Alloys*, vol. 1 (ASM International, 1990). URL doi.org/10.31399/asm.hb.v01.9781627081610.

[120] Haynes, W. M., Haynes, W. M., Lide, D. R. & Bruno, T. J. *CRC handbook of chemistry and physics: a ready-reference book of chemical and physical data.* (CRC Press, Taylor & Francis Group, Boca Raton, FL, 2017), 97th edn. URL doi.org/10.1201/9781315380476.

APPENDIX A
PUBLICATIONS

Astrath, N. G. C., **Flizikowski, G. A. S.**, Anghinoni, B., Malacarne, L. C., Baesso, M. L., Požar, T., Partanen, M., Brevik, I., Razansky, D. & Bialkowski, S. E. Unveiling bulk and surface radiation forces in a dielectric liquid. Light: Science and Applications 11, 10 (2022). [doi.org/10.1038/s41377-022-00788-7].

Anghinoni, B., **Flizikowski, G. A. S.**, Malacarne, L. C., Partanen, M., Bialkowski, S. E. & Astrath, N. G. C. On the formulations of the electromagnetic stress–energy tensor. Annals of Physics 443, 169004 (2022). [doi.org/10.1016/j.aop.2022.169004].

Astrath, N. G. C., Anghinoni, B., **Flizikowski, G. A. S.**, Zanuto, V. S., Malacarne, L. C., Baesso, M. L., Požar, T. & Razansky, D. The role of electrostriction in the generation of acoustic waves by optical forces in water. Photoacoustics 29, 100445 (2023). [doi.org/10.1016/j.pacs.2022.100445].

Flizikowski, G. A. S., Zanuto, V. S., Nunes, L. A. O., Baesso, M. L., Malacarne, L. C. & Astrath, N. G. C. Standard and modified Judd-Ofelt theories in Pr3+-doped calcium aluminosilicate glasses: A comparative analysis. Journal of Alloys and Compounds 780, 705–710 (2019). [doi.org/10.1016/j.jallcom.2018.11.308].

Capeloto, O. A., Zanuto, V. S., Camargo, V. G., **Flizikowski, G. A. S.**, Lukasievicz, G. V. B., Herculano, L. S., Belançon, M. P., Astrath, N. G. C. & Malacarne, L. C. Nanosecond pressure transient detection of laser-induced thermal lens. Applied Optics 59, 3682 (2020). [doi.org/10.1364/AO.389545].

Flizikowski, G. A. S., Anghinoni, B., Rohling, J. H., Belançon, M. P., Mendes, R. S., Baesso, M. L., Malacarne, L. C., Požar, T., Bialkowski, S. E. & Astrath, N. G. C. Influence of edge effects on laser-induced surface displacement of opaque materials by photothermal interferometry. Journal of Applied Physics 128, 044509 (2020). [doi.org/10.1063/5.0015996].

Flizikowski, G. A. S., Capeloto, O. A., Camargo, V. G., Anghinoni, B., Baesso, M. L., Malacarne, L. C., Belançon, M. P., Požar, T. & Astrath, N. G. C. Laser induced thermoelastic surface displacement in solids detected simultaneously by photothermal mirror and interferometry. Optics Express 28, 7116 (2020). [doi.org/10.1364/OE.386344].

Oliveira, G. M., Zanuto, V. S., **Flizikowski, G. A. S.**, Kimura, N. M., Sampaio, A. R., Novatski, A., Baesso, M. L., Malacarne, L. C. & Astrath, N. G. C. Soret effect in lyotropic liquid crystal in the isotropic phase revealed by time-resolved thermal lens. Journal of Molecular Liquids 312, 113381 (2020). [doi.org/10.1016/j.molliq.2020.113381].

Bergmann, E. V., Capeloto, O. A., Catanio, A. T. S., **Flizikowski, G. A. S.**, Kimura, N. M., Freitas, C. F., Herculano, L. S., Astrath, N. G. C. & Malacarne, L. C. Photoactivation of Erythrosine in Simulated Body Fluids. Spectrochimica Acta Part A: Molecular and Biomolecular Spectroscopy 119867 (2021). [doi.org/10.1016/j.saa.2021.119867].

Capeloto, O. A., Zanuto, V. S., Camargo, V. G., **Flizikowski, G. A. S.**, Morais, F. A. P., Lukasievicz, G. V. B., Herculano, L. S., Belançon, M. P., Astrath, N. G. C. & Malacarne, L. C. Induction and detection of pressure waves by pulsed thermal lens technique in water–ethanol mixtures. Applied Optics 60, 4029 (2021). [doi.org/10.1364/AO.420275].

Astrath et al. *Light: Science & Applications* (2022)11:103
https://doi.org/10.1038/s41377-022-00788-7

Official journal of the CIOMP 2047-7538
www.nature.com/lsa

ARTICLE Open Access

Unveiling bulk and surface radiation forces in a dielectric liquid

N. G. C. Astrath[1]✉, G. A. S. Flizikowski[1], B. Anghinoni[1], L. C. Malacarne[1], M. L. Baesso[1], T. Požar[2], M. Partanen[3], I. Brevik[4], D. Razansky[5,6] and S. E. Bialkowski[7]

Abstract

Precise control over light-matter interactions is critical for many optical manipulation and material characterization methodologies, further playing a paramount role in a host of nanotechnology applications. Nonetheless, the fundamental aspects of interactions between electromagnetic fields and matter have yet to be established unequivocally in terms of an electromagnetic momentum density. Here, we use tightly focused pulsed laser beams to detect bulk and boundary optical forces in a dielectric fluid. From the optical convoluted signal, we decouple thermal and nonlinear optical effects from the radiation forces using a theoretical interpretation based on the Microscopic Ampère force density. It is shown, for the first time, that the time-dependent pressure distribution within the fluid chiefly originates from the electrostriction effects. Our results shed light on the contribution of optical forces to the surface displacements observed at the dielectric air-water interfaces, thus shedding light on the long-standing controversy surrounding the basic definition of electromagnetic momentum density in matter.

Introduction

Electromagnetic fields store linear momentum, accounting for the radiation pressure resulting from light-matter interactions responsible for many important nanotechnology applications[1–5]. Predicted by Maxwell in 1873[6], the fundamental aspects of radiation pressure physics still remain uncertain in regard to the correct definition of an electromagnetic momentum density in a medium[7–11]. First proposed by Minkowski in 1908[12] and followed by Abraham in 1909[13], the ongoing discussion on the form taken by the momentum of light in matter, the classic Abraham–Minkowski controversy, has been extensively described in many notable theoretical and experimental contributions[14–32].

The problem associated with this controversy appears to be a simple choice of the most suitable expression for the electromagnetic momentum density in matter. The implications of such a choice are however far reaching, being driven by many of the most precise experimental tools available today. To illustrate the origin of this fascinating problem, the energy-momentum tensor proposed by Minkowski predicts a momentum proportional to the refractive index of the medium, n, and to the momentum in vacuum, p_0, as $p_M = np_0$, while Abraham predicts a momentum $p_A = p_0/n$. It turns out that both energy-momentum tensors lead to common electromagnetic forces at interfaces that can be equally used to describe most of the experimental results obtained to date.

Theoretically, the controversy has been resolved by identifying the kinetic momentum via canonical momentum proposed by Abraham and Minkowski's description[17]. The canonical momentum is the total momentum of light, while the kinetic momentum is the electromagnetic momentum when the rest of the total momentum is deposited locally in the material by a force density term called the Abraham force. This would settle the debate and present both momenta as legitimate yet describing different aspects of the electromagnetic wave phenomena[14,17,33]. Although this assumption may sound

Correspondence: N G. C. Astrath (ngcastrath@uem.br)
[1]Department of Physics, Universidade Estadual de Maringá, Maringá, PR, Brazil
[2]Faculty of Mechanical Engineering, University of Ljubljana, Ljubljana, Slovenia
Full list of author information is available at the end of the article

Photoacoustics 29 (2023) 100445

Contents lists available at ScienceDirect

Photoacoustics

journal homepage: www.elsevier.com/locate/pacs

The role of electrostriction in the generation of acoustic waves by optical forces in water

N.G.C. Astrath [a,*], B. Anghinoni [a], G.A.S. Flizikowski [a], V.S. Zanuto [a], L.C. Malacarne [a], M.L. Baesso [a], T. Požar [b], D. Razansky [c,d]

[a] Department of Physics, Universidade Estadual de Maringá, 87020-900 Maringá, Brazil
[b] Faculty of Mechanical Engineering, University of Ljubljana, 1000 Ljubljana, Slovenia
[c] Institute for Biomedical Engineering and Institute of Pharmacology and Toxicology, Faculty of Medicine, University of Zurich, 8057 Zurich, Switzerland
[d] Institute for Biomedical Engineering, Department of Information Technology and Electrical Engineering, ETH Zurich, 8093 Zurich, Switzerland

ARTICLE INFO

Keywords:
Electrostriction
Radiation forces
Photo-induced lensing effect
Pressure-transients
Kerr lens

ABSTRACT

We present semi-analytical solutions describing the spatiotemporal distributions of temperature and pressure inside low-absorbing dielectrics excited by tightly focused laser beams. These solutions are compared to measurements in water associated with variations of the local refractive index due to acoustic waves generated by electrostriction, heat deposition, and the Kerr effect at different temperatures. The experimental results exhibited an excellent agreement with the modeling predictions, with electrostriction being the dominant transient effect in the acoustic wave generation. Measurements at 4.0 °C show that the thermoelastic contribution to the optical signal is significantly reduced due to the low thermal expansion coefficient of water at this temperature.

1. Introduction

The definitive knowledge of the electromagnetic forces acting inside matter under the influence of external fields remains an open problem in Physics. It is directly related to the century-old Abraham–Minkowski dilemma [1,2], which deals with the electromagnetic momentum transfer in dielectric media. The topic has recently drawn significant attention in the context of applications relying on complete manipulation of optical forces [3], such as optical traps [4], photonic devices [5] and optofluidic technology [6,7].

When electromagnetic fields are applied to continuous matter, variety of effects can take place. Regarding internal forces, one known contribution is related to the tendency of the matter to be compressed towards the regions of higher field intensity due to the interaction between the induced dipoles and the applied electromagnetic fields. Such compression forces occur even for static fields and are commonly described as electrostriction in the case of polarizable media or magnetostriction for magnetizable media. In conductors, these striction effects can slightly deform the medium, leading to observable changes in its shape [8]. In turn, dielectric media respond by increasing their local pressure or strain until the forces are completely compensated — striction forces are thus inherently transient effects. The compensation time-scale involved is the interval it takes for the generated acoustic waves to propagate over one beam width, typically about 10–100 ns [9] when tightly focused beams of light are used as the excitation source.

Striction forces appear as important contributions in opto-acoustic techniques, such as laser-induced thermal acoustics [10] and laser induced phonons [11]. Additionally, they are often related to fluid stability [12,13] and can also provide the necessary non-linear coupling that leads to stimulated Brillouin scattering [14,15]. Electrostriction has also been suggested as an alternative way to improve piezoelectricity in ferroelectric materials [16].

Accurate measurements of striction forces have been historically challenging since even small or moderate thermal effects usually dominate [17]. One of the well-established methods in the literature to probe these effects consists in analyzing the diffraction generated by stimulated Brillouin scattering [18–22]. Alternatively, in liquids the local variation of pressure alters the local index of refraction of the material, an effect that can usually be probed in weakly absorbing transparent media by optical techniques such as interferometry and photo-induced lensing [23].

On the theoretical side, striction effects are currently not very well understood. The generally adopted description relies on a phenomenological approach derived for thermodynamic equilibrium [8,24,25]. For static fields, good agreement with experiments has been found [26,

* Corresponding author.
E-mail address: ngcastrath@uem.br (N.G.C. Astrath).

https://doi.org/10.1016/j.pacs.2022.100445
Received 27 October 2022; Received in revised form 15 December 2022; Accepted 26 December 2022
Available online 30 December 2022

Annals of Physics 443 (2022) 169004

Contents lists available at ScienceDirect

Annals of Physics

journal homepage: www.elsevier.com/locate/aop

On the formulations of the electromagnetic stress–energy tensor

B. Anghinoni [a], G.A.S. Flizikowski [a], L.C. Malacarne [a], M. Partanen [b,*], S.E. Bialkowski [c], N.G.C. Astrath [a]

[a] Physics Department, Universidade Estadual de Maringá, Maringá, PR 87020-900, Brazil
[b] Department of Electronics and Nanoengineering, Aalto University, 00076 Aalto, Finland
[c] Department of Chemistry and Biochemistry, Utah State University, UT 84322-0300, USA

ARTICLE INFO

Article history:
Received 28 January 2022
Accepted 29 June 2022
Available online 2 July 2022

Keywords:
Stress–energy tensor
Optical force
Optomechanics
Momentum of light
Radiation pressure
Electromagnetism

ABSTRACT

In this work, we review the main existing theories for the electromagnetic stress–energy tensor in dielectric media — a problem directly related to the century-long debate regarding the correct momentum of light in dielectric media, known as Abraham–Minkowski controversy. The theoretical validity of the main existing formulations is analyzed in terms of symmetry and invariance requirements for the tensors. We also present position- and time-dependent numerical simulations of the related electromagnetic forces for a lossless nondispersive medium, highlighting the different expected spatial force distributions. The force densities of different formulations drive forward different momentum and atomic number density distributions of the medium contributing to the total momentum and energy densities associated with the coupled field-medium state of light.

1. Introduction

Historically, there has been a continuing debate on a century-long problem regarding which is the correct form for the electromagnetic momentum transfer in dielectric media, originally known as Abraham–Minkowski controversy. It started in 1908 when Minkowski [1] used the wave

* Corresponding author.
E-mail addresses: brunoanghinoni@gmail.com (B. Anghinoni), mikko.p.partanen@aalto.fi (M. Partanen), ngcastrath@uem.br (N.G.C. Astrath).

https://doi.org/10.1016/j.aop.2022.169004

Research Article Vol. 60, No. 13 / 1 May 2021 / Applied Optics 4029

applied optics

Induction and detection of pressure waves by pulsed thermal lens technique in water–ethanol mixtures

Otávio A. Capeloto,[1,2] Vitor S. Zanuto,[1] Vinicius G. Camargo,[1] Gabriel A. S. Flizikowski,[1] Flávia A. P. Morais,[3] Gustavo V. B. Lukasievicz,[4] Leandro S. Herculano,[4] Marcos P. Belançon,[5] Nelson G. C. Astrath,[1,*] and Luis C. Malacarne[1,6]

[1]Departamento de Física, Universidade Estadual de Maringá, Maringá, PR 87020-900, Brazil
[2]Instituto de Saúde e Biotecnologia de Coari, Universidade Federal do Amazonas, Coari, AM 69460-000, Brazil
[3]Departamento de Química, Universidade Estadual de Maringá, Maringá, PR 87020-900, Brazil
[4]Departamento de Física, Universidade Tecnológica Federal do Paraná, Medianeira, PR 85884-000, Brazil
[5]Departamento de Física, Universidade Tecnológica Federal do Paraná, Pato Branco, PR 85503-390, Brazil
[6]e-mail: lcmala@dfi.uem.br
*Corresponding author: ngcastrath@uem.br

Received 19 January 2021; revised 17 March 2021; accepted 1 April 2021; posted 2 April 2021 (Doc. ID 420275); published 29 April 2021

The mode-mismatched dual-beam thermal lens technique is widely applied in the characterization of optical and thermo-physical properties of solids and liquids. The technique has also been used to investigate transient acoustic waves induced by pulsed laser excitation at the nanosecond time scale. In this paper, we developed a semi-analytical model to describe the transient acoustic wave that allows a fitting procedure to get the physical properties of fluid samples. The method was used to investigate samples with different mixtures of ethanol and water, and quantitative information of piezo-optic coefficient and sound speed are evaluated for the fluid mixtures.

https://doi.org/10.1364/AO.420275

1. INTRODUCTION

The effects of light interacting with matter provide a rich scenario for which a large number of phenomena can be induced and detected at different time scales. Different techniques such as optical transmittance, fluorescence, interferometry, and photothermal methods are usually employed to investigate light/matter interaction effects in solids, liquids, and gases. Concerning photothermal methods, photoacoustic, mirage, thermal radiometry, thermal grating, thermal mirror, and thermal lens (TL) are the most common techniques [1].

In particular, the mode-mismatched dual-beam TL has been widely applied in the characterization of solid and liquid samples due to its remote, sensitive, and non-destructive characteristics [1]. In addition, this method has the possibility to reach very low limits of detection and make measurements on micro samples. The TL effect was first observed by Gordon *et al*. [2] and followed by several experimental configurations and mathematical models describing the effects in a number of applications [3–9]. The mode-mismatched TL configuration proposed by Shen *et al*. [10] is one of the most used methods for both continuous and pulsed laser excitation regimes.

In continuous excitation, effects in the order of seconds, such as thermal diffusion, the Soret effect, and photochemical reaction, have been observed [9,11,12]. In addition, at the millisecond scale, the method has also been applied to study electronic effects and quantum yield of triplet state formation in glasses [13–15]. Under pulsed excitation, in general, a short pulse of light is considered to be absorbed, and the signal is obtained at the millisecond to second scale, after acoustic relaxation, when only TL effect contributes to the signal [16–19]. At the millisecond time scale, in addition to the TL, in some samples, the probe beam intensity is also affected by a transient absorption and/or excited state gradient [20]. This effect is referred to as the population lens and may give a significant contribution to the TL signal in some cases, for example, in solutions of C_{60} in benzene [21].

The potential of the TL technique to investigate laser-induced acoustic waves has been presented to study gas, fluid, and glass samples. For fluid, only qualitative analysis was performed [22]. For gas and glass [23,24], a very short pulse laser (femtosecond) was used, assuming an instantaneous Dirac delta heat source and a time-independent temperature profile, since the thermal diffusion was taking place only for longer times.

1559-128X/21/134029-05 Journal © 2021 Optical Society of America

Spectrochimica Acta Part A: Molecular and Biomolecular Spectroscopy 259 (2021) 119867

Contents lists available at ScienceDirect

Spectrochimica Acta Part A: Molecular and Biomolecular Spectroscopy

journal homepage: www.elsevier.com/locate/saa

Photoactivation of Erythrosine in simulated body fluids

Eduardo V. Bergmann [a], Otávio A. Capeloto [b], Angelo T.S. Catanio [a], Gabriel A.S. Flizikowski [a], Newller M. Kimura [a], Camila F. Freitas [c], Leandro S. Herculano [d], Nelson G.C. Astrath [a,*], Luis C. Malacarne [a]

[a] Departamento de Física, Universidade Estadual de Maringá, Maringá, PR 87020-900, Brazil
[b] Instituto de Saúde e Biotecnologia de Coari, Universidade Federal do Amazonas, Coari, AM 69460-000, Brazil
[c] Departamento de Química, Universidade Estadual de Maringá, Maringá, PR 87020-900, Brazil
[d] Departamento de Física, Universidade Tecnológica Federal do Paraná, Medianeira, PR 85884-000, Brazil

HIGHLIGHTS

- Photoactivation process of Erythrosine was investigated in different simulated body fluids.
- Optical techniques were used to investigate the photoactivation process.
- Thermal lens results reveled photobleaching in submicromolar concentrations range.
- Clear differences in the photodegradation kinetics, triplet lifetime and singlet oxygen generation were observed.
- The results presented could help to explain and to define Photodynamic Therapy application protocols.

GRAPHICAL ABSTRACT

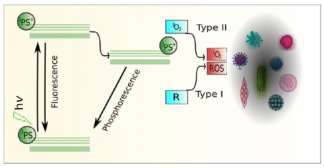

ARTICLE INFO

Article history:
Received 19 March 2021
Received in revised form 15 April 2021
Accepted 19 April 2021
Available online 27 April 2021

Keywords:
Erythrosine
Photobleaching
Triplet Lifetime
Thermal Lens

ABSTRACT

Photodynamic Therapy (PDT) is a powerful technique for the treatment of cancer and non-cancerous diseases. The precise PDT treatment protocol definition must consider the performance difference between *in vitro* and *in vivo* applications. This also occurs in other biological studies, and to partially overcome this difficulty, the simulated body fluids are generally applied as a prior understanding of the particularities of the different systems. However, in PDT these studies are scarce. In this work, we investigated the photoactivation of Erythrosine, a photosensitizer widely used in PDT, in different simulated body fluids. Differences in the photodegradation kinetics, triplet lifetime, and singlet oxygen generation were observed. The results can help to explain and to define PDT application protocols.

1. Introduction

Photodynamic therapy (PDT) is a technique applied to combat various diseases, which is based on the photoactivation of a photosensitizing compound (PS) by radiation of wavelength consistent with its absorption spectrum, in the presence of molecular oxygen ($^3O_2$). The interaction of these species leads to the generation of cytotoxic species, such as singlet oxygen ($^1O_2$) and other reactive oxygen species (ROS), which are responsible for cell death [1–4]. Currently, PDT represents a well-established clinical modality for the treatment of a variety of malignant tumors [5,6]. However, it has also been used in the treatment of various non-cancerous conditions such as benign prostatic hyperplasia, age-related macular

* Corresponding author.
E-mail addresses: ngcastrath@uem.br (N.G.C. Astrath), lcmala@dfi.uem.br (L.C. Malacarne).

https://doi.org/10.1016/j.saa.2021.119867
1386-1425/

Journal of Applied Physics ARTICLE scitation.org/journal/jap

Influence of edge effects on laser-induced surface displacement of opaque materials by photothermal interferometry

Cite as: J. Appl. Phys. **128**, 044509 (2020); doi: 10.1063/5.0015996
Submitted: 1 June 2020 · Accepted: 8 July 2020 ·
Published Online: 29 July 2020

G. A. S. Flizikowski,[1] B. Anghinoni,[1] J. H. Rohling,[1] M. P. Belançon,[2] R. S. Mendes,[1] M. L. Baesso,[1] L. C. Malacarne,[1] T. Požar,[3] S. E. Bialkowski,[4] and N. G. C. Astrath[1,a)]

AFFILIATIONS

[1]Departamento de Física, Universidade Estadual de Maringá, Maringá, PR 87020-900, Brazil
[2]Departamento de Física, Universidade Tecnológica Federal do Paraná, Pato Branco, PR 85503-390, Brazil
[3]Faculty of Mechanical Engineering, University of Ljubljana, Ljubljana 1000, Slovenia
[4]Department of Chemistry and Biochemistry, Utah State University, Logan, Utah 84322-0300, USA

Note: This paper is part of the Special Topic on Photothermics.
[a)]**Author to whom correspondence should be addressed:** ngcastrath@uem.br

ABSTRACT

We demonstrate the influence of edge effects on the photothermal-induced phase shift measured by a homodyne quadrature laser interferometer and compare the experiments with rigorous theoretical descriptions of thermoelastic surface displacement of metals. The finite geometry of the samples is crucial in determining how the temperature is distributed across the material and how this affects the interferometer phase shift measurements. The optical path change due to the surface thermoelastic deformation and thermal lens in the surrounding air is decoded from the interferometric signal using analytical and numerical tools. The boundary/edge effects are found to be relevant to properly describe the interferometric signals. The tools developed in this study provide a framework for the study of finite size effects in heat transport in opaque materials and are applicable to describe not only the phase shift sensed by the interferometer but also to contribute to the photothermal-based technologies employing similar detection mechanisms.

I. INTRODUCTION

The dynamic events following light absorption at the surface of the inspected material contain information on the structure of matter, its geometry, and its physical and thermoelastic properties. The temperature changes resulting from optical absorption are responsible for generating thermoelastic disturbances detectable at the surfaces of the sample, bringing characteristic signatures of defects and shape of the system that can be exploited experimentally in several different ways. External and internal boundaries are accessible in such a system, for example, by monitoring the perturbations caused by heat diffusion at the interfaces[1] or by elastic waves reverberating within the material.[2]

In practice, the inspected materials have to be prepared as samples of well-defined finite dimensions, often as small as possible, especially when the material is expensive or difficult to be produced. This, in turn, imposes some limitations on how to model the response of such samples and compare the model to the measurements to retrieve the unknown sample properties. The lateral heat flow confinement or the elastic waves reflections from the samples surfaces are known as edge effects. They become important when the heat diffusion flow is laterally halted or when the disturbances reflect from the edges and return to the detection site. The edge effects are responsible for the scattering of elastic waves propagating inside materials and form the basis of photothermal ultrasound detection systems with applications ranging from biological imaging[3,4] to defect inspection.[5,6] Edge effects also have an important role in material processing procedures.[7–9] Several methods including laser interferometry have been used for investigating surface properties,[10,11] local magnetic property deteriorations in metals,[12] microdamage evolution,[13] fatigue failure,[14] mechanical properties,[15,16] and

Research Article Vol. 28, No. 5 / 2 March 2020 / Optics Express 7116
Optics EXPRESS

Laser induced thermoelastic surface displacement in solids detected simultaneously by photothermal mirror and interferometry

G. A. S. Flizikowski,[1] O. A. Capeloto,[1] V. G. Camargo,[1] B. Anghinoni,[1] M. L. Baesso,[1] L. C. Malacarne,[1] M. P. Belançon,[2] T. Požar,[3] and N. G. C. Astrath[1,*]

[1]*Departamento de Física, Universidade Estadual de Maringá, Maringá, PR 87020-900, Brazil*
[2]*Universidade Tecnológica Federal do Paraná, Pato Branco, PR 85503-390, Brazil*
[3]*Faculty of Mechanical Engineering, University of Ljubljana, Ljubljana 1000, Slovenia*
[*]*ngcastrath@uem.br*

Abstract: We propose a combined pump-probe optical method to investigate heat diffusion properties of solids. We demonstrate single-shot simultaneous laser-induced thermoelastic surface displacement of metals detected by concurrent measurements using photothermal mirror and interferometry. Both methods probe the surface displacement by analyzing the wavefront distortions of the probe beams reflected from the surface of the sample. Thermoelastic properties are retrieved by transient analysis in combination with numerical description of the thermoelastic displacement and temperature rise in the sample and in the surrounding air. This technique presents a capability for material characterization that can be extended to experiments for quantitative surface mapping.

1. Introduction

All-optical pump-probe methods are advanced techniques for general non-destructive material characterization, characterized by detecting the effects generated by the interaction between light and matter. These effects depend on the ability of the material to convert light into radiative and non-radiative processes [1].

The non-contacting nature of pump-probe methods allows accessing thermal, optical and mechanical properties of solids. These methods require reflective surfaces in order to directly detect the perturbation caused by light absorption and have to be capable of detecting probe beam wavefront deformation. Two such methods are the photothermal mirror and the interferometry [2–7]. Both are naturally similar in this sense, because they detect wavefront distortion, although employing different optical detection mechanisms.

The photothermal mirror (TM) spectrometry detects the deformation of the illuminated surface by analyzing the focusing or defocusing of the reflected probe beam in the far field region [8–12]. TM measures a convoluted signal arising from the wavefront distortion caused by the probed surface of the sample in addition to the phase shift created by heat-coupling in the fluid surrounding the sample. This method has been recently introduced under pulsed Gaussian laser excitation for the measurement of thermal diffusivity and thermo-optical properties of semi-transparent and opaque solids [8,9] and for the detection of thermoelastic waves launched by a localized heat deposition [13–15]. This method has also been used to detect surface displacements induced by radiation pressure at air-liquids interfaces [11,12].

Out-of-plane surface displacement can be detected with a homodyne quadrature laser interferometer (HQLI) [16–18], a special extension of the arm-compensated Michelson interferometer [18,19]. HQLI employs the quadrature detection using a stable, linearly polarized laser. Using an additional octadic-wave plate and a polarizing beam splitter, two orthogonally polarized

#386344 https://doi.org/10.1364/OE.386344
Journal © 2020 Received 19 Dec 2019; revised 10 Feb 2020; accepted 10 Feb 2020; published 25 Feb 2020

applied optics

Nanosecond pressure transient detection of laser-induced thermal lens

Otávio A. Capeloto,[1] Vitor S. Zanuto,[1] Vinicius G. Camargo,[1] Gabriel A. S. Flizikowski,[1] Gustavo V. B. Lukasievicz,[2] Leandro S. Herculano,[2] Marcos P. Belançon,[3] Nelson G. C. Astrath,[1,*] and Luis C. Malacarne[1]

[1]Departamento de Física, Universidade Estadual de Maringá, Maringá, PR 87020-900, Brazil
[2]Universidade Tecnológica Federal do Paraná, Medianeira, PR 85884-000, Brazil
[3]Universidade Tecnológica Federal do Paraná, Pato Branco, PR 85503-390, Brazil
*Corresponding author: ngcastrath@uem.br

Received 31 January 2020; revised 13 March 2020; accepted 19 March 2020; posted 19 March 2020 (Doc. ID 389545); published 16 April 2020

We use the thermal lens technique in the nanosecond time scale to describe the acoustic wave effect in liquids and the corresponding correlation with the speed of sound in the fluid, volumetric thermal expansion, and piezo-optic coefficient. These physical properties are found to be directly correlated to the anomalous effects observed in the transients at the nanosecond time scale, where acoustic waves dominate the thermal lens signal inducing an oscillating transient. Our results suggest the application of the thermal lens to study the generation and the detection of thermo-acoustic waves in liquids, which makes this method interesting for all-optoacoustic ultrasound detection and imaging.

https://doi.org/10.1364/AO.389545

1. INTRODUCTION

Time-resolved thermal lens spectroscopy is a powerful non-contact all-optical pump–probe photothermal method widely used in the characterization of a large set of physical properties of solids and liquids [1–9]. In this technique, a continuous or pulsed laser beam induces a thermal perturbation in the sample, which is probed by a continuous laser beam crossing the same region of the sample. The transient signal is monitored at the far-field detector by analyzing the wavefront distortion of the probe beam.

The intensity of the center of the probe beam at the far-field detector changes according to the laser-induced phase shift $\Phi(r, t)$ in the sample as [10]

$$I(t) = \left| \int_0^\infty \frac{2r}{w_p^2} \exp\left[-(1 + iV)\frac{r^2}{w_p^2} - i\Phi(r, t) \right] dr \right|^2, \tag{1}$$

where V is an experimental parameter from the experimental setup and w_p is the probe beam radius in the sample.

The thermal lens technique detects a broad range of phenomena arising from the interaction between light and matter at different time scales. Under continuous laser excitation, for instance, transients at the scale of seconds are observed from effects such as heat diffusion, Soret effect, and photoinduced chemical reaction [9,11,12]. Transients at millisecond time scale have been reported from studies on the electronic effects and quantum yield of triplet state formation in glasses [13–15]. Under pulsed laser excitation, a number of additional effects may take place at very short time [16–19]. At the millisecond time scale, in addition to the thermal lens, the probe beam intensity may also be affected by transient absorption and/or excited state gradient [20]. This effect is referred to as population lens and may give significant contribution to the thermal lens signal in some cases [21]. At shorter time scales, acoustic waves may give rise to pressure effects [22], which are the foundation for ultrasound detection and imaging [22–25].

Here we report a study using the thermal lens technique to investigate transient acoustic waves launched by a localized heat deposition at the nanosecond time scale. Pulsed laser excitation is used to generate pressure perturbation in liquids that are detected using the thermal lens method. At this time scale, acoustic waves dominate the thermal lens signal inducing an oscillating transient. The observed signal is described theoretically by calculating the built-in pressure contribution to the phase shift induced in the sample. The volumetric thermal expansion, piezo-optic coefficient, and sound speed of liquids are found to be directly correlated to the anomalous effects observed in the transients.

1559-128X/20/123682-04 Journal © 2020 Optical Society of America

Journal of Molecular Liquids 312 (2020) 113381

Contents lists available at ScienceDirect

Journal of Molecular Liquids

journal homepage: www.elsevier.com/locate/molliq

Soret effect in lyotropic liquid crystal in the isotropic phase revealed by time-resolved thermal lens

G.M. Oliveira [a], V.S. Zanuto [a], G.A.S. Flizikowski [a], N.M. Kimura [a], A.R. Sampaio [a], A. Novatski [b], M.L. Baesso [a], L.C. Malacarne [a], N.G.C. Astrath [a,*]

[a] Department of Physics, Universidade Estadual de Maringá, Maringá, PR 87020-900, Brazil
[b] Department of Physics, Universidade Estadual de Ponta Grossa, Ponta Grossa, PR 84010-330, Brazil

ARTICLE INFO

Article history:
Received 6 April 2020
Received in revised form 13 May 2020
Accepted 15 May 2020
Available online 18 May 2020

Keywords:
Soret effect
Thermodiffusion
Thermal Lens
Lyotropic liquid crystal
Mass diffusion

ABSTRACT

We demonstrate the Soret effect in a lyotropic liquid crystal at different temperatures across the isotropic phase detected by the time-resolved thermal lens technique. We investigate thermo-optical and mass diffusion properties of the sample and present quantitative characterization of Soret, mass and thermal diffusion coefficients. The results reveal that the temperature gradient induced in the experiments causes the migration of micelles from hotter to colder regions in the sample. The increase of the mass diffusion coefficient with temperature is related to the decrease of the radius of the micelles in the solution.

1. Introduction

Lyotropic liquid crystals are formed by dissolving amphiphilic molecules in a solvent (usually water). The self-assembly of amphiphilic molecules in excess water are influenced by the structural characteristics of the amphiphilic molecule and the conditions of the solution. As the surfactant concentration in the solution (c) exceeds the critical micellar concentration (CMC), different polymorphic structures can be observed. At low concentrations of amphiphilic ($c \approx$ CMC) spherical micelles are formed with typical diameter of about twice the length of the surfactant carbon chain, which results in a clear and isotropic solution. At amphiphilic concentrations greater than 100 CMC, although randomly oriented in space in an isotropic phase, micelles with non-spherical shape can be observed [1]. Micellar isotropic phase is optically isotropic, with a single index of refraction. The characteristic X-ray diffraction pattern of this phase presents a small-angle scattering due to the individual micelles, with a modulus of the scattering vector $s \approx 2 \times 10^{-2}$ nm^{-1} [2].

The order of stability of different lyotropic phases varies as a function of concentration (and of temperature) of amphiphilic molecules in water. At high concentrations, micelles aggregate forming ordered structures leading to hexagonal, cubic or lamellar phases, for instance [3]. Furthermore, at high concentrations, nematic and cholesteric phases are also obtained [4–7]. The lyotropic isotropic phase is useful for numerous potential applications, especially for encapsulation of a wide range of target molecules or controlled release drugs [8–13]. The particular properties of each structural phase lead to different diffusion coefficients in the solution, which depend on temperature and on the micellar concentration.

Mass diffusion may be induced within a fluid mixture by a temperature gradient. The spatial temperature distribution is the driving force that causes migration of components in the mixture from regions with different temperatures. This effect is known as thermodiffusion or the Soret effect. The Soret coefficient (S_T) determines the magnitude of thermodiffusion in the steady state. Thermodiffusion is observed in a variety of molecular systems, including gases, simple and multicomponent liquid mixtures [14]. The Soret effect is relevant in many fields including applications in the manipulation of macromolecules in biology [14–16], separation processes in polymer solutions [17,18], and colloidal dispersions [19–21]. The drift of dispersed particles due to a thermal gradient allows contact-free molecular segregation [22,23] and has been used to manipulate molecules for DNA trapping [24–26]. Detection of thermal diffusion in liquid mixtures is feasible with many different experimental approaches [27,28]. Thermodiffusion can be detected by pump-probe methods, such as the thermal lens method [20,29,30], grating methods [31–33], thermal diffusion cells [34–36], thermogravitational columns [37], field-flow fractionation [38], and microscopic methods [39,40].

* Corresponding author.
E-mail address: ngcastrath@uem.br (N.G.C. Astrath).

https://doi.org/10.1016/j.molliq.2020.113381
0167-7322/

Journal of Alloys and Compounds 780 (2019) 705–710

Contents lists available at ScienceDirect

Journal of Alloys and Compounds

journal homepage: http://www.elsevier.com/locate/jalcom

Standard and modified Judd-Ofelt theories in Pr^{3+}-doped calcium aluminosilicate glasses: A comparative analysis

G.A.S. Flizikowski [a], V.S. Zanuto [a, b, *], L.A.O. Nunes [b], M.L. Baesso [a], L.C. Malacarne [a], N.G.C. Astrath [a]

[a] Departamento de Física, Universidade Estadual de Maringá, Maringá, PR, 87020-900, Brazil
[b] Instituto de Física de São Carlos, Universidade de São Paulo, São Carlos, SP, 13560-590, Brazil

ARTICLE INFO

Article history:
Received 28 August 2018
Received in revised form
5 November 2018
Accepted 22 November 2018
Available online 1 December 2018

Keywords:
Aluminosilicate glass
CAS:Pr^{3+}
LSCAS:Pr^{3+}
Standard Judd-Ofelt theory
Modified Judd-Ofelt theory

ABSTRACT

The small energy difference between the fundamental level and the first opposite parity configuration of Pr^{3+}-doped hosts is particularly challenging for the characterization of radiative transitions using the Judd-Ofelt theory, although modified versions of the theory have been proposed in the past for the investigation of praseodymium doped materials. Here, we present a detailed spectroscopic investigation on two sets of calcium aluminosilicate glasses, with 34 wt% of SiO_2 (CAS) and with 7 wt% of SiO_2 (LSCAS), doped with different concentrations of Pr^{3+} (0.5, 1.0 and 2.0 wt%). We use the standard Judd-Ofelt theory to characterize the glasses and the results and derived spectroscopic quantities — such as transition probabilities, radiative lifetimes and branching ratios — are compared to results obtained by the modified Judd-Ofelt theories. The analysis showed that the modified theories could lead to smaller values of root mean square deviations. However, a better agreement between experimental data and the standard theory was achieved when the derived spectroscopic quantities are taken into account. Moreover, the branching ratios of the $^3P_0 \rightarrow {}^3H_4$ and $^1D_2 \rightarrow {}^3H_4$ transitions were over 60% for both glass hosts, suggesting its potential use as solid-state laser devices.

1. Introduction

The great potentiality of rare earth elements as optically active ions in a wide variety of host materials is, in part, accounted by the minimal influence that the host crystal field has on the intra-configurational 4f electron distribution as it is shielded by the outer electronic shells. In this context, the third ionized state of praseodymium (Pr^{3+}) makes this ion an interesting element among other rare earths as a consequence of its variety of optical transitions. Ultraviolet (UV) emission can be provided by either direct excitation of 4f5d level or via upconversion mechanisms. In the visible (Vis) range, Pr^{3+} presents several optical transitions in blue, green [1], orange-red and in the red part of the spectrum [2]. Besides, a broad band emission in the infrared region, around 1.5 μm, suggests its applicability in devices for telecommunications [3].

Pr^{3+} has been studied in many different hosts, such as fluoride [4–6], borate [7–9], borosilicate [3,10], phosphate [11,12], fluorotellurite [13,14], and aluminosilicate glasses [15]. However, studies on Pr^{3+}-doped calcium aluminosilicate glasses (CAS) were only reported when co-doped with ytterbium (Yb^{3+}) [16], in which the authors investigated the occurrence of energy transfer processes from Pr^{3+} to Yb^{3+}. Recently, an investigation on the upconversion and hypersensitive transitions of Pr^{3+}-doped CAS glasses was reported [17]. Such glasses have attracted interest due to their appropriate thermo-optical and mechanical properties compared to silicates and phosphates [18], elevated transition temperature, and transparency up to 5 μm [19,20]. Investigations have also been performed with regard to the compositional dependence of the physical properties of the calcium aluminosilicate glasses [18,21]. When doped with rare earth elements, studies have shown that these glasses are potential candidates for optical devices such as tunable white light systems [21,22] and solid state lasers [21,23,24].

The luminescent properties of trivalent rare earth elements have been described with reasonable success by the Judd-Ofelt (J-O) theory [25,26]. However, the description of the spectroscopic properties of Pr^{3+} is particularly challenging due to the low energy difference between the fundamental level and the first opposite

* Corresponding author. Departamento de Física, Universidade Estadual de Maringá, Maringá, PR, 87020-900, Brazil.
E-mail address: vszanuto@gmail.com (V.S. Zanuto).

https://doi.org/10.1016/j.jallcom.2018.11.308
0925-8388/

APPENDIX B

PUBLISHER'S LICENSES

B.1 Optica Publishing Group

The statements presented in Fig. B.1 have been extracted from the "Open Access"[1] and "Copyright and Licensing" tabs, respectively, of the "Author Resources" page of the Optica website.

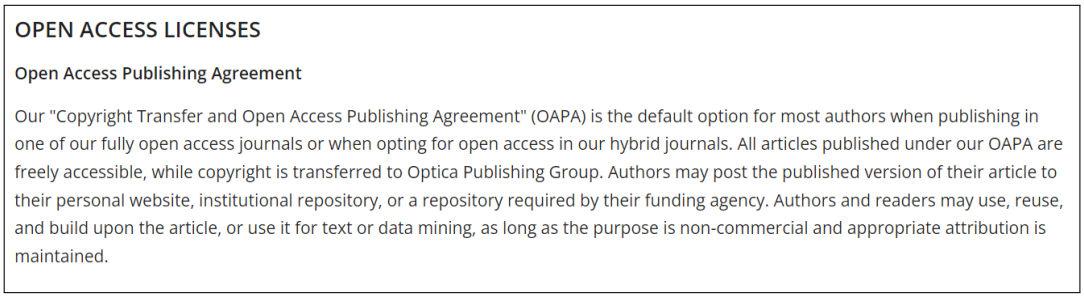

OPEN ACCESS LICENSES

Open Access Publishing Agreement

Our "Copyright Transfer and Open Access Publishing Agreement" (OAPA) is the default option for most authors when publishing in one of our fully open access journals or when opting for open access in our hybrid journals. All articles published under our OAPA are freely accessible, while copyright is transferred to Optica Publishing Group. Authors may post the published version of their article to their personal website, institutional repository, or a repository required by their funding agency. Authors and readers may use, reuse, and build upon the article, or use it for text or data mining, as long as the purpose is non-commercial and appropriate attribution is maintained.

(a)

Gold Open Access Publishing

Biomedical Optics Express, *Optica*, *Optical Materials Express*, *Optics Express*, and *OSA Continuum* are all gold open access journals. As a result of the authors paying an article processing charge (APC), all content published in these journals is freely available. Beginning with content published in September 2017, we allow users of our gold open access journals to read, download, copy, distribute, print, search, or link to the full texts of the articles, or use them for any other lawful purpose, without asking prior permission from us or the author. This is in accordance with the BOAI definition of open access. Authors may also opt to make their articles freely available in our hybrid journals, *Applied Optics*, *Journal of the Optical Society A*, *Journal of the Optical Society B*, *Optics Letters*, and *Journal of Optical Communications and Networking*.

(b)

Figure B.1: Optica Publishing statements based on the Open Access policy.

[1] See https://opg.optica.org/submit/review/open-access-policy-statement.cfm.

Figure B.2 below is the OPTICA's response to the requested permission to reprint the published paper as part of this thesis.

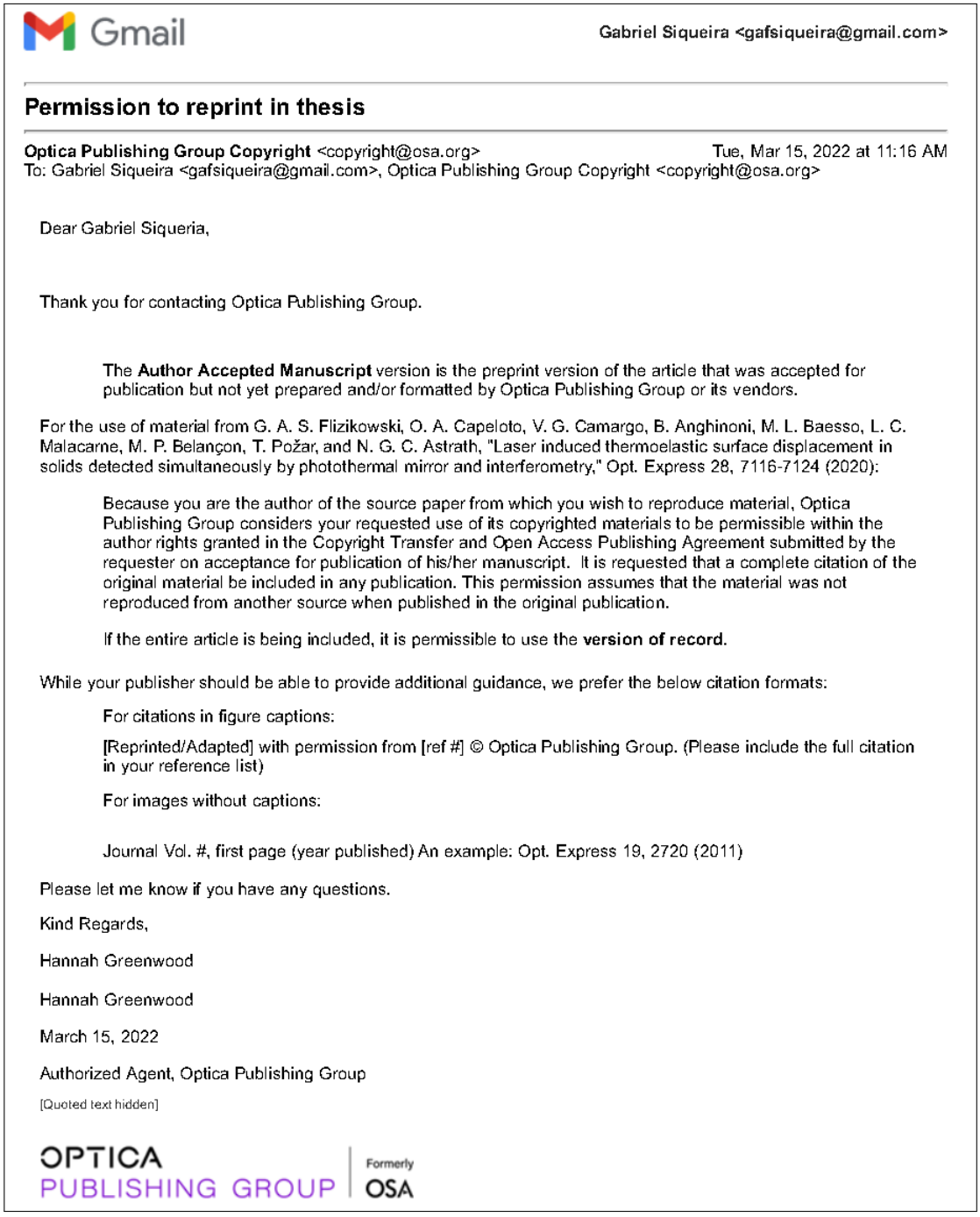

Gmail — Gabriel Siqueira <gafsiqueira@gmail.com>

Permission to reprint in thesis

Optica Publishing Group Copyright <copyright@osa.org> Tue, Mar 15, 2022 at 11:16 AM
To: Gabriel Siqueira <gafsiqueira@gmail.com>, Optica Publishing Group Copyright <copyright@osa.org>

Dear Gabriel Siqueria,

Thank you for contacting Optica Publishing Group.

The **Author Accepted Manuscript** version is the preprint version of the article that was accepted for publication but not yet prepared and/or formatted by Optica Publishing Group or its vendors.

For the use of material from G. A. S. Flizikowski, O. A. Capeloto, V. G. Camargo, B. Anghinoni, M. L. Baesso, L. C. Malacarne, M. P. Belançon, T. Požar, and N. G. C. Astrath, "Laser induced thermoelastic surface displacement in solids detected simultaneously by photothermal mirror and interferometry," Opt. Express 28, 7116-7124 (2020):

Because you are the author of the source paper from which you wish to reproduce material, Optica Publishing Group considers your requested use of its copyrighted materials to be permissible within the author rights granted in the Copyright Transfer and Open Access Publishing Agreement submitted by the requester on acceptance for publication of his/her manuscript. It is requested that a complete citation of the original material be included in any publication. This permission assumes that the material was not reproduced from another source when published in the original publication.

If the entire article is being included, it is permissible to use the **version of record.**

While your publisher should be able to provide additional guidance, we prefer the below citation formats:

For citations in figure captions:

[Reprinted/Adapted] with permission from [ref #] © Optica Publishing Group. (Please include the full citation in your reference list)

For images without captions:

Journal Vol. #, first page (year published) An example: Opt. Express 19, 2720 (2011)

Please let me know if you have any questions.

Kind Regards,

Hannah Greenwood

Hannah Greenwood

March 15, 2022

Authorized Agent, Optica Publishing Group

[Quoted text hidden]

OPTICA PUBLISHING GROUP | Formerly OSA

Figure B.2: OPTICA's response to the requested permission to reprint the published paper as part of this thesis.

B.2 AIP Publishing — American Institute of Physics

The statement presented in Fig. B.3 has been extracted from the AIP website in the "Author Licenses" section[2]. Item 5 refers to the specific use of published papers in the author's own thesis.

Author Rights and Permitted Uses

Subject to the rights herein granted to AIP Publishing, each Copyright Owner retains ownership of copyright and all other proprietary rights such as patent rights in the Work.

Each Copyright Owner retains the following nonexclusive rights to use the Work, without obtaining permission from AIP Publishing, in keeping with professional publication ethics, and provided clear credit is given to its first publication in an AIP Publishing journal. Any reuse must include a full credit line acknowledging AIP Publishing's publication and a link to the VOR on AIP Publishing's site.

Each Copyright Owner may:

1. Reprint portions of the Work (excerpts, figures, tables) in future works created by the Author, in keeping with professional publication ethics.
2. Post the Accepted Manuscript (AM) to their personal web page or their employer's web page immediately after acceptance by AIP Publishing.
3. Deposit the AM in an institutional or funder-designated repository immediately after acceptance by AIP Publishing.
4. Use the AM for posting within scientific collaboration networks (SCNs). For a detailed description of our policy on posting to SCNs, please see our Web Posting Guidelines (https://publishing.aip.org/authors/web-posting-guidelines).
5. Reprint the Version of Record (VOR) in print collections written by the Author, or in the Author's thesis or dissertation. It is understood and agreed that the thesis or dissertation may be made available electronically on the university's site or in its repository and that copies may be offered for sale on demand.
6. Reproduce copies of the VOR for courses taught by the Author or offered at the institution where the Author is employed, provided no fee is charged for access to the Work.
7. Use the VOR for internal training and noncommercial business purposes by the Author's employer.
8. Use the VOR in oral presentations made by the Author, such as at conferences, meetings, seminars, etc., provided those receiving copies are informed that they may not further copy or distribute the Work.
9. Distribute the VOR to colleagues for noncommercial scholarly use, provided those receiving copies are informed that they may not further copy or distribute the Work.
10. Post the VOR to their personal web page or their employer's web page 12 months after publication by AIP Publishing.
11. Deposit the VOR in an institutional or funder-designated repository 12 months after publication by AIP Publishing.
12. Update a prior posting with the VOR on a noncommercial server such as arXiv, 12 months after publication by AIP Publishing.

Figure B.3: List of permitted uses for authors extracted from the "Author Licenses" section of the AIP publishing website.

[2] Available at https://publishing.aip.org/resources/researchers/rights-and-permissions/author-licenses/.